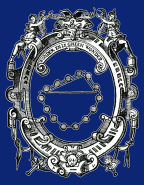

MECHANIK

FORSCHUNGSBERICHT

Multistable Structures for Broad Bandwidth Vibration-based Energy Harvesters: An Analytical Design Investigation

Matthias Heymanns

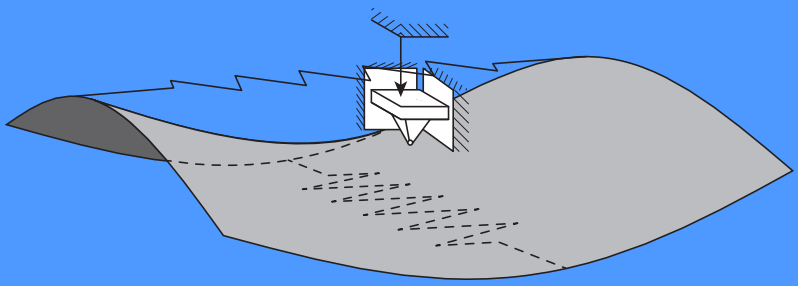

TECHNISCHE UNIVERSITÄT DARMSTADT

Band 39

Multistable Structures for Broad Bandwidth Vibration-based Energy Harvesters: An Analytical Design Investigation

Vom Fachbereich Maschinenbau
an der Technischen Universität Darmstadt
zur Erlangung des akademischen Grades
eines Doktor-Ingenieurs (Dr.-Ing.) genehmigte

Dissertation

vorgelegt von

Matthias Heymanns, MSc ETH

aus Darmstadt

Berichterstatter:	Prof. Dr. Peter Hagedorn
Mitberichterstatter:	Prof. Dr.-Ing. Bernhard Schweizer
Tag der Einreichung:	20. Oktober 2015
Tag der mündlichen Prüfung:	16. Dezember 2015

Darmstadt 2015

D 17

Heymanns, Matthias

Multistable Structures for Broad Bandwidth Vibration-based Energy Harvesters: An Analytical Design Investigation

Forschungsberichte des Instituts für Mechanik der Technischen Universität Darmstadt

Band 39

Herausgeber der Reihe:

Studienbereich Mechanik, Technische Universität Darmstadt

Verfasser:

Matthias Heymanns

Verlag:

Studienbereich Mechanik, Technische Universität Darmstadt

Franziska-Braun-Straße 7, 64287 Darmstadt

Bibliografische Information der Deutschen Nationalbibliothek:
Die Deutsche Nationalbibliothek verzeichnet diese Publikation in der Deutschen Nationalbibliografie; detaillierte bibliografische Daten sind im Internet über http://dnb.d-nb.de abrufbar.

ISBN 978-3-935868-39-6

Vorwort

Im Sommer 2012 wurde bei einem eher zufälligen gemeinsamen Eisessen mit meinem damaligen Kollegen Andres Arrieta an der ETH Zürich der Ausgangspunkt für die vorliegende Arbeit gelegt. Zu diesem Zeitpunkt war ich wissenschaftlicher Mitarbeiter am Zentrum für Strukturtechnologien. Andres Arrieta kam gerade von der TU Darmstadt, um am selben Institut als Post-Doc zu arbeiten. In der Arbeitsgruppe von Prof. Hagedorn hatte er zuvor an einem Projekt über breitbandiges Energy Harvesting gearbeitet. Aufgrund seines Wechsels an die ETH Zürich war nun die Position in Darmstadt frei. Aufgrund meiner ersten Erfahrungen in diesem Gebiet, ihm Rahmen meiner Bachelorarbeit an der TU Darmstadt, war mein Interesse sofort geweckt. Somit trat ich im Februar 2013 eine Stelle als wissenschaftlicher Mitarbeiter in der *Arbeitsgruppe Dynamik und Schwingungen* von Prof. Hagedorn an.

An dieser Stelle bedanke ich mich ganz herzlich bei allen, die zum Gelingen dieser Arbeit beigetragen haben. Insbesondere gilt mein Dank meinem Doktorvater Herrn Prof. Peter Hagedorn, dessen erste Vorlesungen mir noch immer im Gedächtnis sind. Sicherlich ist hier auch mein frühes Interesse an der Mechanik begründet. Für seine wissenschaftliche Betreuung und Förderung, gepaart mit genügend Freiraum eigene Ideen zu verfolgen und umzusetzen, bin ich sehr dankbar. Mein Dank gilt auch Herrn Prof. Bernhard Schweizer für die bereitwillige Übernahme des Koreferats und dem Interesse für meine Arbeit.

Ich möchte mich bei meinen derzeitigen und ehemaligen Kollegen Andreas Wagner, Manuel Eckstein, Eduard Heffel, Henning Spiegelberg, Dominic Jekel und Eoin Clerkin für die sehr gute Zusammenarbeit und die überaus angenehme Zeit in der Arbeitsgruppe bedanken. Auch gilt mein Dank Maria Rauck für ihre große Hilfsbereitschaft.

Herrn Jochen Ott danke ich für die tatkräftige und schnelle Hilfe bei der

Erstellung der experimentellen Aufbauten.

Zum Gelingen dieser Arbeit haben auch Johannes Kromer, Fridtjof Krische, Patricia Pauli und Marcel Knapp beigetragen, die ich im Rahmen einer Abschlussarbeit bzw. einer Tätigkeit als Hilfswissenschaftler betreut habe. Besonderes danke ich meinen Eltern für all die Förderung und Unterstützung über meinen gesamten Werdegang hinweg. Meiner geliebten Frau Simone, die mir den nötigen Rückhalt und Hilfe während der gesamten Zeit gegeben hat, möchte ich von Herzen danken. Im Rahmen dieser Arbeit habe ich nicht nur an fachlicher Kompetenz hinzugewonnen, sondern ich durfte auch unsere Familie wachsen sehen: Benaja und Linnéa. Für ihre Freude und Bereicherung bin ich ausgesprochen dankbar!

Darmstadt, Dezember 2015 Matthias Heymanns

Für mich aber ist Gottes Nähe beglückend! Mein Vertrauen setze ich auf den Herrn, ja, auf den Herrn.

Die Bibel, Psalm 73

Abstract

The field of vibrational energy harvesting aims to transform ambient mechanical energy into electrical energy. For example, this energy can be used to operate autonomous sensor units for structural health monitoring or to supply low power electronic devices. Robust energy harvesters that allow to harvest sufficient energy over a broad frequency range are crucial for these applications. One strategy to increase the bandwidth of energy harvesters and, thus, the robustness is the exploitation of multistable structures. This is due to their feature of showing large amplitude oscillations that result from snap-through actions (inter-well oscillations) in a significant frequency range.

The aim of this thesis is to analyze different multistable energy harvester designs in order to optimize their performance and formulate design criteria. The considered designs are a bistable electromechanical beam, a bistable electromechanical composite plate and a newly proposed design of a multistable plate with four equilibria. Firstly, analytical models for the multistable energy harvesters are presented in order to assess their broad bandwidth harvesting capabilities. Analytical methods are applied to these models to investigate the underlying bifurcation behavior. Based on the analytical investigations, design criteria are formulated to describe the favorable harvesting domain. Numerical simulations are performed to supplement the analytical investigations. The differences of the considered structures are highlighted concerning robust and efficient harvesting by means of numerical simulations for different types of excitation. Experiments are carried out to complement the analytical and numerical analysis. The experiments establish the transferability of the numerical and analytical findings to real-world applications.

Zusammenfassung

Die Hauptaufgabe von schwingungsbasiertem Energy Harvesting besteht darin, mechanische Umgebungsenergie in Form von Schwingungen in nutzbare elektrische Energie umzuwandeln. Die gewonnene Energie kann beispielsweise dazu verwendet werden, um energieautarke Sensoreinheiten für Structural Health Monitoring zu realisieren oder um (mobile) energiearme Geräte zu betreiben. Für dieses Anwendungsfeld sind Energy Harvester entscheidend, die in einem breiten Frequenzbereich ausreichend Energie ernten können. Eine Möglichkeit, Energy Harvester mit einer großen Bandweite zu entwerfen, besteht in der Ausnutzung von multistabilen Strukturen. Diese Strukturen weisen Schwingungen großer Amplitude in einem signifikanten Frequenzbereich auf, die von Durchschlägen zwischen den Gleichgewichtslagen resultieren.

Das Ziel dieser Arbeit besteht darin, verschiedene multistabile Energy Harvester Designs zu analysieren, um die Leistungsfähigkeit zu optimieren und Auslegungskriterien zu formulieren. Die betrachteten Designs sind ein bistabiler elektromechanischer Balken, eine bistabile elektromechanische Composite-Platte sowie ein neu vorgeschlagenes Konzept einer multistabilen Platte mit vier Gleichgewichtslagen. Zunächst werden die analytischen Modelle vorgestellt, um die Breitband-Fähigkeit der Designs zu beurteilen. Analytische Methoden werden anwendet, um das zugrunde liegende Bifurkationsverhalten zu untersuchen. Basierend auf diesen analytischen Untersuchungen werden Auslegungskriterien formuliert, die es erlauben geeignete Betriebsbereiche einzuschränken. Numerische Simulationen ergänzen dabei die analytischen Untersuchungen. Die Unterschiede der untersuchten Strukturen bezüglich robusten und effizienten Energy Harvesting werden anhand von numerischen Simulationen für unterschiedliche Anregungsarten hervorgehoben. Die Übertragbarkeit, der analytisch und numerisch gewonnen Erkenntnisse auf realistische Anwendungen, wird experimentell bestätigt.

Contents

1. Introduction

The pursuit of engineers is to enhance performance and effiency of constructions and machines and this demands research for new methods, materials and technologies. In the last years, the field of smart structures has gained more and more importance in this context. Designing structures that are capable of monitoring their own condition is crucial for robustness and reliability. The integration of monitoring capabilities into a structure is the aim of structural health monitoring (SHM). The field of SHM is emerging, as it promises to reduce costs while increasing performance and safety.

This can be seen very well in the field of aerospace. New aircraft structures such as the Boeing 787 Dreamliner or the Airbus A350 XWB are built for the most part with composite materials. Composite materials allow the construction of lighter and, thus, more efficient aircrafts. However, their drawback are invisible damages due to impacts or fatigue. Moreover, the use of composites is a new technological ground and civil aviation authorities demand structural integrity over the life period [45]. Like the aircraft industry [2], many other fields aim to develop and apply SHM systems able to overcome these drawbacks and fulfill the requested specifications.

Structural health monitoring is achieved by designing autonomous wireless sensor networks that capture the health of the structure. To ensure a self-sufficient power supply, energy harvesting systems seem to be promising.

1.1. Energy harvesting

The objective of energy harvesting is to harvest ambient energy. Contrary to the field of renewable energy, the harvested power is of small scale, just sufficient to drive autonomous sensor units. The energy conversion principle in energy harvesting systems is hereby mainly determined by the type

of ambient energy. Possible energy sources are vibrations (kinetic energy), temperature gradients (thermal energy), solar energy (light) or electromagnetic waves (radiation). Well known examples of constructions that exploit these energy sources are windmills and water wheels or even natural processes, where plants and bacteria produce energy from sunlight [5]. Regarding the application and the environmental conditions, a suitable energy source can be selected to perform an effective energy harvest. However, the challenge for engineers is to maximize the harvested power provided by the energy source. Here an appropriate system design and conversion principle are key aspects.

Today, there is much research to bring complete systems into the market. There are also many interesting application fields besides the mentioned aircraft structures. One application is the localization of freight trains. The waggons typically do not have electricity supply. Energy harvesters in this context can be used to drive sensors for localization or monitoring waggons and cargo for smooth logistics and maintenance processes [126]. Another application within a niche are autonomous watches. In 1986 Seiko unveiled the first watch that generates electricity from its own movement in order to drive the quartz crystal. Figure 1.1 shows such a clock unit. The unbalance is excited by the arm movement. This motion is transformed via a gear to obtain a

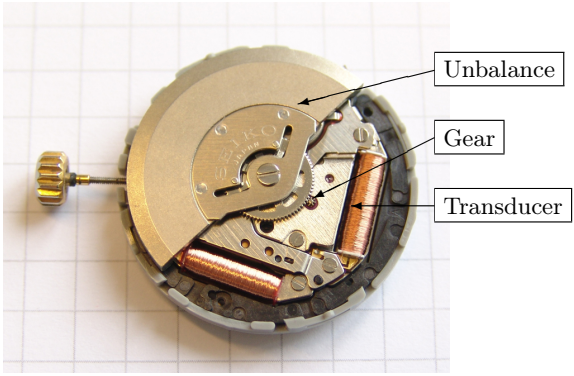

Figure 1.1: A clock unit of a Seiko Kinetic watch as an energy harvester

fast rotation coil. The electrical energy is generated by an electromechanical transducer and stored in a battery. Today, some more companies produce automatic quartz watches although a wide distribution is absent.

The autonomous SEIKO watch is an example for energy harvesting from kinetic energy. This is called kinetic or vibrational energy harvesting. This work deals with the design and description of vibrational energy harvesting systems. For an optimal energy harvest, a mechanical amplification of the source vibrations is desired. This is achieved by mechanical structures, which can typically be described by linear equations. They are tuned to work in their resonance frequency. This allows to increase the excitation amplitude by magnitudes, but only as long as the eigenfrequency is met. However, due to changes in the environmental and excitation conditions, a constant excitation cannot be assumed for most of the application fields. This is an enormous drawback of linear mechanical structures. For the robust electromechanical conversion and, thus, a successful application of energy harvesters, this drawback creates interesting challenges for engineers.

1.2. State of the art

This section gives a brief overview on the research in the area of energy harvesting. A great deal of research has been done in scavenging ambient energy over the last years. This has been achieved with the use of many different transducer mechanisms and structure designs. Linear structural designs have been proposed and investigated for a long time [14]. However, linear energy harvesters only show a narrow frequency bandwidth in which a significant amount of energy can be harvested. Several ideas have been proposed in the literature to overcome the drawback of a narrow bandwidth in linear energy harvesters. The interested reader might consult some review papers for an in-depth introduction to broad bandwidth energy harvesting [28, 85, 123, 136]. Only the common approaches for broad bandwidth energy harvesting will be presented here. One strategy is to design systems with a tunable resonance frequency. This can be achieved actively [3] or passively [61]. This allows to adapt the energy harvester to the changing conditions. Another strat-

egy is to limit the amplitude with mechanical stoppers [83, 130]. For this design, structures with low stiffness are exploited to run at low amplitudes, where the exploitable bandwidth is broader. Another approach is to perform a frequency-up conversion [49, 69] where a mechanical structure with low resonance frequency excites another structure by impacts. This allows to transform low frequency excitations into higher ones, thus acting as a rudimentary gear box. This mechanism allows to operate above the resonance frequency due to the transfer function characteristics. However, both aforementioned methods are accompanied by an increased dissipation resulting from the impact actions. Arranging multiple linear energy harvesters in an array [39] as well as the coupling of simple energy harvesters [81] are other strategies to harvest energy more robustly.

Furthermore, nonlinear effects can be exploited to increase robustness and performance. Nonlinear structures have attracted significant research in the last years due to their capabilities to respond within a larger frequency range with substantial amplitude compared to linear systems. Most of the nonlinear energy harvesters can be distinguished according to the number of stable equilibria. Monostable energy harvesters are capable to respond within a broader frequency range by generating maximally the same amount of power as their linear counterpart [100, 108]. This is due to the characteristic nonlinear frequency response curve. However, this characteristic response yields in two possible oscillation types within the optimal harvesting range: small and large amplitude oscillations. Large amplitudes are desired, since they correspond to the energy output. To compensate this drawback of monostable nonlinear energy harvesters, triggered perturbations can be applied to enhance the overall performance [86]. By these perturbations it can be tried to bring a small amplitude oscillation on the high amplitude branch.

Multistable energy harvesters are a second type of nonlinear structures. The simplest multistability is shown by a bistable system. Exploiting bistable structures for energy harvesting has become an increasing area in research, since they present two benefits concerning broadband energy harvesting.

Firstly, bistable structures allow to operate over a wide frequency band due to the nonlinear characteristics. Secondly, these systems show oscillations

with large amplitudes because of possible snap-through actions between the equilibria. Bistable structures show a particular nonlinear stiffness characteristic that provides several prospects, not only for energy harvesting. Thus, numerous investigations such as designing mechanical filters [96] or morphing structures [9] have been conducted.

Bistable energy harvesting

The following part gives a brief introduction to the different aspects of bistable energy harvesting, concluding with the motivation of the work in a later section. A deeper survey of bistable energy harvesting can be found in the paper by Harne and Wang [55]. Bistable structures are typically composed by a cantilevered beam with a magnet arrangement that creates the bistability [35,109]. Analogously, asymmetric composite plates are employed utilizing the anisotropy of the different plies [7,8,18]. When it comes to the modelling of these structures, the beam is described by a single degree-of-freedom, where the composite plate is described by at least two degrees-of-freedom. The advantages of bistable energy harvesters are described and illustrated in several publications [11, 24, 34, 35, 38, 82, 85, 100, 134]. The bistable oscillator has different oscillation types which partially show large amplitudes over a broad bandwidth. In addition, chaotic oscillations are persistent over a wide frequency domain. By these features, the bistable energy harvester outperforms the linear counterpart for pure harmonic excitations [35] as well as for multi-frequency excitation (white [24, 25, 41, 66, 107] and colored [107] noise). Borowiec et al. [20] show similar results by modifying the amplitude distribution of the noise excitation. This is an outstanding feature of the bistable energy harvester, as Daqaq [27] showed that under different noise excitations the monostable nonlinear energy harvester does not provide any benefit compared to a linear energy harvester. This is also concluded by Barton, Burrow and Clare [13] and Halvorsen [53]. The bistable energy harvester was also shown to harvest energy more efficiently for real-world excitation signals [127], but it seems that this statement cannot be applied to every excitation signal [16]. To conclude, all these investigations reveal the superior

properties of bistable energy harvesters.

Most of the investigations on bistable energy harvesters are performed numerically or experimentally. Indeed, one of the most cited papers by Stanton, McGehee and Mann [109] that considers a bistable energy harvester, is of experimental and numerical nature. The same applies to other frequently cited papers [8,35,38]. The publications on bistable energy harvesting mainly show frequency sweeps to illustrate the frequency broadening such as the work by Mann and Owens [86] for a beam or for a composite plate by Arrieta et al. [8, 10]. The experimental and numerical investigations are established by the underlying nonlinear equations which prevent a closed-form solution. However, for the design and application an understanding of bistable systems such as the derivation of accurate and comprehensible criteria describing the solution's topology is inevitable. To this end, analytic methods need to be exploited. This has been done in few publications for periodic [89] or noise excitation [1] for monostable nonlinear systems. Even though bistable systems have been investigated for a long time, such as in the work by Tseng and Dugundji [122] (1971) or by Holmes [60] (1979), the exploitation of bistable systems for energy harvesting is a rather new field. One early paper from McInnes et al. [90] can be found in 2008. Exploiting bistable systems requires simple and accurate criteria that describe bifurcations and topologies. To this end, some analytical methods have been applied to predict the overall behavior. Harne, Thota and Wang [54] applied the harmonic balance method to obtain a criterion for high energy orbits. In the work by Panyam, Masana and Daqaq [97] various methods were applied to investigate the bandwith of bistable energy harvesters for harmonic excitations. Their work was published during the creation of this work. Grinberg and Gendelman [48] recently proposed a method to analytically define a boundary curve in the phase space that contains all attractors of the simple Duffing equation. In the case of noise excitation, an analytical analysis made with the Melnikov method was carried out by Stanton, Mann and Owens [107]. These few publications show that the area of multistable structures such as multistable energy harvesters is still a vigorous field in which analytical methods are widely used.

1.3. Motivation

This work is motivated by the conducted research in the field of bistable energy harvesting of the last years. Great progress has been made in the experimental and numerical analysis of bistable systems such as prestressed beams or composite plates. However, the fundamental analysis of the different proposed designs seems to be lacking. For instance, composite plates and bistable beams show a similar behavior, but the underlying equations differ greatly. Moreover, most of the publications do not utilize analytical methods to describe the system's bifurcations and solution's topology. However, for the understanding and characterization of the different energy harvester designs an analytic description is inalienable. To this end, this work contains an analysis of the different equation types, the definition of design criteria and the application of possible reductions of these systems.

One aim is to apply and define analytical tools to describe the different structural designs in an accurate way in order to predict the system response such as the capability for broadband energy harvesting. Another aim is to compare the different energy harvester designs concerning their performance and implication for energy harvesting. This will help to span a framework for understanding and designing bistable energy harvesters.

1.4. Outline of the thesis

Chaper 2 gives an introduction to vibration based energy harvesting. It consists in two main parts. The first part deals with the description of the different mechanical structures of energy harvesters. This includes simple monostable and bistable oscillators. The occurring oscillation types are introduced and described by the underlying bifurcations. The second part presents possible electromechanical transducers.

The modelling of different energy harvesters is carried out in Chapter 3. The presented models include typical energy harvester designs. Firstly, the nonlinear model of a prestressed bistable beam is introduced, as it will be important in the later progress of the work. It will, then, be followed by a

model that is extended to an electromechanical beam. An electromechanical bistable composite plate is modelled after that. Finally, a model for a multistable plate is derived.

Chapter 4 introduces and applies various analytical methods to the derived models. The content of this chapter has a key role in the aim of the work. The presented techniques include well known methods such as the multiple-scale method and also less known methods such as the normal form theory. These methods provide a description of the fundamental bifurcations in bistable energy harvesters.

In Chapter 5 the different energy harvester designs will be investigated numerically and compared to the analytical findings. The different characteristics will then be highlighted to convey general design criteria for the different designs.

To complement the analytical and numerical analysis, experimental results will be presented in Chapter 6. This will be done by means of a bistable beam which is studied with and without attached piezoelectric elements. A short experiment with a composite plate will complete the chapter.

Finally, this work concludes with an outlook in Chapter 7.

2. Vibration based energy harvesting

This chapter presents the concept of vibration based energy harvesting. An energy harvester able to harvest electrical energy from ambient vibrations needs to perform two subtasks [15, 36]. The first subtask is to amplify the amplitude of the host structure. This is typically performed by a mechanical structure which exhibits forced vibrations. Besides the amplification, a transformation might be implemented to convert the vibration type, e.g. rotational to translational motion. The second subtask is to convert the dynamical energy into electrical energy by means of an electromechanical transducer. Both subtasks are discussed in this chapter. The subsequent task is to store the energy and to make it available for the electrical consumer. This also includes a power management. This will not be considered in this thesis.

2.1. Mechanical structure

2.1.1. Excitation mechanisms and types

Usually, an energy harvester is mounted on or to a host structure. Typical host structures can be buildings such as bridges or machinery parts like rotating shafts or vibration machine housings. These different kinds of host structures require different strategies for energy exploitation. Most considered energy harvesters are subjected to forced vibrations [15]. These harvesters are described by inhomogeneous differential equations. These systems can either be linear or nonlinear. Otherwise, it is possible to use the mechanism of self-excitation. This concept was analyzed by Heffel [56] by using ultrasonic motors in generator operations. These harvesters have the advantage of operating over a broad bandwidth.

The type of excitation is of great importance for the design of an energy

harvester. In most cases, host structures show specific resonance frequencies. For optimal performance it is convenient to tune the energy harvester to one of these frequencies.

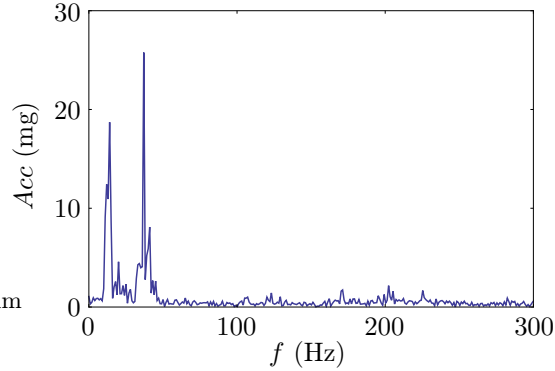

Figure 2.1: Frequency spectrum of a suspension bridge [124]

In most of the models for energy harvesters it is, therefore, assumed that the excitation is purely harmonic. In other papers [107] random excitation is supposed. However, as Fig. 2.1 shows, most of the structures posses a spectrum which is located between an harmonic and a purely random excitation. According to the predominant excitation type, the design of the mechanical structure has to be defined. This will be discussed in the next section.

2.1.2. Structural design

The task of the mechanical structure of the harvester is to increase the amplitude of the host structure. Therefore, structures which are described by a linear or a nonlinear ordinary differential equation can be exploited. In general, linear structures posses a high efficiency, i.e. they show a large magnification of the excitation amplitude, if they are excited at their resonance frequency [99]. However, the efficiency of the energy harvester significantly drops as soon as this frequency is not met. This can be avoided by resonance tuning [21, 22, 136], which may lead to semiactive structures. Taking this drawback into account, nonlinear energy harvesters have attracted significant attention over the past years.

Nonlinear monostable energy harvesters allow to extend the bandwidth

thanks to their dynamical features. The characteristic frequency response of these harvesters allows to operate them over a broader bandwidth even though the possible output power is not increased [100]. In contrast to monostable structures, nonlinear multistable structures show large amplitude oscillations due to the snap-through actions which outperform monostable energy harvesters.

In the physical system, such a nonlinear characteristic can be implemented by external arrangements, e.g. using springs or magnets or by structural nonlinearity such as implemented by the lay-up of the lamina plies of composite plates. Other possibilities to introduce nonlinear behavior are geometric nonlinearities [40, 78]. Monostable and multistable structural designs will be briefly discussed in the following sections. In addition, the concept of multimodal energy harvesting devices has been proposed [74, 114, 132, 133]. These systems typically have multiple degrees of freedom which are either coupled nonlinear systems or uncoupled arrays. Since they are composed by nonlinear subsystems, these multimodal systems will not be discussed explicitly. An overview on the different structural designs including their performance is given by Tang, Yang and Soh [32].

A general introduction to nonlinear systems can be found in the book by Wagg and Neild [128]

Monostability

A monostable oscillator has only one stable equilibrium similar to a linear oscillator. By introducing nonlinear stiffness coefficients in the differential equation, a frequency response curve as illustrated in Fig. 2.2 can be found. Depending on the nonlinear stiffness coefficients, a softening or harding behavior is obtained. The left bent curve reveals a softening behavior, whereas the right bent curve corresponds to hardening. The solid lines represent the stable solutions branches, whereas the dashed line corresponds to the unstable branch. The interesting solution of this frequency response curve is the resonant upper stable branch for the amplitude $\hat{a}$. This branch is often referred to as high energy orbit. This branch can also show a broader bandwidth

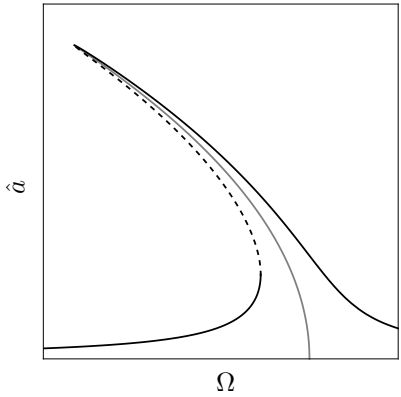

Figure 2.2: Frequency response relation of a monostable DUFFING oscillator with softening

compared to linear systems. There are two possible solutions in the frequency domain in which the upper branch shows maximal amplitude: non-resonant small and large amplitude oscillations. For energy harvesting, only the high resonant branch is desired. Unfortunately, the branch to which the solution is attracted depends on the initial conditions. Consequently, this leads to a probability distribution for each solution branch which was analyzed by QUINN et al. [99]. Considering this drawback of monostable structures, many researchers exploit multistable structures.

Multistability

Multistable structures posses multiple equilibria. Thus, the solution space increases compared to monostable systems. A benefit of using multistable structures for the mechanical part of an energy harvester are the snap-through actions. The snap-through oscillations show a large amplitude which results in a high energy harvest. Due to its nonlinear characteristics, it is also able to respond within a broad bandwidth showing a significant amplitude. Different designs for multistable structures have been proposed in the literature. The majority of the proposed designs are bistable [55]. This is justified by the fact that bistable systems exhibit both of the mentioned benefits: bandwith and large amplitude. Other concepts such as tristable energy harvesters can

be found but they are rather rare [120, 135]. In any case, these structures do not seem to bring any improvement concerning broad bandwidth energy harvesting.

2.1.3. Bistable DUFFING oscillator

This section introduces the bistable DUFFING oscillator. This periodically forced oscillator allows to describe the main features of a multistable system such as basins of attraction, multiple solutions or chaotic behavior. Furthermore, the mechanical structures of the predominantly proposed multistable energy harvesters can be reduced to the bistable DUFFING equation. Thus, a profound understanding of this oscillator conveniently allows to analyze energy harvesters with more complexity. An interesting numerical and experimental investigation on the bistable DUFFING oscillator can be found in the paper by WAITE, VIRGIN and WIEBE [129] and in the publication by TODD and VIRGIN [118].

Oscillation types

Figure 2.3 shows a simple bistable structure consisting of an excited bistable prestressed beam. This structure can be described by a single equation. The simplest way to this is by using the bistable DUFFING equation[1]

$$\ddot{x}(t) + \mu\,\dot{x}(t) - \alpha\,x(t) + \beta\,x^3(t) = \ddot{e}(t). \tag{2.1}$$

A harmonic excitation $e(t) = \sin \Omega t$ will be used for illustration in this chapter. The bistable DUFFING equation is a special case of the equations investigated by DUFFING [31]. It has a negative linear coefficient α and a positive cubic

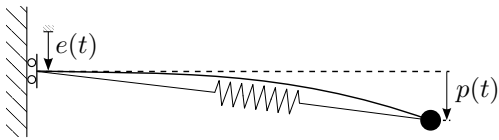

Figure 2.3: A prestressed beam as a structure describes by the bistable DUFFING equation

[1] Named after Georg DUFFING (1861-1944), German engineer and inventor

coefficient β in the restoring force. The oscillation types of a bistable oscillator are described my means of its potential energy

$$\mathcal{U} = -\frac{1}{2}\alpha\, x^2 + \frac{1}{4}\beta\, x^4. \tag{2.2}$$

Figure 2.4 illustrates the double-well potential $\mathcal{U}$. As indicated, this potential

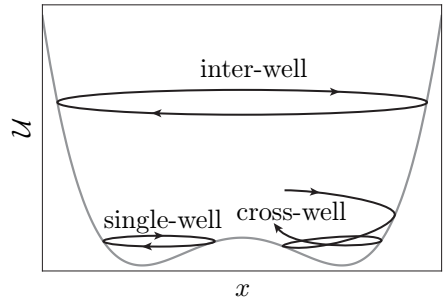

Figure 2.4: Bistable potential well with the corresponding oscillation types

shape leads to three distinctive oscillation types. Oscillations about a stable equilibrium are called *single-well* or *intra-well* oscillations. These oscillations are periodic. Single-well oscillations are similar to the ones observed in nonlinear monostable systems. *Cross-well* oscillations are vibrations between the wells. They show intermittency or chaotic behavior. This can be shown by the Poincaré-Bendixson theorem [115]. The Lyapunov exponent [91,104] can be used to distinguish between both oscillation manners.

It is not reasonable to calculate the Lyapunov exponent for a large amount of time signals because of its limit value character. A chaotic attractor typically has an infinite set of unstable periodic attractors [76]. Thus, it is able to show infinite diverse periodic motions composed of multiple frequencies. This is an interesting feature regarding energy harvesting over a wide bandwidth.

The last oscillation type are vibrations about the unstable equilibrium. They are called *inter-well* oscillations. These oscillations are periodic and most favourable for energy harvesting; they show large amplitudes incorporating, therefore, the highest energy.

Figure 2.5 illustrates the time signal and the phase space for the three different oscillation types. The phase space also depicts the Poincaré[2] map [71]

[2]Named after Henri Poincaré (1854-1912), French mathematician and physicist

given by the black dots. The periodicity is clearly visible in the single-well and inter-well oscillations by the single point, whereas the cross-well oscillations show scattered points in the POINCARÉ map. Figure 2.6 shows the amplitude spectrum of the time signals depicted in Fig. 2.5. The spectrum reveals the different frequency components. As indicated in Fig. 2.6a, single-well oscillations show characteristics similar to a linear system. The excitation frequency shows the highest amplitude, while the higher harmonics are present with smaller amplitudes. The cross-well oscillation (Fig. 2.6b) spectrum reveals the chaotic attractor, as a large set of frequencies are contained within the time signal. However, the amplitude at the excitation frequency Ω shows the highest amplitude. The inter-well spectrum is shown in Fig. 2.6c. Its particular characteristic is the occurrence of the third harmonics.

The equilibria positions of Eqn. (2.1) are defined by

$$x_s = \pm\sqrt{\frac{\alpha}{\beta}}. \tag{2.3}$$

If the bistable potential shape is asymmetric, a quadratic term appears in the restoring force. The eigenfrequency within a stable equilibria reads

$$\omega = \sqrt{2\alpha}. \tag{2.4}$$

Due to the various possible oscillations that can be observed in bistable systems, the initial conditions need to be considered. This is a major difference compared to linear systems, which show only one solution type, thus initial conditions play a minor role for linear systems. A mathematical definition that allows to analyze the time signal regarding each oscillation type is introduced to consider the effect of the initial conditions. Afterwards, the domains of attraction are discussed.

Characteristic values

For the characterization of a time signal it is convenient to introduce a characteristic value by which the oscillation type can be identified. For the distinction between the three possible oscillation types, a simple value can be

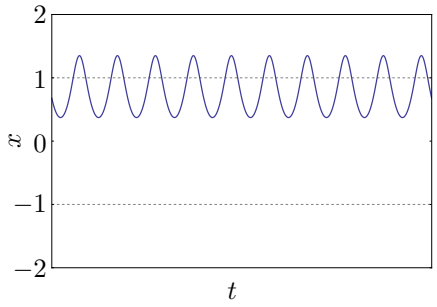

(a) Time signal for single-well oscillations ($\Omega = 1.2, \hat{e} = 0.07$)

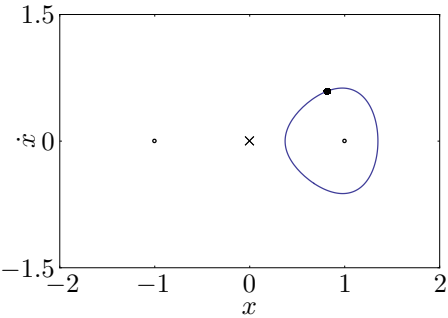

(b) Phase diagram for single-well oscillations

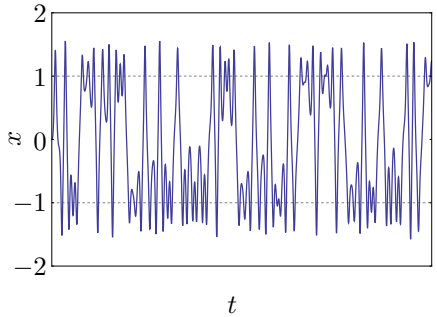

(c) Time signal for cross-well oscillations ($\Omega = 1.2, \hat{e} = 0.2$)

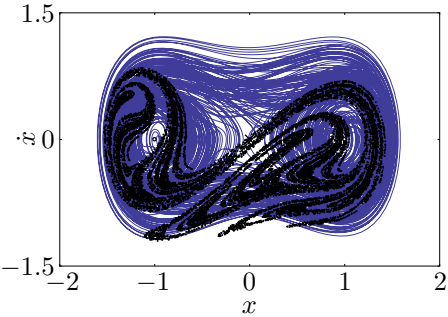

(d) Phase diagram for cross-well oscillations

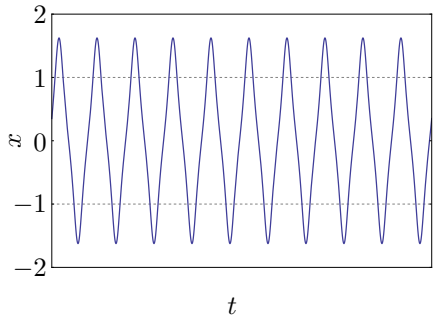

(e) Time signal for inter-well oscillations ($\Omega = 0.8, \hat{e} = 0.2$)

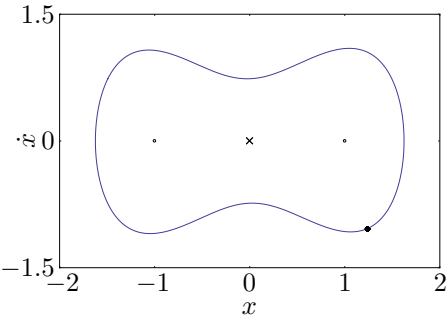

(f) Phase diagram for inter-well oscillations

Figure 2.5.: Different oscillation types for $\alpha = 1, \beta = 1, \mu = 0.05$

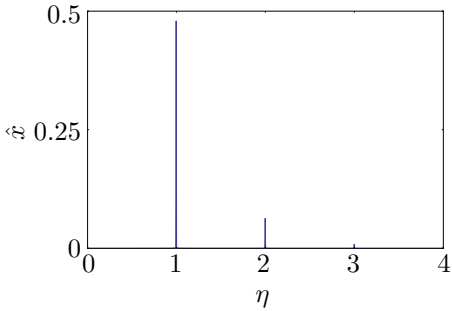

(a) Amplitude spectrum for single-well oscillations ($\Omega = 1.2,\ \hat{e} = 0.07$)

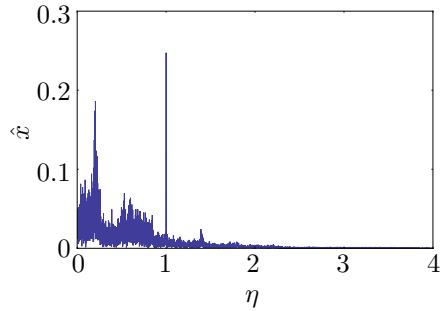

(b) Amplitude spectrum for cross-well oscillations ($\Omega = 1.2, \hat{e} = 0.2$)

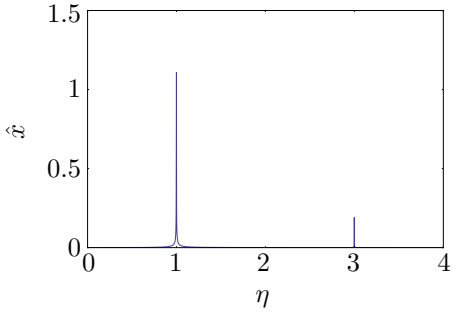

(c) Amplitude spectrum for inter-well oscillations ($\Omega = 0.8, \hat{e} = 0.2$)

Figure 2.6.: Amplitude spectra for different oscillation types ($\alpha = 1,\ \beta = 1, \mu = 0.05, \eta = \omega/\Omega$)

defined

$$\Psi = \frac{1}{n}\sum_{i}^{n} LA_i \quad \text{with} \quad LA_i = \begin{cases} 1, \text{ if } |\hat{a}_i - \hat{a}_{i+1}| \geq 2\,|x_\mathrm{s}| \\ 0, \text{ other} \end{cases} \tag{2.5}$$

An illustration of the calculation of Ψ is given in Fig. 2.7. The large amplitude ratio Ψ states the ratio of snap-throughs within a time signal by considering successive extrema. Thus, $\Psi = 0$ for single-well, $0 < \Psi < 1$ for cross-well and $\Psi = 1$ for inter-well oscillations. In addition, further distinctions can be made to describe each oscillation type in more detail. For instance, autocorrelation

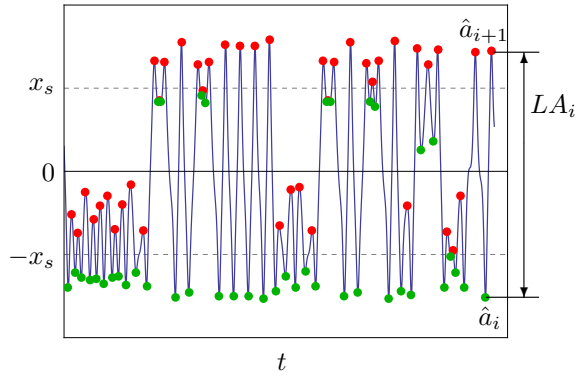

Figure 2.7: Illustration for the calculation of Ψ ($\alpha = 1, \beta = 1, \mu = 0.05$, $\hat{e} = .15$, $\Omega = \sqrt{2}$)

or the LYAPUNOV exponent can be calculated to analyze intermittency of cross-well oscillations, but this is time consuming because of its long numerical calculation and the knowledge is of little importance concerning the energy harvest. It is reasonable to state the ratio $\Psi = 1$ for a specific oscillation frequency to distinguish between sub- and super harmonic frequencies.

Basin of attraction

The multiple solutions of nonlinear systems stress the importance of initial conditions. Various oscillation types can occur depending on the initial conditions even though the excitation remains constant. Therefore, it is convenient to regard the basins of attraction. The basins of attraction are regions in the phase space where every initial condition within the domain is attracted to a specific solution. The sum of all initial conditions is thus called basin of attraction. Many systems, such as the VAN DER POL [57] oscillator or the monostable DUFFING oscillator [99], have basins with smooth boundaries. Chaotic oscillations typically have a scattered attractor, and thus no smooth and closed basin can be defined. The basins of attraction for the driven DUFFING oscillator (Eqn. 2.1) are shown in Fig. 2.8 for different forcing amplitudes $\hat{e}$ with excitation $e(t) = \hat{e} \sin \Omega t$. The construction of these graphs was done with the integration of Eqn. (2.1) over a long time span using `Mathematica`. The ratio Ψ was calculated for each shown initial condition. The white and

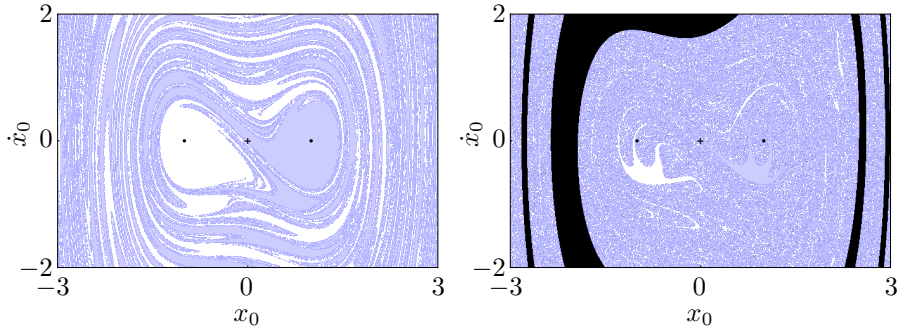

(a) $\hat{e} = 0.05$ **(b)** $\hat{e} = 0.1$

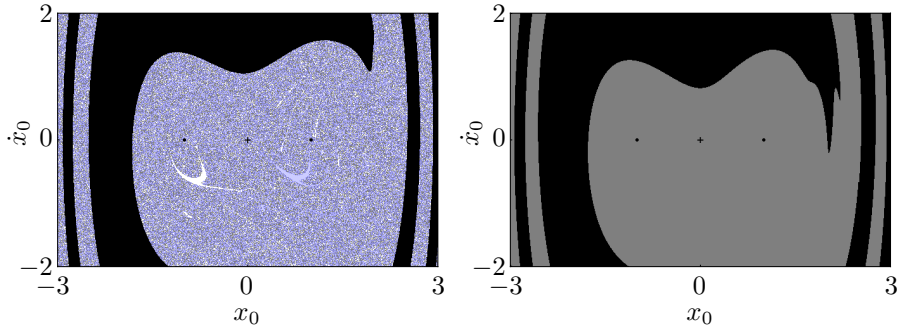

(c) $\hat{e} = 0.15$ **(d)** $\hat{e} = 0.1525$

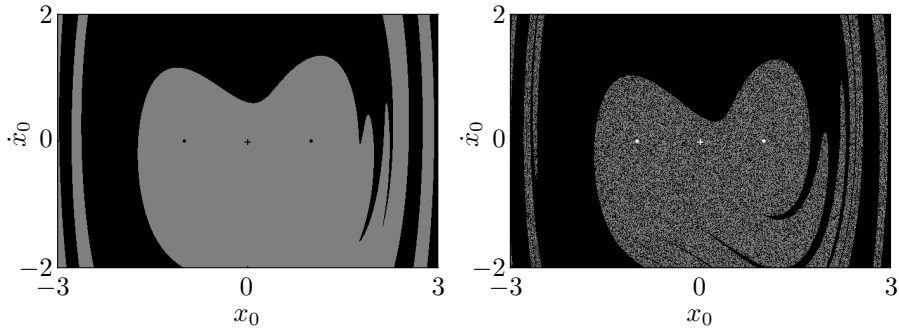

(e) $\hat{e} = 0.2$ **(f)** $\hat{e} = 0.235$

Figure 2.8.: Basin of attraction for $\alpha = 1, \beta = 1, \mu = 0.05, \Omega = \sqrt{2}$: White and light blue dots indicate single-well about the two stable equilibria. Black (gray) dots indicate inter-well (cross-well) oscillations.

light blue domains indicate the attractor of single-well oscillations about one of the two stable equilibria. The gray domain represents cross-well and the black dots inter-well oscillations. The graphs reveal the scattered cross-well attractor. An increased excitation amplitude leads to a more solid basin until it becomes united in Fig. 2.8d. In contrast, for a low excitation amplitude $\hat{e}$ the attractor for inter-well oscillations shows smooth boundaries. With a further increase of the amplitude, the basin branches out until it becomes a scattered attractor (Fig. 2.8f). The figure illustrates the influence of the initial conditions on the oscillation type: the more energy is imposed to the system by the initial conditions, the likelier it reaches high energy orbits (inter-well oscillations). Not only the energy level affects the resulting oscillation type, but also the phase. This is why the black domain shows the spiral shape.

Response map

The resulting oscillation type can be shown depending on the excitation parameters Ω and $\hat{e}$. This leads to a response map, shown in Fig 2.9.

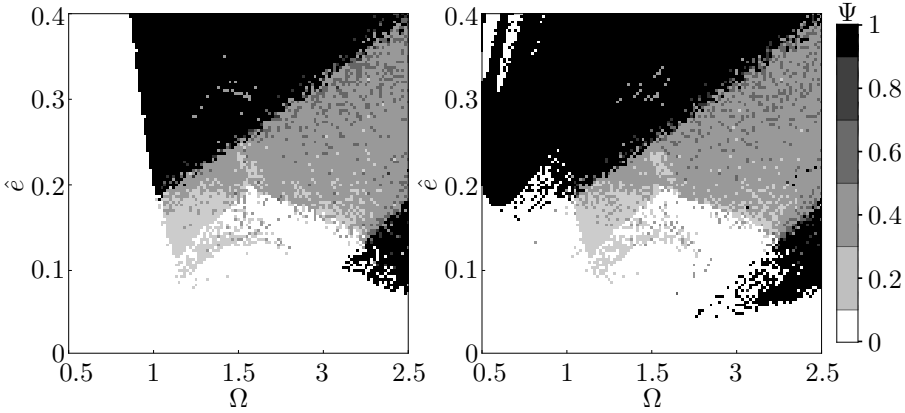

(a) $x_0 = x_s,\ \dot{x}_0 = 0$ **(b)** $x_0 = 0, \dot{x}_0 = 0$

Figure 2.9.: Large amplitude ratio Ψ as a function of Ω and $\hat{e}$

The maps reveal the three oscillation types. For low excitation amplitudes

and frequencies only single-well oscillations are obtained. The gray shaded domain reveals the excitation parameters for which cross-well oscillations are obtained. Inter-well oscillations are represented by black points. The two maps reveal the influence of the initial conditions on the topology. If the initial condition is set to the stable equilibrium x_s and $\dot{x}_0 = 0$, the system contains minimal initial energy. This leads to a smaller domain for inter-well oscillations. Otherwise, if the initial condition leads to an enhancement of the initial system energy, it is more likely to reach the inter-well orbit. Therefore, the domain for $\Psi = 1$ is increased as demonstrated in Fig. 2.9b. This coherency was also shown in the context of the basins of attraction in Fig. 2.8. The fact that the inter-well domain is minimal for the initial condition $x_0 = x_s, \dot{x}_0 = 0$ can be shown by numerical simulation. For energy harvesting a large inter-well domain is desired. Thus, the response map for the zero energy initial condition (Fig. 2.9a) provides a conservative estimation of the domain where inter-well oscillations can be obtained.

Figure 2.9a not only provides a conservative estimation, it also allows to illustrate the underlying bifurcation behavior. The transition between the different domains are affected by the bifurcation type. In Fig. 2.9a, a sharp boundary which emerges from the eigenfrequency $\omega = \sqrt{2\alpha}$ limits the left edge of the inter-well domain. In contrast, the inter-well domain is bounded towards cross-well oscillations by a diffuse band. To illustrate this behavior a bifurcation diagram for a fixed amplitude $\hat{e} = 0.3$ is depicted in Fig. 2.10. The diagram is obtained by means of analytical methods presented in Chapter 4. The black curves represent the regular frequency response relation for single-well oscillations and the blue ones represent the inter-well amplitudes. As proven by the FLOQUET theory, the dashed lines represent the unstable branches. Numerical results are indicated by the gray points. The deviation between numerical and analytical results arises from the approximative character of the analytic methods. When there is zero initial energy the solution follows the lower branches. As the frequency is increased, the oscillation follows the non-resonant saddle S_n until it loses stability at the lower saddle-node bifurcation, b_{snU}, giving way to the large-amplitude saddle S_I at about $\Omega = 1$. The oscillation follows the large amplitude branch until

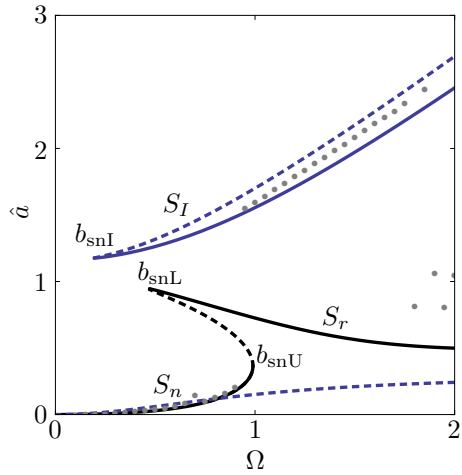

Figure 2.10: Bifurcation diagram for $\hat{e} = 0.3$. ($\alpha = 1, \beta = 1, \mu = 0.05$)

it disappears in a period-doubling bifurcation leading to chaotic oscillations. For even higher excitation frequencies, the solution would follow the resonant saddle S_r. However, this is not shown in the graph. In the case of an initial condition which introduces energy to the system, the branch S_I can be obtained for an excitation frequency below the bifurcation value b_{snU}.

2.2. Electromechanical transducers

The electromechanical transducers accomplish the second subtask of an energy harvester. Common transducers are based on the piezoelectric, electromagnetic or the electrostatic effect. The piezoelectric effect generates electrical energy from the strain of the mechanical structure, whereas the electrostatic and electromagnetic transducers exploit the velocity and the displacement of the structure respectively. An overview on these conversion principles can be found in various contributions [15, 98, 105]. A comparison between these conversion mechanisms regarding its applicability has been carried out in several publications [72, 103]. All of these transducers have been applied in various scenarios, whereby an optimal operation regime is determined by several boundary conditions. One criterion consists in the environmental conditions

and the excitation parameters. Other criteria are the energy density and the power density [46], which define the ability for miniaturization, e.g. for integrated circuits (IC). Furthermore, the strain or stress amplitudes which result from the mechanical structure need to be considered.

Compared to the other transducers, piezoelectric materials only endure small strain amplitudes but, still, they are much more compact than electromagnetic actors [65]. If there are no constraints in size, the electromagnetic transducer is the most efficient [15]. However, if size is of importance, the electromagnetic transducer decreases its performance.

Electrostatic converters harvest energy by their mechanically varied capacity. Therefore, they require a power source for creating an initial electrical field. Another drawback is the synchronisation between the deformation cycle and the energy extraction.

In this work the piezoelectric will be exploited to generate electrical energy. Piezoelectric transducers are shown to be more efficient under low frequency excitations compared to electromagnetic ones [16]. However, many observations within this work can be applied to the use of electromagnetic transducers since the equations of motion show the same structure. An introduction to piezoelectric energy harvesting can be found in the book of Erturk and Inman [36].

3. Nonlinear energy harvesters

In this chapter some multistable energy harvester designs are derived in order to investigate their broadband capabilities in later Chapters. To this end, not only the electromechanical equations are derived but also the equations describing the underlying mechanical structure.

3.1. Bistable beam

3.1.1. Modelling

This section concerns the derivation of the equations of motion of a bistable prestressed beam. Even though no electromechanical transducer will be considered to this end, the model is able to describe the characteristics of a simple bistable energy harvester. The result will be a scalar equation of motion.

A typical energy harvester is mounted on a vibrating structure. Therefore, a base-excited cantilevered beam as shown in Fig. 3.1 will be considered. The movement of the base is characterized by the function $e(t)$. The beam is described in terms of YOUNG's modulus E, the cross-sectional area A, the mass density ρ, the length l and the structural damping parameter μ. A particle with the mass m is attached to the tip of the beam. The bistable characteristic is implemented by a spring arrangement. The massless spring is specified by the linear stiffness k and the initial undeformed length l_0.

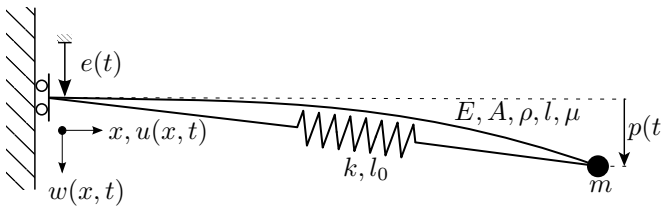

Figure 3.1: Prestressed beam as a bistable system

The deformation of the beam is described by the functions $u(x,t)$ and $w(x,t)$. Both functions depend on the coordinate x. In the derivation of the equation of motion the beam will be discretized. To this end, the deflection of the tip is described by the generalized coordinate $p(t)$ as indicated in Fig. 3.1.

3.1.2. Kinematics

The nonlinear kinematic relations need to be considered for this nonlinear problem. Due to the large deformations, it is insufficient to apply the linear EULER[1]-BERNOULLI[2] beam theory. Therefore, the full kinematic relations considering longitudinal and transversal deformation have to be taken into account. However, without any assumption, this will end in equations with coupled longitudinal and transversal deformations. This can be remedied by supposing an inextensible neutral axis. This assumption is physically justified for usual beam structures [37, 117] and also a part of the EULER-BERNOULLI hypothesis. Thus, the following kinematic relation can be formulated [33, 93]

$$\varepsilon_s^0 = \sqrt{\left(u'(x)+1\right)^2 + w'^2(x)} - 1 = 0. \tag{3.1}$$

This assumption is common for slender structures such as in EULER's elastica [117]. The superscript 0 denotes the neutral axis. Note that the strain ε_s^0 is hereby defined in the axial beam coordinate s. The strain formulation can be rearranged to

$$\varepsilon_x^0 = u'(x) = \sqrt{1 - w'^2(x)} - 1 \tag{3.2}$$

which describes the strain along the neutral axis in the x-coordinate. The slope of a beam element of infinitesimal length reads

$$\varphi = \tan^{-1}\frac{\mathrm{d}x + \mathrm{d}u}{\mathrm{d}w} = \tan^{-1}\frac{1+u'(x)}{w'(x)}. \tag{3.3}$$

[1]Leonhard Euler (1707-1783), Swiss mathematician and physicist
[2]Daniel Bernoulli (1700-1782), Swiss mathematician and physicist

With this expression (3.3) and the strain formulation (3.2), the nonlinear curvature $\frac{\mathrm{d}\varphi}{\mathrm{d}s}$ is defined by [58]

$$\kappa = \frac{\mathrm{d}\varphi}{\mathrm{d}s} = \frac{\mathrm{d}\varphi}{\mathrm{d}x}\frac{\mathrm{d}x}{\mathrm{d}s} = \frac{w''(x,t)}{\sqrt{1-w'^2(x,t)}}. \tag{3.4}$$

With this expression for the curvature, the strain is given by

$$\varepsilon_s = -z\kappa = -z\frac{w''(x,t)}{\sqrt{1-w'^2(x,t)}}. \tag{3.5}$$

3.1.3. Derivation of the equation of motion

The equation of motion of the presented prestressed beam (Fig. 3.1) is derived in this section in discretized form. This is done by directly using the LAGRANGE's equation instead of carrying out the variational calculus from HAMILTON's principle. For doing so, the LAGRANGEian $\mathcal{L}$ will be derived and discretized using the RITZ discretization [52, 101]. The LAGRANGEian $\mathcal{L}$ is defined by

$$\mathcal{L} = \mathcal{T} - \mathcal{U}, \tag{3.6}$$

with $\mathcal{T}$ being the kinetic and $\mathcal{U}$ the potential energy. The RAYLEIGH dissipation function [47] will be introduced to account for the damping. Thus, the LAGRANGE equation reads

$$\frac{d}{dt}\frac{\partial \mathcal{L}}{\partial \dot{p}_i} - \frac{\partial \mathcal{L}}{\partial p_i} + \frac{\partial \mathcal{D}}{\partial \dot{p}_i} = 0. \tag{3.7}$$

In the following, the functionals $\mathcal{T}$,$\mathcal{U}$ and $\mathcal{D}$ will be derived.

Kinetic energy $\mathcal{T}$

The expressions for the kinetic energy [52]

$$\mathcal{T} = \frac{1}{2}\rho A \int_0^l \left(\dot{w}(x,t) + \dot{e}(t)\right)^2 \mathrm{d}x + \frac{1}{2}m\left(\dot{w}(l,t) + \dot{e}(t)\right)^2 \tag{3.8}$$

contains two terms. The first expression accounts for the kinetic energy of the beam and the second term for the kinetic energy of the tip mass.

Potential energy $\mathcal{U}$

The expression for the potential energy is more involved. The energy contains two terms

$$\mathcal{U} = \mathcal{U}_b + \mathcal{U}_s. \tag{3.9}$$

The potential energy of the beam $\mathcal{U}_b$ is defined by

$$\mathcal{U}_b = \int_V \int_\varepsilon E\varepsilon_s \mathrm{d}\varepsilon_s \mathrm{d}V = \frac{1}{2}\int_V E\varepsilon_s^2 \mathrm{d}V, \tag{3.10}$$

where the parameter $V = Al$ specifies the volume of the beam. If Eqn. (3.5) is inserted into Eqn. (3.10) and the integration is carried out over the cross-section, the expression becomes

$$\begin{aligned}\mathcal{U}_b &= \frac{1}{2}\int_0^l \int_A Ez^2\kappa^2(x,t)\,\mathrm{d}A\mathrm{d}x \\ &= \frac{1}{2}EI\int_0^l \kappa^2(x,t)\,\mathrm{d}x \\ &= \frac{1}{2}EI\int_0^l \frac{w''^2(x,t)}{1-w'^2(x,t)}\mathrm{d}x\end{aligned} \tag{3.11}$$

with $EI = \int_A Ez^2 \mathrm{d}A$ being the bending stiffness. The potential energy of the spring reads

$$\mathcal{U}_\mathrm{s} = \frac{1}{2}k\triangle {l_s}^2, \tag{3.12}$$

with $\triangle l_s$ being the elongation of the spring which is defined by

$$\triangle l_s = \sqrt{w(l,t)^2 + \left(\int_0^l u'(x)\,\mathrm{d}x + l\right)} - l + l_0. \tag{3.13}$$

Rayleight dissipation function $\mathcal{D}$

The dissipation function is defined in a similar way as the kinetic energy [119], thus it is defined by

$$\mathcal{D} = \frac{1}{2}\mu A\rho \int_0^l \dot{w}^2(x,t)\mathrm{d}x. \tag{3.14}$$

This is a convenient assumption, since the mass proportionality is dominant for lower excitation frequencies, whereas the damping becomes proportional to the stiffness for higher frequencies [88].

Ritz discretization

Up to now, the energy expressions are defined in terms of the unknown function $w(x,t)$. The prestressed beam will now be discretized by expanding

$$w(x,t) = \sum_i W_i(x) p_i(t). \tag{3.15}$$

With this *ansatz* the solution $w(x,t)$ is projected on shape functions $W_i(x)$ which need to fulfill the geometric boundary conditions [52]. The functions $p_i(t)$ are the generalized coordinates. The geometric boundary conditions for the cantilevered beam are

$$\begin{aligned} &w(0,t) = 0, \\ &\frac{\partial w(0,t)}{\partial x} = 0. \end{aligned} \tag{3.16}$$

If more degrees of freedom are considered, it is convenient to use the orthogonal Legrende polynoms as shape functions. This simplifies the derivation. However, in the present derivation only the lowest mode is of interest. It is, therefore, enough to consider a shape function which considers the first bending mode. Thus, the following *ansatz* will be used

$$w(x,t) = W_1(x) p_1(t), \tag{3.17}$$

with

$$W_1(x) = \frac{x}{l} - \frac{1}{\pi} \sin\left(\frac{\pi}{l} x\right). \tag{3.18}$$

Equation (3.18) results from the exact deflection curve of a buckled beam where the load passes through the root [117]. This load case is similar to the beam shown in Fig. 3.1. Finally, the equation of motion for the prestressed beam (3.19) is obtained when the *ansatz* (3.17) is inserted into (3.7) by using

the functionals $\mathcal{T}$,$\mathcal{U}$ and $\mathcal{D}$ (3.8, 3.9 and 3.14).

$$\begin{aligned}\frac{\left(2\pi^2-9\right)Al\rho+6\pi^2 m}{6\pi^2}\ddot{p}(t)+\mu\frac{\left(9-2\pi^2\right)lA\rho}{6\pi^2}\dot{p}(t)\\ +\frac{\pi^2EI-kl^2l_0}{2l^3}p(t)+\frac{20\pi^2EI+kl^2(2l-19l_0)}{16l^5}p^3(t)\\ =\frac{\left(\pi^2-4\right)Al\rho+2\pi^2 m}{2\pi^2}\ddot{e}(t)\end{aligned} \tag{3.19}$$

This equation approximates the dynamics of the prestressed beam about its first mode. The bistable domain of Eqn. (3.19) is of interest. Bistability is obtained when the linear term becomes negative. This leads to the critical buckling load

$$F_{\mathrm{cr}}=\frac{\pi^2EI}{l^2}. \tag{3.20}$$

Thus, the prestress load needs to fullfill the condition

$$kl_0\geq\frac{\pi^2EI}{l^2}, \tag{3.21}$$

such that Eqn. (3.19) describes a bistable oscillator. This special case will be considered in the following.

3.1.4. Nondimensionalization and parameter reduction

Regardless of the chosen shape function (3.18), Eqn (3.19) can be written as

$$\ddot{x}(t)+\mu\,\dot{x}(t)-\alpha\,x(t)+\beta\,x^3(t)=\hat{e}\;\ddot{e}(t). \tag{3.22}$$

The parameters α and β describe the stiffness of the system, μ the damping and $\hat{e}$ the mass excitation parameter. For the bistable domain, all the parameters are limited by

$$\mu,\alpha,\beta,\,\hat{e}>0. \tag{3.23}$$

Equation (3.22) is known as the bistable Duffing equation which was already introduced in Chapter 2. For many investigations, it is reasonable to reduce

the number of parameters and nondimensionalize the equation. This can be done by performing a dimension analysis and reduction [59]. This results in the following transformations for time and deflection

$$\begin{aligned} x &= y\ x_s, \\ t &= \tau/\sqrt{\alpha}, \end{aligned} \tag{3.24}$$

where the stable equilibria x_s are given by

$$x_s = \sqrt{\frac{\alpha}{\beta}}. \tag{3.25}$$

With these transformation the following equation is obtained

$$\ddot{y}(\tau) + \bar{\mu}\ \dot{y}(\tau) - y + y^3(\tau) = \hat{\bar{e}}\ \ddot{\bar{e}}(\tau), \tag{3.26}$$

where the substitutions

$$\begin{aligned} \mu &= \bar{\mu}\ \sqrt{\alpha}, \\ \hat{e} &= \hat{\bar{e}}\ x_s, \end{aligned} \tag{3.27}$$

are applied. By doing so, it is possible to reduce the number of three parameters to only one on the left hand side. This means that it is possible to obtain solutions that are invariant for changing stiffness parameters but only depend on the damping parameter $\bar{\mu}$. This reduction can be used for analytical investigations and to minimize the effort in the numerical analysis.

Another representation of the DUFFING equation is the transformation by the eigenfrequency $\omega = \sqrt{2\alpha}$ about the stable equilibria. Here, the transformations for distance and time are

$$\begin{aligned} x &= \frac{y}{2}\ x_s, \\ t &= \tau\ /\sqrt{2\alpha}. \end{aligned} \tag{3.28}$$

With these transformations, the following equation is obtained

$$\ddot{y}(\tau) + \bar{\mu}\dot{y}(\tau) - \frac{1}{2}y(\tau) + \frac{1}{8}y^3(\tau) = \hat{f}\ \ddot{\bar{e}}(\tau), \tag{3.29}$$

with

$$\bar{\mu} = \mu \frac{1}{\sqrt{2\alpha}}, \qquad \hat{f} = \hat{e} \frac{2}{x_s}. \tag{3.30}$$

This representation (3.29) is convenient since resonance occurs for the excitation frequency $\bar{\Omega} = 1$.

3.2. Bistable electromechanical beam

3.2.1. Modelling

At this point, a simple model for a bistable electromechanical beam will be derived. A piezoelectric patch attached to the structure will be used for the generation of electrical energy. The equations of motion will be derived by using the LAGRANGE equation. The considered prestressed electromechanical beam is shown in Fig. 3.2. The mechanical part of the equation is identical to the one derived in Section 3.1. Therefore, the kinetic energy $\mathcal{T}$ and the potential energy $\mathcal{U}$ for the structure are already given. For the electromechanical beam, piezoelectric patches are attached to the host structure. The elements are symmetrically bonded to the beam on both sides. On the one hand, this ensures a centered neutral plane that keeps the kinematics simple. On the other hand, the power output is increased.
Each piezoelectric patch is connected to an resistance R. The introduced electrical degrees of freedom are, therefore, the voltages $v_i(t)$ measured over the resistance R, see Fig. 3.2. Figure 3.3 shows the geometry of the electrome-

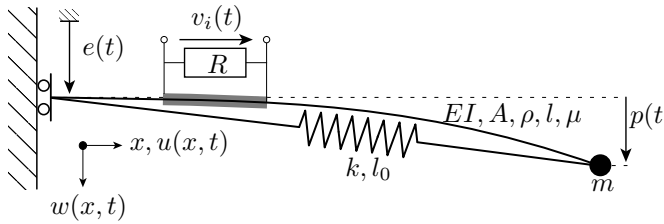

Figure 3.2: Prestressed electromechanical beam as a simple bistable energy harvester

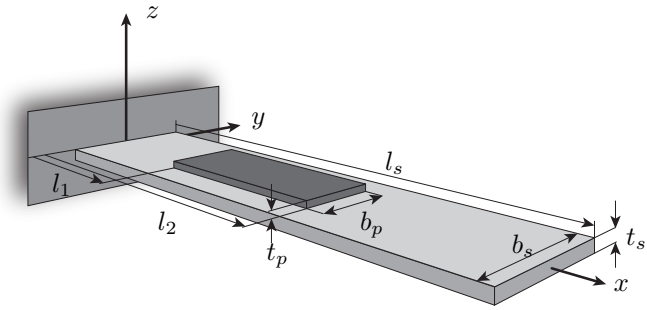

Figure 3.3: Geometry of the electromechanical beam

chanical beam in detail. The structure has the dimensions l_s, b_s and t_s. The considered beam has two symmetrically attached piezoelectric elements. One on the upper and one on the lower side (not shown here). The geometry is described by the parameters l_1, l_2, b_p, t_p as illustrated in Fig. 3.3.

3.2.2. Derivation of the equation of motion

Energy expressions

The equations of motion will be derived using the LAGRANGE's equation. These equations result from HAMILTON's principle. Since non-conservative electrical displacement appears within the piezoelectric elements, HAMILTON's principle needs to be expanded to account for these terms. This has been deduced explicitly by WOLF [70]. Only the result will be presented here. The extended HAMILTON's principle is given by

$$\delta \int_{t_1}^{t_2} (\mathcal{L} \ + \mathcal{W}_e) \, \mathrm{d}t = 0. \tag{3.31}$$

The functional $\mathcal{W}_e$ includes the work of external electrical forces. The equations of motion can now be obtained applying LAGRANGE'S equation. With dissipative terms and Eqn. (3.31) these equations yield

$$\frac{\mathrm{d}}{\mathrm{d}t} \frac{\partial(\mathcal{L} + \mathcal{W}_e)}{\partial \dot{p}_i} - \frac{\partial(\mathcal{L} + \mathcal{W}_e)}{\partial p_i} + \frac{\partial \mathcal{D}}{\partial \dot{p}_i} = 0. \tag{3.32}$$

The LAGRANGEian $\mathcal{L} = \mathcal{T} - \mathcal{U}$ contains the kinetic and potential energy of the beam (b), spring (s) and the piezoelectric elements (p)

$$\mathcal{T} = \mathcal{T}_b + \mathcal{T}_p, \tag{3.33}$$

$$\mathcal{U} = \mathcal{U}_b + \mathcal{U}_s + \mathcal{U}_p. \tag{3.34}$$

The terms $\mathcal{U}_b$ and $\mathcal{U}_s$ are defined by Eqns. (3.11 and 3.12) and the kinetic energy of the beam is given by Eqn. (3.8).

At this point, the additional energy terms of the piezoelectric element ($\mathcal{W}_e, \mathcal{T}_p$ and $\mathcal{U}_p$) will be determined. This will be done by starting with the piezoelectric constitutive equations [4]

$$\begin{bmatrix} T_{ij} \\ D_i \end{bmatrix} = \begin{bmatrix} c^E_{ijkl} & -e_{kij} \\ e_{ikl} & \varepsilon^S_{ik} \end{bmatrix} \begin{bmatrix} S_{kl} \\ E_k \end{bmatrix}. \tag{3.35}$$

Within this equation T_{ij} is the stress tensor, D_i the electric displacement vector, c^E_{ijkl} the elastic stiffness constant tensor, e_{ikl} the piezoelectric constant tensor and ε^S_{ik} the dielectric constant tensor measured at constant strain.

Plane stress is assumed, thus all stresses T_{ij} and strains S_{ij} vanish exept for T_{11} and S_{11} respectively. Hence Eqn. (3.35) is simplified to

$$\begin{bmatrix} T_1 \\ D_3 \end{bmatrix} = \begin{bmatrix} c^E_{11} & -e_{31} \\ e_{31} & \varepsilon^S_{33} \end{bmatrix} \begin{bmatrix} S_1 \\ E_3 \end{bmatrix}, \tag{3.36}$$

where the VOIGT notation is applied. If only the d_{31}-effect is considered, the dielectric constant ε^S_{33} at constant strain is related to ε^T_{33} (constant stress) by

$$\varepsilon^S_{33} = \varepsilon^T_{33} - d^2_{31} c^E_{11}. \tag{3.37}$$

Equation (3.36) can be rewritten for clearer representation

$$\begin{bmatrix} \sigma_{11} \\ D_3 \end{bmatrix} = \begin{bmatrix} E_p & -e_{31} \\ e_{31} & \varepsilon^S_{33} \end{bmatrix} \begin{bmatrix} \varepsilon_{11} \\ E_3 \end{bmatrix}. \tag{3.38}$$

With these equations the energy expressions can be written as

$$\mathcal{U}_p = \frac{1}{2} \int_V \sigma_{11} \varepsilon_{11} \mathrm{d}V, \tag{3.39a}$$

$$\mathcal{W}_e = \frac{1}{2} \int_V E_3 D_3 \, \mathrm{d}V. \tag{3.39b}$$

Inserting Eqn. (3.38) into the energy expressions (3.39) yields

$$\mathcal{U}_p = \frac{1}{2}\int_V \varepsilon_{11}(x,z,t)(E_p\varepsilon_{11}(x,z,t) - e_{31}E_3)\,\mathrm{d}V, \tag{3.40a}$$

$$\mathcal{W}_e = \frac{1}{2}\int_V E_3\left(\varepsilon_{11}(x,z,t)e_{31} + \varepsilon_{33}^S E_3\right)\mathrm{d}V. \tag{3.40b}$$

The term $\mathcal{W}_e$ is the work of the external electrical forces. The integral over the volume V needs to be evaluated for each piezoelectric element separately. Note that the strain is a function in time and space as derived in Sec. 3.1.2. Therefore, the only unknown is the electrical field E_3. The electrical field is a quadratic function in the thickness direction of the piezoelectric patch. If the thickness of the piezopatch is smaller than the thickness of the substrate, it can be assumed that the distribution is linear. This was analyzed by Marinkovic, Koppe and Gabbert [87]. Therefore, it is assumed that

$$E_3 = \frac{v_i(t)}{h_p} \tag{3.41}$$

for each piezoelectric element. Since the patches are arranged symmetrically, the electrical field is the same for both elements. The contribution of each piezoelectric element on the kinetic energy is given by

$$\mathcal{T}_p = \frac{1}{2}\rho_p t_p b_p \int_{l_1}^{l_2} \left(\dot{w}(x,t) + \dot{e}(t)\right)^2 \mathrm{d}x. \tag{3.42}$$

The parameter ρ_p is hereby the density of a piezoelectric element. Although the kinetic energy of the piezoelectric element is derived here, it can often be neglected due to its low contribution to the modal mass.

Finally, the potential and kinetic energy expressions contained in the Lagrangeian $\mathcal{L}$ of the electromechanical beam can be stated using the relation for the nonlinear strain (Eqn. 3.5) and the energy expressions derived in

Section 3.1 The potential energy is given by

$$\begin{aligned}\mathcal{U} &= \mathcal{U}_b + \mathcal{U}_s + \mathcal{U}_p \\ &= \frac{1}{2} EI \int_0^l \frac{w_{,xx}^2(x,t)}{1 - w_{,x}(x,t)^2}\, \mathrm{d}x \\ &\quad + \frac{1}{2} k \left(\sqrt{w^2(l,t) + \left(\int_0^l u_{,x}(x,t)\, dx + l \right)} - l + l_0 \right)^2 \\ &\quad + \frac{1}{2} \int_V z \frac{w_{,xx}(x,t)}{\sqrt{1 - w_{,x}(x,t)^2}} \left(2E_p z \frac{w_{,xx}(x,t)}{\sqrt{1 - w_{,x}(x,t)^2}} + \right. \\ &\quad \left. e_{31} \frac{v_1(t) + v_2(t)}{h_p} \right) \mathrm{d}V,\end{aligned} \tag{3.43}$$

and the kinetic reads

$$\begin{aligned}\mathcal{T} &= \mathcal{T}_b + \mathcal{T}_p \\ &= \frac{1}{2} \rho_b\ h_b\ b_b \int_0^l \big(\dot{w}(x,t) + \dot{e}(t) \big)^2 \mathrm{d}x + \frac{1}{2} m \big(\dot{w}(l,t) + \dot{e}(t) \big)^2 \\ &\quad + \rho_p t_p b_p \int_{l_1}^{l_2} \big(\dot{w}(x,t) + \dot{e}(t) \big)^2 \mathrm{d}x.\end{aligned} \tag{3.44}$$

With $\mathcal{T}_b$,$\mathcal{U}_b$ and $\mathcal{U}_s$ being the kinetic and potential energy of the mechanical structure as defined in Eqns. (3.8, 3.10 and 3.12).

Dissipation function

Considering Eqn. (3.32), only the dissipation function is still unknown. The dissipation within the electromechanical system is introduced by the mechanical and the electrical part. Thus, the dissipation function is defined by

$$\mathcal{D} = \mathcal{D}_s + \mathcal{D}_p. \tag{3.45}$$

The contribution of the structure on the dissipation was already defined by the Rayleigh dissipation function $\mathcal{D}_s$ (Eqn. 3.14). The electrical circuit attached to each piezoelectric element introduces electrical dissipation to the system.

Thus, the electrical dissipation function is defined by

$$\mathcal{D}_p = \frac{1}{2R} \int v_i^2(t) \mathrm{d}t, \qquad i = 1, 2. \tag{3.46}$$

Equations of motion

Inserting Eqns. (3.43, 3.44 and 3.46) into Eqn. (3.32) by expanding $w(x,t)$ according to Eqn. (3.17) results in the electromechanically coupled equations

$$\bar{m}\, \ddot{p}(t) + \lambda\, (v_1(t) + v_2(t)) + \alpha\, p(t) + \beta\, p^3(t) + \bar{\mu}\, \dot{p}(t) = \bar{m}_e\, \ddot{e}(t), \tag{3.47a}$$

$$C_p \dot{v}_1(t) + \phi\, v_1(t) = \lambda\, \dot{p}(t), \tag{3.47b}$$

$$C_p \dot{v}_2(t) + \phi\, v_2(t) = \lambda\, \dot{p}(t). \tag{3.47c}$$

The parameters contained within these equations are given in Appendix A.1. In the following the bistable case will be considered. Thus, the minimal required prestress load can be defined by considering the definition of α (A.1e). This yields in

$$kl_0 \geq \frac{\pi^2 EI}{l^2} + \frac{\pi E_p b_p h_p \left(6h_b h_p + 3h_b^2 + 4h_p^2\right)}{12 l^3} \tag{3.48}$$

$$\left(2\pi\,(l_2 - l_1) - l\left(\sin\frac{2\pi l_2}{l} - \sin\frac{2\pi l_1}{l}\right)\right). \tag{3.49}$$

It is convenient to connect the attached piezoelectric elements in series or parallel. This can be done in an optimal way if the generated voltages $v_i(t)$ are identical. This is the case for the considered electromechanical beam due to the symmetric bonded piezoelectric patches. Therefore, both electrical circuits are connected in series by assuming

$$v_s(t) = v_1(t) + v_2(t) \tag{3.50}$$

which results in the equation

$$\kappa\, \dot{p}(t) + \frac{1}{2} C_p\, \dot{v}_s(t) = \frac{1}{2} \phi\, v_s(t) \tag{3.51}$$

for the electrical circuit.

3.2.3. Nondimensionalization and parameter reduction

For the analysis of the electromechanical equations it is convenient to perform an nondimensionalization and parameter reduction. Equations (3.47a and 3.51) can be rearranged to give

$$m\ \ddot{p}(t) + \mu\ \dot{p}(t) - \kappa\ v(t) - \alpha\ p(t) + \beta\ p^3(t) = \hat{e}\ \ddot{e}(t) \tag{3.52a}$$

$$\phi\ v(t) + \kappa\ \dot{p}(t) + \gamma\ \dot{v}(t) = 0, \tag{3.52b}$$

with

$$\mu, \alpha, \beta, \kappa, \phi, \gamma > 0$$

for the bistable domain. Equation (3.52) can also be written in the form

$$\ddot{p}(t) + \bar{\mu}\ \dot{p}(t) - \delta\ v(t) - \bar{\alpha}\ p(t) + \bar{\beta}\ p^3(t) = \hat{\bar{e}}\ \ddot{e}(t), \tag{3.53a}$$

$$\bar{\phi}\ v(t) + \eta\ \dot{p}(t) + \dot{v}(t) = 0. \tag{3.53b}$$

This formulation is convenient especially for analytical investigations, though the overbars can be dropped as long as clearness is ensured. The coupled equations (3.52) can be nondimensionalized in order to reduce the number of parameters within the system. The number of independent parameters is three. The transformation is given by

$$p(t) = \sqrt{\frac{\alpha}{\beta}}\ q(\tau), \qquad t = \tau\sqrt{\frac{m}{\alpha}}, \qquad v(t) = \frac{\alpha}{\sqrt{\beta\ \gamma}} V(\tau). \tag{3.54}$$

The resulting equations read

$$\ddot{q}(\tau) + \bar{\mu}\,\dot{q}(\tau) - \bar{\kappa}\,V(\tau) - q(\tau) + q^3(\tau) = \hat{\bar{f}}\ \ddot{f}(\tau). \tag{3.55a}$$

$$\dot{V}(\tau) + \bar{\phi}\,V(\tau) + \bar{\kappa}\,\dot{q}(\tau) = 0, \tag{3.55b}$$

with

$$\bar{\kappa} = \frac{\kappa}{\sqrt{\gamma\alpha}}, \qquad \bar{\phi} = \sqrt{\frac{m}{\alpha}}\frac{\phi}{\gamma}, \qquad \bar{\mu} = \sqrt{\frac{1}{\alpha\ m}}\mu. \tag{3.56}$$

These three parameters describe the whole parameter space of the coupled equations. The parameter $\bar{\mu}$ is the mechanical damping, $\bar{\kappa}$ the coupling coefficient and $\bar{\phi}$ the electrical conductance of the electrical circuit. To simplify the equations, the overbars can be omitted as long as clearness is preserved.

For better representation of the normalized equations, it is advantageous to transform the Eqn. (3.52) by the mechanical eigenfrequency about a stable equilibrium. This can be done with the following substitutions

$$p(t) = \frac{1}{2}\sqrt{\frac{\alpha}{\beta}}\, q(\tau), \qquad t = \tau\sqrt{\frac{m}{2\alpha}}, \qquad v(t) = \frac{\alpha}{\sqrt{\beta\,\gamma}} V(\tau). \tag{3.57}$$

In this case the equations read

$$\ddot{q}(\tau) + \frac{\bar{\mu}}{\sqrt{2}}\dot{q}(\tau) - \bar{V}(\tau) - \frac{1}{2}q(\tau) + \frac{1}{8}q^3(\tau) = \hat{\bar{f}}\,\ddot{\bar{f}}(\tau) \tag{3.58a}$$

$$\sqrt{2}\dot{V}(\tau) + \bar{\phi}V(\tau) + \frac{\bar{\kappa}}{\sqrt{2}}\dot{q}(\tau) = 0, \tag{3.58b}$$

with the coefficients given by Eqn. (3.56). This has the advantage that resonance occurs for the excitation frequency $\bar{\Omega}$=0.

3.3. Composite plate

3.3.1. Modelling

In the following section the equations of motion of a bistable composite plate are derived. Bistable composite laminates result from an asymmetric lay-up of the laminate plies. Asymmetric laminates can exhibit bistable characteristics due to the orthotropic thermal expansions of the plies. Hyer [63] showed that these differences introduce residual stresses which lead to an out-of-plane deformation [26,62] of the plate that is dependent on the temperature difference between curing and service temperature. Therefore, the bistable behavior is based on structural properties. Bistable laminates have been known for a considerable time. In the last years, they have attracted several researchers in the field of smart materials and structures. Due to the different shape modes, these laminates can be exploited for morphing, e.g. adaptive airfoils.

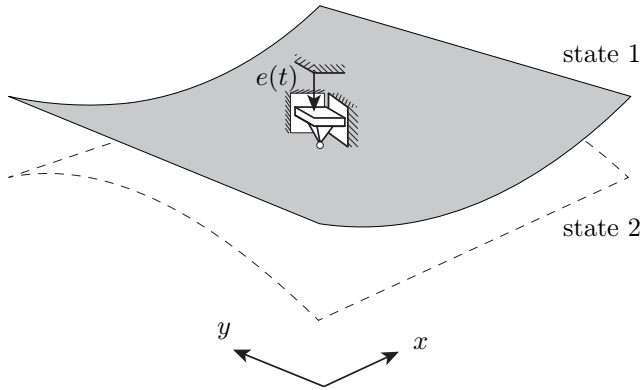

Figure 3.4: Bistable composite plate

Figure 3.4 shows a simple bistable composite plate which is clamped at the center. Both orthogonal stable states can be identified. The laminate is excited by the base-excitation $e(t)$. The geometric and material parameters will be introduced later.

For the modelling, the classical laminate theory needs to be applied [42,68], although nonlinear kinematic relations will be considered. The equations of motion will be derived by LAGRANGE's equation (Eqn. 3.7). Thus, the kinetic energy $\mathcal{T}$ and potential energy $\mathcal{U}$ need to be determined. For doing so, an assumption for the stress field will be made in order to avoid coupled equations in the in-plane and out-of-plane deformation. A derivation of the equations of motion considering the coupled in-plane and out-of-plane deformation is found the literature [67, 84]. The derivation of an reduced model, containing only the out-of-plane deformation by making an assumption for the in-plane deformation is also found in the literature [18, 19, 30], however partly inaccurate. Thus, it seems to be necessary to describe the derivation in detail.

3.3.2. Derivation of the equations of motion

Figure 3.5 shows the geometry of the considered composite plate. The laminate is composed of two plies of the same lamina. The lamina is characterized

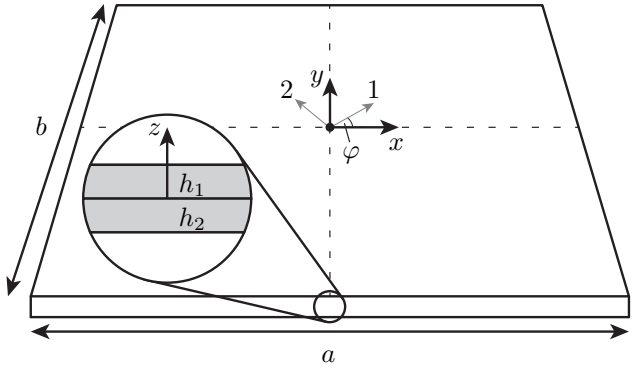

Figure 3.5: Geometry of the composite plate

by the elastic constants $E_1, E_2, \nu_{12}, \nu_{21}$ and G_{12}, as well as the thermal expansion coefficients α_1, α_2 and the mass density ρ. The dimensions of the composite plate are given by the parameters a and b, whereby, the thickness of each ply is given by $h_1 = h_2 = \frac{h}{2}$. The lay-up configuration is $[90, 0]$ which means that the plies are orientated rectangularly to each other. Each plies' orientation is described by means of the local 1/2- coordinate system. The global coordinates are given by x and y. The asymmetric lay-up leads to a bistable behavior for a sufficient large temperature difference ΔT between curing and operation temperature. The composite plate is excited by a base-excitation described by the function $e(t)$ at the point of origin. The equations of motion describing the out-of-plane dynamics will be derived by the LAGRANGE's equations. Thus, the LAGRANGEian

$$\mathcal{L} = \mathcal{T} - \mathcal{U} \tag{3.59}$$

needs to be defined. The kinetic energy $\mathcal{T}$ and potential energy $\mathcal{U}$ will be derived in the following sections.

Energy expressions

The energy expressions for each lamina read [30, 42, 68]

$$\mathcal{T} = \frac{1}{2}\rho \int_V \left(\dot{w}(x,y,t) + \dot{e}(t)\right)^2 \mathrm{d}V + \int_V \frac{1}{2} z^2 \left(\dot{w}_{,y}^2(x,y,t) + \dot{w}_{,x}^2(x,y,t)\right) \mathrm{d}V, \tag{3.60a}$$

$$\mathcal{U} = \int_V \Pi \, \mathrm{d}V. \tag{3.60b}$$

The first term of the kinetic energy accounts for the deflection of the laminate, and the second one for the rotation. Note that the in-plane dynamics is neglected. The specific potential energy Π is defined by [68, 102]

$$\Pi = \frac{1}{2}\boldsymbol{\varepsilon}\bar{\mathbf{Q}}\boldsymbol{\varepsilon} - \boldsymbol{\varepsilon}\bar{\mathbf{Q}}\bar{\boldsymbol{\alpha}}\Delta T. \tag{3.61}$$

The first term term describes the elastic energy due to the mechanical stress. The second term accounts for the residual stresses introduced by the temperature difference ΔT. The overbar indicates that the matrices or vectors are described in the global x/y- coordinate system. The transformation from the local $1/2$-coordinate system of each ply to the global coordinate system can be done by applying the rotation matrix

$$\mathbf{T} = \begin{bmatrix} \cos^2\varphi & \sin^2\varphi & 2\cos\varphi\sin\varphi \\ \sin^2\varphi & \cos^2\varphi & -2\cos\varphi\sin\varphi \\ -\cos\varphi\sin\varphi & \cos\varphi\sin\varphi & \cos^2\varphi - \sin^2\varphi \end{bmatrix} \tag{3.62}$$

to obtain the global stiffness matrix and the thermal expansion vector

$$\bar{\mathbf{Q}} = \mathbf{T}^{-1}\mathbf{Q}\,\mathbf{T}^{-T}, \tag{3.63}$$

$$\bar{\boldsymbol{\alpha}} = \mathbf{T}^{-1}\boldsymbol{\alpha}. \tag{3.64}$$

The local stiffness matrix and the vector of thermal expansion are given by [42, 68]

$$\mathbf{Q} = \frac{1}{1-\nu_{12}\nu_{21}} \begin{bmatrix} E_{11} & E_{22}\nu_{12} & 0 \\ E_{22}\nu_{12} & E_{22} & 0 \\ 0 & 0 & G_{12}(1-\nu_{12}\nu_{21}) \end{bmatrix}, \tag{3.65}$$

$$\boldsymbol{\alpha} = \begin{bmatrix} \alpha_1 \\ \alpha_2 \\ \alpha_3 \end{bmatrix}. \tag{3.66}$$

Kinematic relations and deformation field

Within Eqn. (3.61) only the strain field remains to be determined. This field is more involved since in-plane and out-of-plane deformations are coupled. Therefore, an approximation will be made starting with a shape *ansatz* for the out-of-plane deformations. Only the lowest modes for each degree of freedom are of interest. Thus, only the first deflection modes will be considered in the RITZ discretization. To this end, the out-of-plane deformation field $w(x, y, t)$ is expanded by the separation of the variables

$$w(x, y, t) = \sum_i W_i(x, y)\ p_i(t). \tag{3.67}$$

The first modes for the out-of-plane displacement are approximated by the function

$$w^0(x, y, t) = \left(\frac{2x}{a}\right)^2 p_1(t) + \left(\frac{2y}{b}\right)^2 p_2(t). \tag{3.68}$$

In this case, the displacement is described by polynomials of second order, which is common for asymmetric laminates [26, 62]. The two generalized coordinates $p_1(t)$ and $p_2(t)$ are introduced to describe the motion for both modes.

With the defined shape function (3.68), the kinematic relations can be stated. The VON KÁRMÁN[3] strains for the neutral plane of a thin plate are

[3] Theodore VON KÁRMÁN (1881-1963), Hungarian-American mathematician, aerospace engineer and physicist

given by [12, 116]

$$\varepsilon_x^0 = u_{,x}^0 + \frac{1}{2} {w_{,x}^0}^2, \tag{3.69a}$$

$$\varepsilon_y^0 = v_{,y}^0 + \frac{1}{2} {w_{,y}^0}^2, \tag{3.69b}$$

$$\gamma_{xy}^0 = u_{,y}^0 + v_{,x}^0 + w_{,x}^0 w_{,y}^0. \tag{3.69c}$$

The out-of-plane deformation w^0 and the in–plane deformations u^0, v^0 are yet to be determined. To this end, the mid-plane strain is approximated by the polynomials

$$\varepsilon_x^0 = e_1 + e_2 x^2 + e_3 y^2 + e_4 xy, \tag{3.70a}$$

$$\varepsilon_y^0 = e_5 + e_6 x^2 + e_7 y^2 + e_8 xy. \tag{3.70b}$$

The e_i are parameters which still need to be defined. The in-plane deformation can be obtained by rearranging and integrating the kinematic relations (3.69) relations which are given by

$$\begin{aligned} u^0 &= \int \varepsilon_x^0 - \frac{1}{2} {w_{,x}^0}^2 \mathrm{d}x \\ &= e_1 x + \frac{1}{3} e_2 x^3 + \frac{1}{2} e_4 x^2 y + e_3 x y^2 + e_9 y + \frac{1}{3} e_{10} y^3 - \frac{32 x^3}{3a^4} p_1^2(t), \end{aligned} \tag{3.71a}$$

$$\begin{aligned} v^0 &= \int \varepsilon_y^0 - \frac{1}{2} {w_{,y}^0}^2 \mathrm{d}y \\ &= +e_5 y + \frac{1}{3} e_{11} x^3 + e_6 x^2 y + \frac{1}{2} e_8 x y^2 + e_9 x + \frac{1}{3} e_7 y^3 - \frac{32 y^3}{3b^4} p_2^2(t). \end{aligned} \tag{3.71b}$$

The constants e_{9-11} result from the integration in order to obtain complete polynomials of third order for the in-plane deformation. Note that the unknowns e_i are actually functions of time. With the relations (3.71) the strain component γ_{xy}^0 is defined. The full strains of the plate are defined by [12, 125]

$$\varepsilon_x = \varepsilon_x^0 - z\kappa_x, \tag{3.72a}$$

$$\varepsilon_y = \varepsilon_y^0 - z\kappa_y, \tag{3.72b}$$

$$\gamma_{xy} = \gamma_{xy}^0 - z\kappa_{xy}, \tag{3.72c}$$

with

$$\kappa_x = w_{,xx}, \tag{3.73a}$$

$$\kappa_y = w_{,yy}, \tag{3.73b}$$

$$\kappa^0_{xy} = 2\, w_{,xy}. \tag{3.73c}$$

Kinetic energy $\mathcal{T}$

The kinetic energy $\mathcal{T}$ is defined by Eqn. 3.60a. With the definition of the shape function (Eqn. 3.68) the functional $\mathcal{T}$ reads

$$\mathcal{T} = f(\mathbf{p}). \tag{3.74}$$

Dissipation function $\mathcal{D}$

According to Kyriazoglou and Guild [77], the damping is assumed to be proportional to the mass matrix. Thus,

$$\mathcal{D} = \alpha_0 \frac{1}{2} \rho \int_V \dot{w}^{0\,2}\, \mathrm{d}V. \tag{3.75}$$

The parameter α_0, the proportionality factor, is yet to be determined. If the modal coordinates p_i are considered, the parameter α_0 is defined by [88]

$$\alpha_0 = 2 D_n \omega_n, \tag{3.76}$$

with the damping ratio D_n and the eigenfrequency ω_n.

Potential energy $\mathcal{U}$

With the kinematic relations (3.72) the potential energy $\mathcal{U}$ can be written as

$$\mathcal{U} = \int \left(\frac{1}{2} \boldsymbol{\varepsilon} \bar{\mathbf{Q}} \boldsymbol{\varepsilon} - \boldsymbol{\varepsilon} \bar{\mathbf{Q}} \bar{\boldsymbol{\alpha}} \Delta T \right) \mathrm{d}V \tag{3.77}$$

with

$$\boldsymbol{\varepsilon} = \begin{pmatrix} \varepsilon_x \\ \varepsilon_x \\ \gamma_{xy} \end{pmatrix}. \tag{3.78}$$

Thus, the functional $\mathcal{U}$ reads

$$\mathcal{U} = f\left(e_1, \cdots, e_{11}, p_i(t)\right). \tag{3.79}$$

Equations of motion

The equations of motion are obtained by the LAGRANGE's equation

$$\frac{d}{dt}\frac{\partial \mathcal{L}}{\partial \dot{q}_i} - \frac{\partial \mathcal{L}}{\partial q_i} + \frac{\partial \mathcal{D}}{\partial \dot{q}_i} = 0, \tag{3.80}$$

where the vector $\mathbf{q}$ contains the generalized coordinates p_i and the unknown parameters e_i. The functionals of the kinetic energy $\mathcal{T}$ and the dissipation function $\mathcal{D}$ are solely functions of the generalized coordinates p_i. Moreover, the coefficients e_i appear independently throughout the functional $\mathcal{U}$ (3.77). Thus, this coherence is taken into account for the determination of the unknowns e_i. From Eqn. (3.80) with (3.79) the following equations are obtained

$$\frac{\partial \mathcal{U}}{\partial e_i} = 0, \qquad i = 1, ..., 11, \tag{3.81}$$

leading to direct definitions of the coefficients in terms of the variables $p_i(t)$,

$$e_i = f(p_i(t)). \tag{3.82}$$

Inserting Eqn. (3.82) into (3.77) results in the functional of the potential energy

$$\mathcal{U} = f(\mathbf{p}), \tag{3.83}$$

where $\mathbf{p}$ is the vector of the degrees of freedom $p_i(t)$.

The equation of motion can now be derived by substituting Eqns. (3.74, 3.75 and 3.83) into Eqn. (3.7). This leads in the equation of motion for the composite plate

$$\mathbf{M}\ddot{\mathbf{p}} + \mathbf{D}\dot{\mathbf{p}} + \mathbf{K}(\mathbf{p}) = \hat{\mathbf{e}}\, e(t), \tag{3.84}$$

whereby the mass matrix and excitation vector $\hat{\mathbf{e}}$ are given by

$$\mathbf{M} = \frac{1}{9}abh\rho \begin{bmatrix} \frac{9a^2+20h^2}{5a^2} & 1 \\ 1 & \frac{9b^2+20h^2}{5b^2} \end{bmatrix}, \qquad \hat{\mathbf{e}} = \frac{1}{3}hab\rho \begin{bmatrix} 1 \\ 1 \end{bmatrix} \tag{3.85}$$

and the damping matrix by

$$\mathbf{D} = \alpha_0 \mathbf{M}. \tag{3.86}$$

Note that the nonlinear stiffness $\mathbf{K}(\mathbf{p})$ is not stated here explicitly due to its complexity. It is given in Appendix A.2.

3.3.3. Nondimensionalization and parameter reduction

In this section, a parameter reduction is performed in (3.84). For this purpose, the general form of the potential energy (Eqn. 3.83)

$$\mathcal{U} = c_1 p_1(t) + c_2 p_2(t) + \alpha_1 p_1^2(t) + \alpha_2 p_2^2(t) + \gamma p_1(t) p_2(t) + \xi p_1^2(t) p_2^2(t) \tag{3.87}$$

is considered.

With this formulation the equation of motion reads

$$\begin{aligned} &\begin{bmatrix} m_{11} & m_{12} \\ m_{12} & m_{22} \end{bmatrix} \ddot{\mathbf{p}} + \begin{bmatrix} \mu_{11} & \mu_{12} \\ \mu_{12} & \mu_{22} \end{bmatrix} \dot{\mathbf{p}} \\ &\quad + \begin{bmatrix} c_1 + 2\alpha_1 p_1(t) + \gamma p_2(t) + 2\xi p_1(t) p_2^2(t) \\ c_2 + 2\alpha_2 p_2(t) + \gamma p_1(t) + 2\xi p_1^2(t) p_2(t) \end{bmatrix} = \hat{\mathbf{e}}\ \ddot{e}(t). \end{aligned} \tag{3.88}$$

The 12 parameters on the left hand side of the equations can be reduced to 9 according to a dimension analysis. This can be achieved by transforming distance and time according to

$$\begin{aligned} p_i(t) &= q_i(\tau) \sqrt{\frac{\alpha_1}{\xi}}, \\ t &= \tau \sqrt{\frac{m_{11}}{\alpha_1}}. \end{aligned} \tag{3.89}$$

With the substitutions

$$\begin{aligned} \hat{\bar{e}}_i &= \frac{\hat{e}_i}{\alpha_1}, & \bar{c}_i &= \frac{c_i}{\alpha_1}\sqrt{\frac{\xi}{\alpha_1}}, \\ \bar{\gamma} &= \frac{\gamma}{\alpha_1}, & \bar{m}_{ij} &= \frac{m_{ij}}{m_{11}}, \\ \alpha &= \frac{\alpha_2}{\alpha_1}, & \bar{\mu}_{ij} &= \frac{\mu_{ij}}{\sqrt{\alpha_1 m_{11}}}, \end{aligned} \tag{3.90}$$

the reduced equation of motion is obtained

$$\begin{aligned} &\begin{bmatrix} 1 & \bar{m}_{12} \\ \bar{m}_{12} & \bar{m}_{22} \end{bmatrix} \ddot{\mathbf{q}} + \begin{bmatrix} \bar{\mu}_{11} & \bar{\mu}_{12} \\ \bar{\mu}_{12} & \bar{\mu}_{22} \end{bmatrix} \dot{\mathbf{q}} \\ &\quad + \begin{bmatrix} \bar{c}_1 + \bar{\gamma} q_2(\tau) + 2q_1(\tau) q_2^2(\tau) + 2q_1(\tau) \\ \bar{c}_2 + 2\alpha q_2(\tau) + \bar{\gamma} q_1(\tau) + 2q_2(\tau) q_1^2(\tau) \end{bmatrix} = \begin{bmatrix} \hat{\bar{e}}_1 \\ \hat{\bar{e}}_2 \end{bmatrix} e(\tau). \end{aligned} \tag{3.91}$$

The full (Eqn. 3.88) and the reduced equation (3.91) can be transformed to a stable equilibrium and rearranged to *normal form* to read

$$\begin{bmatrix} \ddot{p}_1 \\ \ddot{p}_2 \end{bmatrix} + \begin{bmatrix} \mu_{11} & 0 \\ 0 & \mu_{22} \end{bmatrix} \begin{bmatrix} \dot{p}_1 \\ \dot{p}_2 \end{bmatrix} + \begin{bmatrix} \alpha_{11} & \alpha_{12} \\ \alpha_{21} & \alpha_{22} \end{bmatrix} \begin{bmatrix} p_1 \\ p_2 \end{bmatrix} \tag{3.92}$$

$$+ \begin{bmatrix} \kappa_{120} p_1^2 + \kappa_{102} p_2^2 + \kappa_{111} p_1 p_2 + \beta_{112} p_1 p_2^2 + \beta_{121} p_1^2 p_2 \\ \kappa_{220} p_1^2 + \kappa_{202} p_2^2 + \kappa_{211} p_1 p_2 + \beta_{212} p_1 p_2^2 + \beta_{221} p_1^2 p_2 \end{bmatrix} = \begin{bmatrix} \hat{e}_1 \\ \hat{e}_2 \end{bmatrix} \ddot{y}. \tag{3.93}$$

3.4. Electromechanical composite plate

3.4.1. Modelling

In this section a model for a composite plate with integrated piezoelectric elements will be derived. The mechanical part of the plate is the same as in Section 3.3. Thus, this section only concerns the derivation of the additional terms, introduced by the piezoelectric elements. Two piezoelectric elements are attached to the composite plate, one on each side. Figure 3.6 only shows the piezoelectric elements on the upper side. The piezoelectric elements are equal in size (width Δx_p and length Δy_p with height h_p) and symmetrically

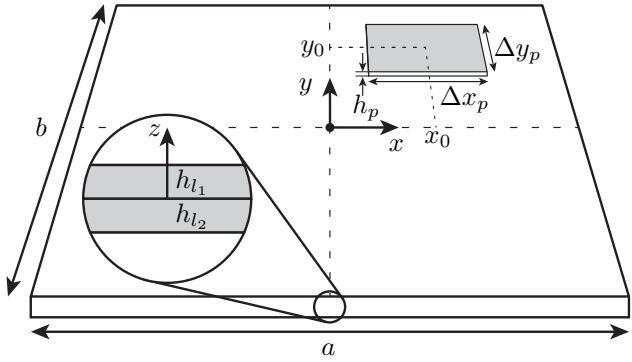

Figure 3.6: Geometry of the electromechanical composite plate

positioned on both sides. The positioning is described in terms of x_0 and y_0. The voltage $v_i(t)$ generated by each piezoelectric element is measured over the electrical resistance R.

3.4.2. Derivation of the equations of motion

The equations will be derived using the extended HAMILTONs principle which results in the LAGRANGE equation (3.32). For the derivation of the electromechanical equations the piezoelectric constitutive equations are reduced to a planar stress state. Related works, while for other mechanical structures can be found in the literature [6, 36].

Piezoelectric constitutive equations

The additional terms in the equation follow from the piezoelectric constitutive equations. The piezoelectric material is described by the linear constitutive equations [4]

$$\begin{bmatrix} S_{ij} \\ D_i \end{bmatrix} = \begin{bmatrix} s^E_{ijkl} & d_{kij} \\ d_{ikl} & \varepsilon^T_{ik} \end{bmatrix} \begin{bmatrix} T_{kl} \\ E_k \end{bmatrix} \tag{3.94}$$

or in another representation

$$\begin{bmatrix} T_{ij} \\ D_i \end{bmatrix} = \begin{bmatrix} c^E_{ijkl} & -e_{kij} \\ e_{ikl} & \varepsilon^S_{ik} \end{bmatrix} \begin{bmatrix} S_{kl} \\ E_k \end{bmatrix}. \tag{3.95}$$

For the composite plate a state of plane stress (KIRCHHOFF-LOVE plate theory) is assumed. Thus, the reduction of Eqn. (3.95) reads

$$\begin{bmatrix} T_1 \\ T_2 \\ T_6 \\ D_3 \end{bmatrix} = \begin{bmatrix} c_{11}^E & c_{12}^E & 0 & -e_{31} \\ c_{21}^E & c_{22}^E & 0 & -e_{32} \\ 0 & 0 & c_{66}^E & 0 \\ e_{31} & e_{32} & 0 & \varepsilon_{33}^S \end{bmatrix} \begin{bmatrix} S_1 \\ S_2 \\ S_6 \\ E_3 \end{bmatrix}, \tag{3.96}$$

where the VOIGT notation ($11 \rightarrow 1, 2 \rightarrow 2, 12 \rightarrow 6, 21 \rightarrow 6$) for the indices is applied. The material properties are equal in the 2nd and 3rd direction. Therefore,

$$c_{21}^E = c_{12}^E, \qquad e_{32} = e_{31}, \qquad c_{22}^E = c_{11}^E, \tag{3.97}$$

with the relations

$$\begin{aligned} c_{11}^E &= \frac{s_{11}^E}{{s_{12}^E}^2 - s_{11}^E s_{22}^E}, & c_{12}^E &= \frac{s_{12}^E}{{s_{12}^E}^2 - {s_{11}^E}^2}, \\ c_{66}^E &= \frac{1}{s_{66}^E}, & e_{31} &= \frac{d_{31}}{s_{11}^E + s_{12}^E}, \\ \varepsilon_{33}^S &= \varepsilon_{33}^T - \frac{2d_{31}^2}{s_{11}^E - s_{12}^E}. \end{aligned} \tag{3.98}$$

For the derivation of the equations of motion, the additional energy terms of the electromechanical composite plate are defined. The procedure is similar to the one in Section 3.2.

Kinetic energy

The kinetic energy of the piezoelectric element is defined by

$$\mathcal{T}_p = \frac{1}{2}\rho_p \int_{V_p} \left(\left(\dot{w}^0 + \dot{e}(t) \right)^2 + \frac{1}{2} z^2 \left(\dot{w}_{,x}^2 + \dot{w}_{,y}^2 \right) \right) \mathrm{d}V_p, \tag{3.99}$$

with the out-of-plane deformation $w^0(x, y, t)$ given by Eqn. (3.68).

Dissipation function

The voltage $v_i(t)$ of each piezoelectric element is dissipated over a resistance R. Thus, the dissipation function for the electrical circuit reads

$$\mathcal{D}_p = \frac{1}{2R}\int v_i^2(t)\mathrm{d}t, \qquad i = 1, 2. \tag{3.100}$$

With this expression, the overall dissipation of the electromechanical composite plate is given by

$$\mathcal{D} = \mathcal{D}_s + \mathcal{D}_p, \tag{3.101}$$

where the dissipation function of the structure $\mathcal{D}_s$ is given by Eqn. (3.75).

Potential energy and work of external forces

The additional energy terms for the piezoelectric element are defined by

$$\mathcal{U}_p = \frac{1}{2}\int_{V_p} T_i S_i \mathrm{d}V_p, \tag{3.102a}$$

$$\mathcal{W}_e = \frac{1}{2}\int_{V_p} E_i D_i \mathrm{d}V_p, \tag{3.102b}$$

The expressions can be expanded to read

$$\begin{aligned}\mathcal{U}_p &= \frac{1}{2}\int_{V_p}\Big(T_1S_1 + T_2S_2 + T_6S_6\Big)\mathrm{d}V_p \\ &= \frac{1}{2}\int_{V_p}\Big(\varepsilon_x\left(c_{11}^E\varepsilon_x + c_{12}^E\varepsilon_y - E_3e_{31}\right) + \varepsilon_y\left(c_{11}^E\varepsilon_y + c_{12}^E\varepsilon_x - E_3e_{31}\right) + \\ &\qquad c_{66}^E\gamma_{xy}^2\Big)\mathrm{d}V_p\end{aligned} \tag{3.103}$$

and

$$\begin{aligned}\mathcal{W}_e =& \frac{1}{2}\int_{V_p} E_3D_3\mathrm{d}V_p \\ =& \frac{1}{2}\int_{V_p} E_3\left(E_3\varepsilon_{33}^S + e_{31}(\varepsilon_x+\varepsilon_y)\right)\mathrm{d}V_p,\end{aligned} \tag{3.104}$$

with the strains ϵ_x, ϵ_y and γ_{xy} given by Eqn. (3.72). Similar to the derivation of the composite plate (Section 3.3), the unknowns e_i occur independently in the functionals $\mathcal{U}_p$ and $\mathcal{W}_e$. Thus, the LAGRANGE's equation yields in the following conditions

$$\frac{\partial(\mathcal{U}_s + \mathcal{U}_p - \mathcal{W}_e)}{\partial e_i} = 0, \qquad \text{with} \qquad i = 1, ..., 11, \tag{3.105}$$

where the potential energy of the structure $\mathcal{U}_s$ is given by Eqn. (3.60b). The solution of Eqn. (3.105) can be substituted into Eqns. (3.60b, 3.103 and 3.104) to obtain the functionals

$$\mathcal{U}_s, \mathcal{U}_p, \mathcal{W}_e = f(\mathbf{p}). \tag{3.106}$$

Having the functions which are only dependent on the variables p_i, the equations of motion can be derived using the extended LAGRANGE equations (3.32), where

$$\mathcal{U} = \mathcal{U}_s + U_p, \tag{3.107a}$$
$$\mathcal{T} = \mathcal{T}_s + T_p, \tag{3.107b}$$

with T_s defined by Eqn. (3.60a).

Finally, when Eqns. (3.104), (3.107) and (3.101) are substituted into Eqn. (3.32), the equations of motion are obtained as

$$\mathbf{M}\ddot{\mathbf{p}} + \mathbf{D}\dot{\mathbf{p}} + \mathbf{K}(\mathbf{p}) = \hat{\mathbf{e}}\, e(t). \tag{3.108}$$

3.4.3. Nondimensionalization and parameter reduction

Equation (3.108) can be expanded to read

$$\begin{bmatrix} m_{11} & m_{12} & 0 & 0 \\ m_{12} & m_{22} & 0 & 0 \\ 0 & 0 & 0 & 0 \\ 0 & 0 & 0 & 0 \end{bmatrix} \ddot{\mathbf{p}} + \begin{bmatrix} \mu_{11} & \mu_{12} & 0 & 0 \\ \mu_{12} & \mu_{22} & 0 & 0 \\ \kappa_1 & \kappa_2 & \gamma_1 & \gamma_2 \\ \kappa_2 & \kappa_1 & \gamma_2 & \gamma_1 \end{bmatrix} \dot{\mathbf{p}} + \begin{bmatrix} 2\alpha_1 & \gamma & -\kappa_1 & -\kappa_2 \\ \gamma & 2\alpha_2 & -\kappa_2 & -\kappa_1 \\ 0 & 0 & \phi_1 & 0 \\ 0 & 0 & 0 & \phi_2 \end{bmatrix} \mathbf{p} + \begin{bmatrix} c_1 + 2\xi\, p_1(t) p_2^2(t) \\ c_2 + 2\xi\, p_1^2(t) p_2(t) \\ 0 \\ 0 \end{bmatrix} = \begin{bmatrix} \hat{e}_1 \\ \hat{e}_2 \\ 0 \\ 0 \end{bmatrix} \ddot{e}(t), \tag{3.109}$$

with

$$\mathbf{p} = \begin{bmatrix} p_1 \\ p_2 \\ v_1 \\ v_2 \end{bmatrix}. \tag{3.110}$$

This equation can be reduced when both piezoelectric elements are linked. For an optimal performance it might be advantageous to keep both electrical circuits separately, but due to the symmetric attachment of the present case and the equal piezoelectric elements, both patches can be linked without loosing performance. For the considered electromechanical composite, the piezoelectric patches are connected in series ($v_1 + v_2 = v$). In this case Eqn. (3.88) is reduced to

$$\begin{bmatrix} m_{11} & m_{12} & 0 \\ m_{12} & m_{22} & 0 \\ 0 & 0 & 0 \end{bmatrix} \ddot{\mathbf{p}} + \begin{bmatrix} \mu_{11} & \mu_{12} & 0 \\ \mu_{12} & \mu_{22} & 0 \\ \kappa & \kappa & \gamma \end{bmatrix} \dot{\mathbf{p}} + \begin{bmatrix} 2\alpha_1 & \gamma & -\kappa \\ \gamma & 2\alpha_2 & -\kappa \\ 0 & 0 & \phi \end{bmatrix} \mathbf{p} + \begin{bmatrix} c_1 + 2\xi\ p_1 p_2^2 \\ c_2 + 2\xi\ p_1^2 p_2 \\ 0 \end{bmatrix} = \begin{bmatrix} \hat{e}_1 \\ \hat{e}_2 \\ 0 \end{bmatrix} \ddot{e}(t), \tag{3.111}$$

with

$$\begin{aligned}\phi &= \frac{1}{2}\left(\phi_1 + \phi_2\right),\\ \kappa &= \frac{1}{2}\left(\kappa_1 + \kappa_2\right),\\ \gamma &= \frac{1}{2}\left(\gamma_1 + \gamma_2\right),\end{aligned} \tag{3.112}$$

and

$$\mathbf{p} = \begin{bmatrix} p_1 \\ p_2 \\ v \end{bmatrix}. \tag{3.113}$$

A dimension analysis shows that the 14 parameters on the left side of Eqn. (3.111) can be reduced to a number of 11. This results in the equation

$$\begin{aligned}&\begin{bmatrix} 1 & \bar{m}_{12} & 0 \\ \bar{m}_{12} & \bar{m}_{22} & 0 \\ 0 & 0 & 0 \end{bmatrix} \ddot{\mathbf{q}} + \begin{bmatrix} \bar{\mu}_{11} & \bar{\mu}_{12} & 0 \\ \bar{\mu}_{12} & \bar{\mu}_{22} & 0 \\ \bar{\kappa} & \bar{\kappa} & 1 \end{bmatrix} \dot{\mathbf{q}}\\ &\quad + \begin{bmatrix} 2 & \bar{\gamma} & -\bar{\kappa} \\ \bar{\gamma} & 2\alpha & -\bar{\kappa} \\ 0 & 0 & \bar{\phi} \end{bmatrix} \mathbf{q} + \begin{bmatrix} \bar{c}_1 + 2\,q_1 q_2^2 \\ \bar{c}_2 + 2\,q_1^2 q_2 \\ 0 \end{bmatrix} = \begin{bmatrix} \hat{g}_1 \\ \hat{g}_2 \\ 0 \end{bmatrix} \ddot{e}(\tau),\end{aligned} \tag{3.114}$$

by applying the transformations (3.89 and 3.90) such as

$$\begin{aligned}\bar{\kappa} &= \frac{\kappa}{\sqrt{\alpha_1 \delta}}, & \bar{\phi} &= \frac{\phi\sqrt{m_{11}}}{\delta\sqrt{\alpha_1}},\\ v(t) &= V(\tau)\frac{\alpha_1}{\sqrt{\xi\delta}}.\end{aligned} \tag{3.115}$$

The vector $\mathbf{q}$ reads

$$\mathbf{q} = \begin{bmatrix} q_1 \\ q_2 \\ v \end{bmatrix}. \tag{3.116}$$

3.5. Multistable plate

In this section the equations of motion of a multistable plate are derived. This structure allows to have more than two equilibria. The structures in the previous sections exhibit two stable equilibria. The considered multistable plate permits to investigate the effect of multistability and multiple eigenfrequencies. The motivation for the considered structure is initially of theoretical nature. A feasible design would most likely introduce the prestress in a different way.

3.5.1. Modelling

Figure 3.7 shows a prestressed plate as a simple multistable structure. The isotropic material is described in terms of YOUNG's modulus E, POISSON's ratio ν and the mass density ρ. The dimensions of the plate are defined by the height h and the side length a and b. The plate is prestressed by two discrete springs acting on the midplane. For the application the prestress can also be realized by magnets or a pre-deformation. The springs are characterized by the stiffness parameters k_x and k_y with the corresponding pre-deformation Δl_x and Δl_y. The plate is mounted to an excited base. The excitation is described by the function $e(t)$.

The model of the multistable plate can be derived in a similar way to the composite plate.

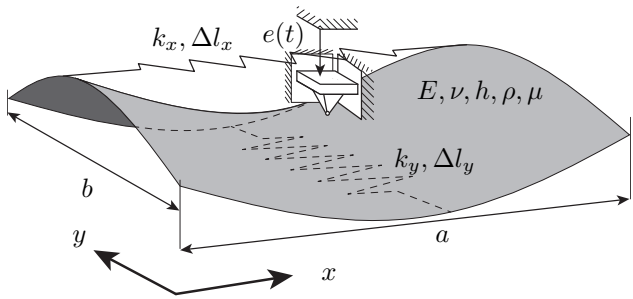

Figure 3.7: Geometry of a prestressed plate

3.5.2. Derivation of the equations of motion

Kinematic relations

For the considered plate a two-dimensional stress state can be assumed. This leads to

$$\sigma_{zz} = 0 \tag{3.117a}$$

$$\tau_{yz} = \tau_{zy} = 0 \tag{3.117b}$$

$$\tau_{xz} = \tau_{zx} = 0. \tag{3.117c}$$

Similar to the composite plate, an assumption for the deformation field is made. With a simple polynomial *ansatz*, the mid-plane stress can be written according to Eqn. (3.70), where the same shape function is used (Eqn. 3.68). With the expression for the mid-plate strain, the strain can be written as

$$\varepsilon_x = \varepsilon_x^0 - z\kappa_x, \tag{3.118a}$$

$$\varepsilon_y = \varepsilon_y^0 - z\kappa_y, \tag{3.118b}$$

$$\gamma_{xy} = \gamma_{xy}^0 - z\kappa_{xy}. \tag{3.118c}$$

where κ_x, κ_y and κ_{xy} denote the curvatures. The curvatures are defined by

$$\kappa_x = w_{,xx}, \tag{3.119a}$$

$$\kappa_y = w_{,yy}, \tag{3.119b}$$

$$\kappa_{xy}^0 = 2w_{,xy}. \tag{3.119c}$$

Note that it is enough to consider the linearized kinematic relations. The nonlinearity is introduced by the coupling of in-plane and out-of-plane deformation. The constitutive equations are given by

$$\sigma_{xx} = \frac{E}{1-\nu^2}(\varepsilon_{xx} + \nu\varepsilon_{yy}), \tag{3.120a}$$

$$\sigma_{yy} = \frac{E}{1-\nu^2}(\varepsilon_{yy} + \nu\varepsilon_{xx}), \tag{3.120b}$$

$$\tau_{xy} = \frac{E}{2(1+\nu)}\varepsilon_{xy}. \tag{3.120c}$$

Energy expressions

With Eqns. (3.118 and 3.120) the strain energy density can be formulated

$$\Pi = \frac{1}{2}\sigma_{xx}\varepsilon_{xx} + \sigma_{yy}\varepsilon_{yy} + \tau_{xy}\gamma_{xy}. \tag{3.121}$$

The potential energy of the springs is given by

$$\begin{aligned}\mathcal{U}_s = &\frac{1}{2}\left(\Delta l_x + u^0\big|_{x=a/2,y=0} - u^0\big|_{x=-a/2,y=0}\right)^2 k_x + \\ &\frac{1}{2}\left(\Delta l_y + v^0\big|_{x=0,y=-b/2} - v^0\big|_{x=0,y=b/2}\right)^2 k_y,\end{aligned} \tag{3.122}$$

with the in-plane deformations that are given by Eqn. (3.71). Thus, the potential energy of the bistable plate reads

$$\mathcal{U} = \int_{-\frac{h}{2}}^{\frac{h}{2}} \int_{-a/2}^{a/2} \int_{-b/2}^{b/2} \Pi \,\mathrm{d}x\,\mathrm{d}y\,\mathrm{d}z + \mathcal{U}_s. \tag{3.123}$$

The kinetic energy of the plate is defined by

$$\mathcal{T} = \frac{1}{2}\rho \int \left(\left(\dot{w}(x,y,t) + \dot{y}(t)\right)^2 + \frac{1}{2} z^2 \left(\dot{w}_{,x}^2 + \dot{w}_{,y}^2\right) \right) \mathrm{d}V. \tag{3.124}$$

With the formulation of the potential and kinetic energy, the LAGRANGEian is defined by

$$\mathcal{L} = \mathcal{T} - \mathcal{U}. \tag{3.125}$$

At this point, the functional $\mathcal{L}$ is a function of the unknowns e_i and the degrees-of-freedom $p_i(t)$

$$\mathcal{U} = f\left(e_1 \cdots e_{11}, p_i(t)\right). \tag{3.126}$$

These unknowns e_i occur linearly independent from p_i, such that the functional $\mathcal{U}$ can be minimized by

$$\frac{\partial \mathcal{U}}{\partial e_i} = 0, \qquad i = 1, ..., 11 \tag{3.127}$$

Equations (3.127) can be solved for e_i and substituted into Eqn. (3.126) which leads to a functional for the potential energy

$$\mathcal{U} = f(\mathbf{p}). \tag{3.128}$$

A damping proportional to the mass-matrix will be assumed. Thus, the functional $\mathcal{D}$ is defined by

$$\mathcal{D} = \alpha_0 \frac{1}{2} \rho \int \dot{w}^2(x, y, t) \mathrm{d}V. \tag{3.129}$$

Finally, the equations of motions can directly be derived with LAGRANGE's equation which follows from HAMILTON's principle using the RITZ approach.

$$\frac{d}{dt} \frac{\partial \mathcal{L}}{\partial \dot{q}_i} - \frac{\partial \mathcal{L}}{\partial q_i} + \frac{\partial \mathcal{D}}{\partial \dot{q}_i} = 0. \tag{3.130}$$

The mass matrix $\mathbf{M}$, the damping matrix $\mathbf{D}$ and the excitation vector $\hat{\mathbf{e}}$ are the same as for the composite plate (Eqns. 3.85 and 3.86). The stiffness $\mathbf{K}(\mathbf{q})$ is given in Appendix A.4 due to its length.

3.5.3. Nondimensionalization and parameter reduction

The potential energy has the form

$$\mathcal{U} = -\alpha_1 p_1^2 - \alpha_2 p_2^2 + \beta_1 p_1^4 + \beta_2 p_2^4 + \gamma p_1 p_2 - \eta_1 p_1^3 p_2 - \eta_2 p_1 p_2^3 + \kappa p_1^2 p_2^2 \tag{3.131}$$

With this formulation the equations of motion read

$$\begin{aligned} &\begin{bmatrix} m_{11} & m_{12} \\ m_{12} & m_{22} \end{bmatrix} \ddot{\mathbf{p}} + \begin{bmatrix} \mu_{11} & \mu_{12} \\ \mu_{12} & \mu_{22} \end{bmatrix} \dot{\mathbf{p}} \\ &\quad + \begin{bmatrix} -2\alpha_1 p_1 + 4\beta_1 p_1^3 + \gamma p_2 - 3\eta_1 p_1^2 p_2 - \eta_2 p_2^3 + 2\kappa p_1 p_2^2 \\ -2\alpha_2 p_2 + 4\beta_2 p_2^3 + \gamma p_1 - \eta_1 p_1^3 - 3\eta_2 p_1 p_2^2 + 2\kappa p_1^2 p_2 \end{bmatrix} = \hat{\mathbf{e}}\ \ddot{e}(t). \end{aligned} \tag{3.132}$$

The number of parameters in this equation can be reduced by an appropriate transformation. This can be achieved by applying the transformation

$$p_i(t) = q_i(\tau) \sqrt{\frac{\alpha_1}{\beta_1}}, \tag{3.133a}$$

$$t = \tau / \sqrt{\alpha_1}, \tag{3.133b}$$

for deflection and time. Thus, the reduced equations read

$$\begin{bmatrix} 1 & \bar{m}_{12} \\ \bar{m}_{12} & \bar{m}_{22} \end{bmatrix} \ddot{\mathbf{q}} + \begin{bmatrix} \bar{\mu}_{11} & \bar{\mu}_{12} \\ \bar{\mu}_{12} & \bar{\mu}_{22} \end{bmatrix} \dot{\mathbf{q}} + \begin{bmatrix} -2q_1 + 4q_1^3 + \bar{\gamma} q_2 - 3\bar{\eta}_1 q_1^2 q_2 - \bar{\eta}_2 q_2^3 + 2\bar{\kappa} q_1 q_2^2 \\ -2\alpha q_2 + 4\beta q_2^3 + \bar{\gamma} q_1 - \bar{\eta}_1 q_1^3 - 3\bar{\eta}_2 q_1 q_2^2 + 2\bar{\kappa} q_1^2 q_2 \end{bmatrix} = \hat{\mathbf{e}}\ \ddot{e}(\tau), \tag{3.134}$$

where

$$\begin{aligned} \hat{\bar{e}}_i &= \frac{\hat{e}_i}{\alpha_1}, & \bar{\eta}_i &= \frac{\eta_i}{\beta_i}, \\ \bar{\gamma} &= \frac{\gamma}{\alpha_1}, & \bar{m}_{ij} &= \frac{m_{ij}}{m_{11}}, \\ \alpha &= \frac{\alpha_2}{\alpha_1}, & \bar{\mu}_{ij} &= \frac{\mu_{ij}}{\sqrt{\alpha_1 m_{11}}}, \\ \bar{\kappa} &= \frac{\kappa}{\beta_1}. \end{aligned} \tag{3.135}$$

4. Analytical framework

This chapter deals with the analytical framework for the investigation of nonlinear equations of motion. The aim is to briefly introduce the methods which are applied in the following chapters. Nonlinear differential equations usually do not possess a closed-form solution for free or harmonically forced systems like linear systems. To this end, various analytical approximation methods have been developed. The most significant methods will be presented. The behavior of nonlinear systems can be described in terms of bifurcation points, at which the solution changes its characteristics. Those bifurcation points can be obtained by perturbation calculus, which became famous when it was used by LE VERRIER[1] to predict the existence of the planet neptune before it had been observed [80]. Also newer methods such as normal form theory will be used [92]. All these methods are tools to describe the dynamics of nonlinear systems, but they do not give exact solutions. They rather provide insight for which parameters a specific solution may be observed and give understanding of the occurring bifurcations.

In this chapter the methods are quintessentially applied to the nondimensionalized DUFFING equation

$$\ddot{x}(t) + \mu\dot{x}(t) - \alpha x(t) + \beta x^3(t) = e(t), \tag{4.1}$$

under the following assumptions

$$\mu, \alpha, \beta \ > 0, \tag{4.2a}$$

$$e(t) = \hat{e}\sin(\Omega t). \tag{4.2b}$$

The stable equilibria of Eqn. (4.1) with $e(t) = 0$ are given by

$$x_s = \pm\sqrt{\frac{\alpha}{\beta}} \tag{4.3}$$

[1] Urbain Jean Joseph LE VERRIER (1811-1877), French mathematician

the differential equation linearized about such an equilibrium position has the eigenfrequency

$$\omega = \sqrt{2\alpha}. \tag{4.4}$$

Additionally, the extension of the presented methods to coupled equations will be shown in some cases. Introductions to the field of analytical methods in nonlinear dynamics can be found in the book by Waag and Neild [128], Hagedorn [51] or in the book by Nayfeh [95]. A geometrical study of the bistable Duffing equation can be found in the publication by Gilmore and McCallum [44].

4.1. Multiple scales method

The idea of perturbation calculus is to represent the exact solution $x(t)$ as a perturbation expansion

$$x(t) = x_0(t) + \epsilon\, x_1(t) + \epsilon^2 x_2(t) + \cdots \tag{4.5}$$

with $\epsilon \ll 1$ as the perturbation parameter. There are different methods to apply a perturbation such as Eqn. (4.5). A detailed treatment of various methods for a variety of mechanical problems can be found in the book by Nayfeh [94]. Here, the method of multiple scales will be used. This method will be presented in the following by means of the bistable Duffing equation in order to apply it to coupled systems in later sections.

The underlying idea of the multiple scales method is to represent the solution $x(t)$ as a function of independent variables that change in terms of different time scales.

$$\begin{aligned} x(t,\epsilon) = x_0(T_0, T_1, T_2, \cdots) + \epsilon\, x_1(T_0, T_1, T_2, \cdots) \\ + \epsilon^2 x_2(T_0, T_1, T_2, \cdots) + \cdots, \end{aligned} \tag{4.6}$$

where $T_n = \epsilon^n t$. On the fastest scale ($T_0 = t$) it is assumed that the solution is dominated by the free oscillation response of the linearized undamped system. Thus, the nonlinearity, damping and excitation are regarded as perturbations

of this response. To this end, the perturbation parameter ϵ is introduced such that the solution on the fastest scale x_0 does not interact with the nonlinearity, damping and excitation. With this assumption the linearized equation about a stable equilibrium reads

$$\ddot{x}(t) + \epsilon^2 \mu\, \dot{x}(t) + 2\alpha\, x(t) + \epsilon\; 3\sqrt{\alpha\beta}\, x^2(t) + \epsilon^2 \beta\, x^3(t) = \epsilon^2 \hat{e} \cos(\Omega\; t). \tag{4.7}$$

An excitation about the eigenfrequency

$$\Omega = \omega + \epsilon^2 \sigma \tag{4.8}$$

is considered. The parameter σ is a small deviation in the frequency. Inserting the expansion (4.6) into Eqn. (4.7) and equating the terms with the same order in the perturbation parameter ϵ yields in the relations

$$\epsilon^0 : D_0^2 x_0 + x_0 \omega^2 = 0, \tag{4.9a}$$

$$\epsilon^1 : D_0^2 x_1 + x_1 \omega^2 + \eta\; x_0^2 + 2 D_0 D_1 x_0 = 0, \tag{4.9b}$$

$$\begin{aligned} \epsilon^2 : D_0^2 x_2 + x_2 \omega^2 + D_0 \mu x_0 + D_1^2 x_0 + 2 D_0 D_2 x_0 + 2 D_0 D_1 x_1 - \hat{e} \cos(\Omega t) \\ + 2\eta\; x_1 x_0 + \beta x_0^3 = 0, \end{aligned} \tag{4.9c}$$

The D_i are derivatives defined by

$$D_i = \frac{\mathrm{d}}{\mathrm{d}T_i} \tag{4.10}$$

and

$$\begin{aligned} \eta &= 3\sqrt{\alpha\beta}, \\ \omega &= \sqrt{2\alpha}. \end{aligned} \tag{4.11}$$

The relations (4.9) can be solved consecutively. The first relation (4.9a) provides the free oscillations response. Solving Eqn. (4.9b) and (4.9c) causes secular terms that can be avoided by supposing conditions for the amplitude of $x(t)$. Applying this method up to the second order (T_2) provides the second

approximation

$$\begin{aligned} x(t) &= x_0(t) + \epsilon x_1(t) + \cdots \\ &= \hat{a}\cos(\gamma - \Omega\, t) + \frac{\eta}{6\omega^2}\hat{a}^2\left(\cos(2(\gamma - \Omega\, t)) - 3\right) + \mathcal{O}(\,\epsilon^2). \end{aligned} \tag{4.12}$$

The amplitude $\hat{e}$ and the phase γ are defined by

$$\frac{3\hat{a}^3\beta}{4} - 2\hat{a}\omega(\sigma - D_2\gamma) - \frac{5\hat{a}^3\eta^2}{6\omega^2} = \hat{e}\cos\gamma, \tag{4.13}$$

$$2\omega D_2\hat{a} + \hat{a}\mu\omega = \hat{e}\sin\gamma. \tag{4.14}$$

Combining both equations for steady-state motion ($D_2\hat{a}, D_2\gamma = 0$) leads to the frequency response equation to

$$\frac{\hat{e}^2}{4} = \left(\frac{3}{2}\hat{a}^3\beta + \hat{a}\sigma\omega\right)^2 + \frac{1}{4}\left(\hat{a}\mu\omega\right)^2. \tag{4.15}$$

From the frequency response equation the frequency response curves can be obtained

$$\sigma_1 = \frac{-3\,\hat{a}^3\beta - \sqrt{\hat{e}^2 - 2\hat{a}^2\alpha\mu^2}}{2\hat{a}\sqrt{2\alpha}}, \tag{4.16a}$$

$$\sigma_2 = \frac{-3\,\hat{a}^3\beta + \sqrt{\hat{e}^2 - 2\hat{a}^2\alpha\mu^2}}{2\hat{a}\sqrt{2\alpha}}. \tag{4.16b}$$

Figure 4.1 illustrates the frequency response curve. The two saddle-node bifurcations (b_{snL} and b_{snU}) are shown by the dashed lines. For any excitation frequency between the two bifurcation values, there are two amplitudes $\hat{a}$ possible: small or large amplitude oscillations. At this point it needs to be pointed out that the shown bifurcation values results from bifurcation conditions. In Fig. 4.1 the dashed lines indicate the solved bifurcation condition for the frequency shift σ.

The backbone curve (gray dashed-dotted line) provides the frequency where the amplitude exhibits a maximum. The backbone curve is given by

$$\sigma_b = -\frac{3\hat{a}^2\beta}{2\sqrt{2\alpha}}. \tag{4.17}$$

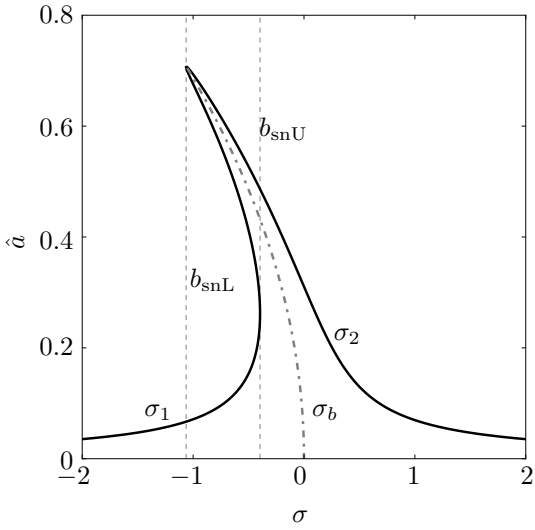

Figure 4.1: Frequency response relation for $\alpha = 1, \beta = 2, \mu = 0.2$, $\hat{e} = 0.2$.

The bifurcation condition can be solved for the excitation amplitude. In this case the bifurcation values read

$$\hat{e}_{\mathrm{snU}} = \frac{8}{9}\alpha^{3/4}\sqrt{\frac{\rho - 4\sigma}{\beta}}\sqrt{3\mu^2 - 2\sigma\,(2\sigma + \rho)}, \tag{4.18a}$$

$$\hat{e}_{\mathrm{snL}} = \frac{8}{9}\alpha^{3/4}\sqrt{\frac{\rho - 4\sigma}{\beta}}\sqrt{3\mu^2 + 2\sigma\,(2\sigma + \rho)}, \tag{4.18b}$$

with

$$\rho = \sqrt{4\sigma^2 - 3\mu^2}. \tag{4.19}$$

Figure 4.2 gives an illustration of these values. Between the two lines ($\hat{e}_{\mathrm{snL}}$ and $\hat{e}_{\mathrm{snU}}$) two stable possible oscillation amplitudes can be found.

4.1.1. Electromechanical system

In this section the multiple scales method is applied to the coupled equations (Eqn. 3.53). The findings can also be applied to any reduced form, by choosing

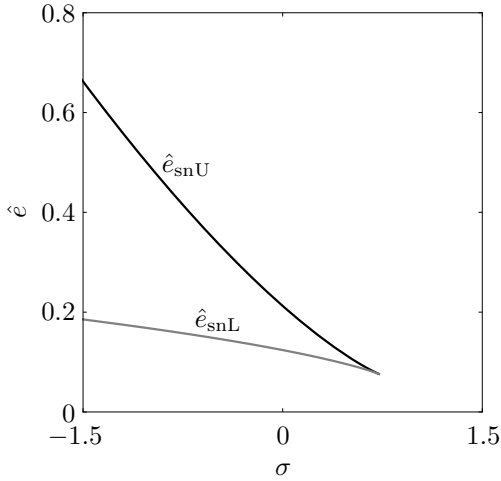

Figure 4.2: Bifurcation values for $\alpha = 1, \beta = 2, \mu = 0.2$.

the parameters accordingly. The coupled equations are given by the equations

$$\ddot{x}(t) + \mu\ \dot{x}(t) - \delta\ v(t) - \alpha\ x(t) + \beta\ x^3(t) = \hat{e}\ e(t), \tag{4.20a}$$

$$\phi\ v(t) + \eta\ \dot{x}(t) + \dot{v}(t) = 0. \tag{4.20b}$$

The equations are expressed about a stable equilibrium in order to apply the perturbation calculus. Similar to previous section, the nonlinearity, damping, excitation and electromechanical coupling are considered as perturbations of the undamped autonomous system. Thus, the perturbation parameter ϵ is introduced. The resulting equations read

$$\begin{aligned}\ddot{x}(t) + \epsilon^2\mu\ \dot{x}(t) - \epsilon^2\delta\ v(t) + \omega^2 x(t) + 3\epsilon\sqrt{\alpha\beta}\ x^2(t) \\ +\epsilon^2\beta\ x^3(t) = \epsilon^2\hat{e}\ e(t),\end{aligned} \tag{4.21a}$$

$$\phi\ v(t) + \gamma\ \dot{x}(t) + \dot{v}(t) = 0, \tag{4.21b}$$

with

$$\omega = \sqrt{2\alpha}. \tag{4.22}$$

The selected order of ϵ ensures that the damping μ, the electromechanical coupling δ, the nonlinearity β and the excitation $e(t)$ interact on the same

time scale. Similar to Section 4.1, the functions are expanded as

$$x(t,\epsilon) = x_0(T_0,T_1,T_2) + \epsilon x_1(T_0,T_1,T_2) + \epsilon^2 x_2(T_0,T_1,T_2), \tag{4.23a}$$

$$v(t,\epsilon) = v_0(T_0,T_1,T_2) + \epsilon v_1(T_0,T_1,T_2) + \epsilon^2 v_2(T_0,T_1,T_2). \tag{4.23b}$$

In the same way, as previously described, the perturbation calculus can be performed. This leads to the frequency response equation for the electromechanical beam

$$\left(\frac{3}{2}\hat{a}^3\beta + \hat{a}\ \omega\left(\sigma - \frac{\delta\gamma\omega}{2\left(\omega^2+\phi^2\right)}\right)\right)^2 + \frac{1}{4}\omega^2\hat{a}^2\left(\mu + \frac{\delta\gamma\phi}{\omega^2+\phi^2}\right)^2 = \frac{\hat{e}^2}{4}. \tag{4.24}$$

Comparing both derived frequency response equations (Eqns. 4.15 and 4.24), it is possible to see the effect of the electromechanical coupling on the overall dynamics. The terms within the equation illustrate the effective nonlinearity, eigenfrequency and the damping. The first term of the first parenthesis can be interpreted as the effective nonlinearity. A comparison between both relation shows the effective nonlinearity

$$\beta_{\text{eff}} = \frac{3}{2}\beta \tag{4.25}$$

which does not change. This is due to the fact that the electromechanical coupling is linear. With the other two contributions it is different. The eigenfrequency is altered by the elecromechanical coupling. This can be seen by the second term in the first parenthesis. The parenthesis containing the frequency deviation σ shows a frequency shift that depends on the electromechanical coupling. Thus,

$$\omega_{\text{eff}} = \omega + \frac{\delta\gamma\omega}{2\left(\omega^2+\phi^2\right)}. \tag{4.26}$$

The effective damping is visible in the second term in Eqn. (4.24)

$$\mu_{\text{eff}} = \mu + \frac{\delta\gamma\phi}{\omega^2+\phi^2}. \tag{4.27}$$

The influence of the electrical circuit can be seen in both relations. If the circuit is short-circuited ($\phi \to \infty$), the eigenfrequency and the damping are not affected by the electrical circuit. The result is, thus similar to the DUFFING equation (Eqn. 4.1). Nevertheless, the mechanical part of the piezoelectric element contributes to the stiffness coeffients α, β and $\hat{e}$. Both effective values (Eqns. 4.26 and 4.27) can be used to reduce an electromechanical system to a single equation. However, this will give an approximation which has the highest accuracy for small oscillations about a stable equilibrium. The approximated time solutions are given by

$$x(t) = \hat{a}\cos(\theta\ - t\Omega) + \frac{\eta}{6\omega^2}\hat{a}^2\left(\cos\left(2(\theta - t\Omega)\right) - 3\right) + \mathcal{O}(\ \epsilon^2), \tag{4.28a}$$

$$\begin{aligned} v(t) = \frac{1}{3}\gamma\hat{a}\Bigg(& \frac{\hat{a}\eta\cos\left(2(\theta - t\Omega) - \tan^{-1}\frac{\phi}{2\omega}\right)}{\omega\sqrt{4\omega^2 + \phi^2}} + \\ & \frac{3\hat{\omega}\cos\left(\theta - t\Omega - \tan^{-1}\frac{\phi}{\omega}\right)}{\sqrt{\omega^2 + \phi^2}}\Bigg) + \mathcal{O}(\ \epsilon^2), \end{aligned} \tag{4.28b}$$

with

$$\eta = 3\sqrt{\alpha\beta} \tag{4.29}$$

and the phase given by

$$\tan(\theta) = \frac{8\alpha^{3/2}\sigma + 3\sqrt{2}\hat{a}^2\beta\left(2\alpha + \phi^2\right) - 2\sqrt{2}\alpha\gamma\delta + 4\sqrt{\alpha}\sigma\phi^2}{2\sqrt{\alpha}(2\alpha\mu + \phi(\gamma\delta + \mu\phi))}. \tag{4.30}$$

The phase shift between the displacement $x(t)$ and the voltage $v(t)$ is visible in Eqn. (4.28). For the response within the first harmonic the phase shift is given by

$$\psi = \tan^{-1}\frac{\phi}{\omega}. \tag{4.31}$$

This phase shift is zero if the electrical circuit is open and unequal to zero if the electrical circuit is shut. This can be explained in terms of the introduced electrical damping.

4.1.2. Composite plate

This section presents a perturbation calculation for the equations of a composite plate derived in Section 3.3. For an analysis of the oscillations around the stable equilibrium, Eqn. (3.88) must be transformed to a stable equilibrium. This can be done with numerical tools. Thereby, it is also convenient to decouple the linear part of the equations. The parameter ϵ is introduced such that the solution on the fastest scale is given by the uncoupled autonomous system. Furthermore, the order of the parameters is set such that the damping, excitation and the nonlinearities interact on the same time scale. Therefore, the equation reads

$$\begin{aligned}&\ddot{\mathbf{p}} + \begin{bmatrix} \epsilon^2\mu_{11} & \mu_{12} \\ \mu_{21} & \epsilon^2\mu_{22} \end{bmatrix} \dot{\mathbf{p}} + \begin{bmatrix} \alpha_{11} & \epsilon^3\alpha_{12} \\ \epsilon^3\alpha_{21} & \alpha_{22} \end{bmatrix} \mathbf{p} + \\ &\begin{bmatrix} \kappa_{120}p_1^2 + \kappa_{102}p_2^2 + \kappa_{111}p_1p_2 + \beta_{112}p_1p_2^2 + \beta_{121}p_1^2p_2 \\ \kappa_{220}p_1^2 + \kappa_{202}p_2^2 + \kappa_{211}p_1p_2 + \beta_{212}p_1p_2^2 + \beta_{221}p_1^2p_2 \end{bmatrix} = \epsilon^3\hat{e}\ e(t).\end{aligned} \tag{4.32}$$

The variables are expanded to

$$p_1(t) = \epsilon\, u_{11}(T_0, T_1, T_2) + \epsilon^2 u_{12}^2(T_0, T_1, T_2) + \epsilon^3 u_{13}^3(T_0, T_1, T_2), \tag{4.33a}$$

$$p_2(t) = \epsilon\, u_{21}(T_0, T_1, T_2) + \epsilon^2 u_{22}^2(T_0, T_1, T_2) + \epsilon^3 u_{23}^3(T_0, T_1, T_2), \tag{4.33b}$$

with

$$T_n{=}\epsilon^n t. \tag{4.34}$$

The excitation function $e(t)$ reads

$$e(t) = \sin\left((\omega_1 + \epsilon^2\sigma)\, t\right) \tag{4.35}$$

and the eigenfrequencies are given by

$$\omega_1 = \sqrt{\alpha_{11}}, \tag{4.36a}$$

$$\omega_2 = \sqrt{\alpha_{22}}. \tag{4.36b}$$

After carrying out the perturbation, two coupled frequency response equations can be found. Both equations involve the amplitude $\hat{a}_1$ and $\hat{a}_2$. But, a single

frequency response equation is desirable. To this end, some assumptions can be used. For these considerations the equation is developed about the p_1-equilibrium, which means that it is transformed to the equilibrium where $p_1 \gg p_2$. Because the system is excited with a frequency close to the eigenfrequency ω_1, it can be assumed that the amplitude of $p_2(t)$ is much lower than the one of $p_1(t)$. Thus, it is assumed that $\hat{a}_2 = 0$. This allows to solve both frequency response equations in a straight-forward manner. The remaining equation is, then, given by

$$\left(\hat{a}_1^3 \frac{\left(3\kappa_{111}\kappa_{220}\omega_1^2\left(3\omega_2^2 - 8\omega_1^2\right) + 10\kappa_{120}^2\omega_2^2\left(\omega_2^2 - 4\omega_1^2\right)\right)}{24\omega_1^2\omega_2^2\left(\omega_2^2 - 4\omega_1^2\right)} + \hat{a}_1\sigma\omega_1\right)^2 + \frac{1}{4}\left(\hat{a}_1\mu_{11}\omega_1\right)^2 = \frac{1}{4}\hat{e}. \tag{4.37}$$

Equation (4.37) describes the relation between the frequency deviation σ and the amplitude $\hat{a}_1$. The relation contains the eigenfrequencies ω_i, given by Eqn. (4.36). These relations can be assumed, if the entries on the antidiagonal of the matrix containing the linear terms in Eqn (4.33) are small. However, if that is not the case, the eigenfrequencies can be calculated from Eqn. (4.33) and used instead. Finally, Eqn. (4.37) can be solved to obtain the lower (b_{snL}) and the upper (b_{snU}) saddle node bifurcation.

4.2. The Melnikov function

This section presents the Melnikov function. The Melnikov function [23, 50, 75] can be exploited to provide a necessary condition for homoclinic orbits. A homoclinic orbit is characterized by a trajectory that joins the stable and unstable manifold of an equilibrium. The function can be used to provide a necessary condition for cross-well oscillations. Moreover, the Melnikov function can be used to provide a conservative criterion for inter-well oscillations. For the one degree of freedom case, the Melnikov function results in the

energy balance

$$\mu \int_I \dot{x}^2(t)\mathrm{d}t = \hat{e} \int_I \sin(\Omega t)\dot{x}(t)\mathrm{d}t, \tag{4.38}$$

where I is a interval of the periodic solution $x(t)$, e.g. one period. This energy balance balances the terms that dissipate and introduce the energy within the system. For the solution of the energy balance, the bistable DUFFING equation

$$\ddot{x}(t) + \mu\dot{x}(t) - x(t) + \gamma\ x^3(t) = \hat{e}\ \sin(\Omega t) \tag{4.39}$$

is considered. The main interest are harmonic oscillations. The integration interval I is yet to be determined. Under the assumption that the solution of Eqn. (4.39) is close to the one of the unperturbed system

$$\ddot{x}(t) - x(t) + \gamma\ x^3(t) = 0, \tag{4.40}$$

the period length can be derived by considering the kinetic energy $\mathcal{T}$ and the potential energy $\mathcal{U}$ of Eqn. (4.40). The energies are defined by

$$\mathcal{T} = \frac{1}{2}\dot{x}^2, \tag{4.41}$$

$$\mathcal{U} = -\frac{1}{2}x^2 + \frac{1}{4}\gamma x^4. \tag{4.42}$$

It follows that

$$E_0 = \mathcal{T} + \mathcal{U} = \frac{1}{2}\dot{x}^2 - \frac{1}{2}x^2 + \frac{1}{4}\gamma x^4, \tag{4.43}$$

where E_0 is the total mechanical energy in the system. Equation (4.43) can be solved for $\dot{x}$ to give

$$\dot{z} = \pm\sqrt{E_0\gamma + z^2 - z^4}, \tag{4.44}$$

where the transformation

$$z = x\sqrt{\gamma/2} \tag{4.45}$$

was applied. The period length follows directly from Eqn. (4.44) by rearrangement and integration

$$P_{\mathrm{S}} = 2\int_{z_{\min}}^{z_{\max}} \frac{1}{\sqrt{E_0\gamma + z^2 - z^4}}\mathrm{d}z, \tag{4.46a}$$

$$P_{\mathrm{I}} = 4\int_{0}^{z_{\max}} \frac{1}{\sqrt{E_0\gamma + z^2 - z^4}}\mathrm{d}z, \tag{4.46b}$$

where the indices denote single-well (S) and inter-well (I) oscillations.

The integration limits are obtained by setting $E_0 = \mathcal{U}$, which leads to

$$z_{\max} = \frac{1}{\sqrt{2}}\sqrt{1 + \sqrt{4E_0\gamma + 1}}, \tag{4.47}$$

$$z_{\min,\mathrm{S}} = \frac{1}{\sqrt{2}}\sqrt{1 - \sqrt{4E_0\gamma + 1}}, \tag{4.48}$$

$$z_{\min,\mathrm{I}} = -z_{\max,\mathrm{I}}. \tag{4.49}$$

The integration limits for the homoclinic orbit can be obtained from Eqn. (4.44) by setting $E_0\gamma = 0$. Integrating the resulting equation and solving for z leads to

$$z_h(t) = \pm\frac{1}{\cosh t}. \tag{4.50}$$

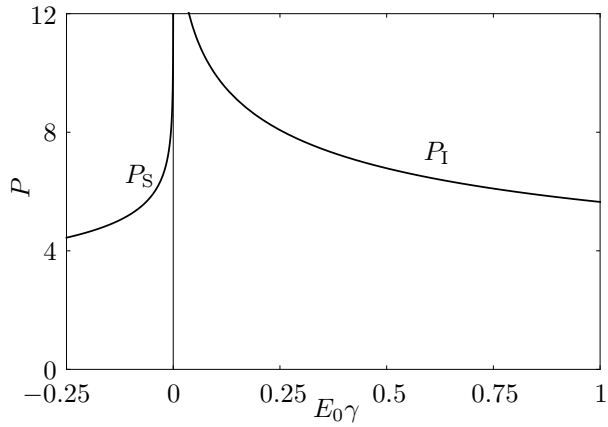

Figure 4.3: Energy-period relations (Eqn. 4.46)

Figure 4.3 illustrates the relation between initial energy $E_0\gamma$ and the period length. With Eqns. (4.44 and 4.46b) the terms within the energy balance (4.38) can be evaluated to

$$\begin{aligned}\int_I \dot{x}^2(t)\mathrm{d}\tau &= \frac{2}{\gamma}\int_I \dot{z}^2(t)\mathrm{d}t \\ &= \frac{4}{\gamma}\int_{I_2} \sqrt{\gamma E_0 + z^2 - z^4}4\mathrm{d}z = \frac{4}{\gamma} f_1(E_0\gamma),\end{aligned} \tag{4.51a}$$

$$\begin{aligned}\int_I \sin(\Omega t)\dot{y}(t)\mathrm{d}\tau &= \sqrt{\frac{2}{\gamma}}\int_I \sin(\Omega t)\dot{z}(t)\mathrm{d}t \\ &= 2\sqrt{\frac{2}{\gamma}}\int_{I_2} \sin\left(\Omega \int_{z_{\min}}^{z_0} \frac{d\xi}{\sqrt{\gamma E_0 + \xi^2 - \xi^4}}\right)\mathrm{d}z_0 \\ &= 2\sqrt{\frac{2}{\gamma}} f_2(E_0\gamma, \Omega).\end{aligned} \tag{4.51b}$$

Here I_2 means the half interval. For single-well oscillations the interval is given by

$$I_2 = [z_{\min,\mathrm{IW}}, z_{\max}] \tag{4.52}$$

and for inter-well oscillations

$$I_2 = [z_{\min}, z_{\max}]. \tag{4.53}$$

For the homoclinic orbits the integration interval reads

$$I_2 = [-z_h, z_h], \tag{4.54}$$

whereby z_h is given by Eqn. (4.50). With the derived terms, the normalized critical excitation amplitude $\hat{\bar{e}}$ values can be obtained to

$$\hat{\bar{e}}_{\mathrm{crit}}(\Omega) = \frac{f_1(E_0\gamma)}{f_2(E_0\gamma, \Omega)}. \tag{4.55}$$

If the transformation (Eqn. 4.45) is reversed, the critical excitation amplitude $\hat{e}_{\mathrm{crit}}$ to obtain homoclinic oscillations reads

$$\hat{e}_{\mathrm{crit}}(\Omega) = \mu\sqrt{\frac{2}{\gamma}}\hat{\bar{e}}_{\mathrm{crit}}(\Omega). \tag{4.56}$$

Figure 4.4 shows an illustration of the critical excitation amplitudes $\hat{\hat{e}}_{\text{crit}}$ for the three considered oscillation types. Each line gives a threshold for obtaining a specific oscillation type. The most interesting cure is given by the upper one. The upper line gives the bifurcation value for inter-well oscillations. Thus, above this threshold inter-well oscillations might be observed.

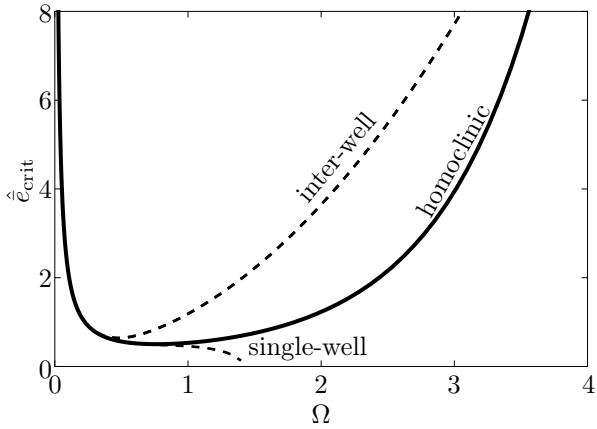

Figure 4.4: Normalized bifurcation values for the three oscillation types: single-well, homoclinic and inter-well oscillations

4.3. Criterion for chaos

Szemplińska-Stupnicka [111–113] derived a criterion to predict chaotic oscillations. This is done by means of different single degree of freedom systems. The derived criterion is more accurate compared to the Melnikov function in the limitation of the domain where chaos can exist, especially for low damping values.

One route to chaos is through period-doubling bifurcations. In many systems the onset of chaos emerges from oscillations that repeat after $T = n\frac{2\pi}{\Omega}$, with Ω being the excitation frequency and $n = 2, 4, ...$ Mathematically expressed, chaos exists if $n \to \infty$. Period-doubling appears when a critical parameter is exceeded. Typically, as the parameter is further increased, the system rapidly goes through a period-doubling cascade until chaotic oscillations are present. In the following the procedure is shown by means of the bistable Duffing

equation. An extension to the electromechanically coupled system is derived subsequently.

4.3.1. Bistable oscillator

The idea of Szemplińska-Stupnicka is to search for the first stable period-doubling bifurcation. For the procedure it is convenient to use the transformed equation

$$\ddot{x}(t) + \mu\dot{x}(t) - x(t) + \gamma\ x^3(t) = \hat{e}\ \sin(\Omega t). \tag{4.57}$$

For the investigations, the equation is shifted to a stable equilibrium

$$\ddot{x}(t) + \mu\dot{x}(t) + 2x(t) - 3\sqrt{\gamma}x^2(t) + \gamma x^3(t) = \hat{e}\ \sin(\Omega t). \tag{4.58}$$

To search solutions with double period oscillations the following *ansatz* is made

$$x(t) = x^*(t) + \delta x(t). \tag{4.59}$$

Where $x^*(t)$ represents an approximate solution obtained by perturbation calculus (Eqn. 4.12)

$$x^*(t) = \hat{a}\cos(t\Omega) + \frac{1}{4}\sqrt{\gamma}\ \hat{a}^2\cos(2t\Omega) - \frac{3}{4}\hat{a}^2\sqrt{\gamma}. \tag{4.60}$$

A variation of Eqn. (4.58) in $x(t)$ is carried out. This leads to

$$\delta\ddot{x}(t) + \mu\delta\dot{x}(t) + \delta x(t)\left(2 - 6\sqrt{\gamma}x^*(t) + 3\gamma{x^*}^2(t)\right) = 0. \tag{4.61}$$

The term in the parenthesis is expanded into a Taylor series, leading to a linear variational Hill type equation

$$\delta\ddot{x}(t) + \mu\delta\dot{x}(t) + \delta x(t)\left(\lambda_0 + \sum_{i=1}^{n}\lambda_i\cos(n\Omega t)\right) = 0. \tag{4.62}$$

The disturbance $\delta x(t)$ is modeled as

$$\delta x(t) = e^{\epsilon t}\phi(t), \qquad \text{with} \tag{4.63a}$$

$$\phi(t) = \sum_{i=1}^{n} a_i\cos\left(\frac{1}{2}i\Omega t\right) + b_i\sin\left(\frac{1}{2}i\Omega t\right),\ n = 1, 3, ... \tag{4.63b}$$

Inserting Eqn. (4.63) into Eqn. (4.62) for the critical parameter $\epsilon = 0$, the following equation can be assembled

$$\mathbf{A} \begin{bmatrix} a_1 \\ b_2 \\ \vdots \\ a_n \\ b_n \end{bmatrix} = 0. \tag{4.64}$$

For non-trivial solutions the matrix $\mathbf{A}$ has to fulfill the condition

$$\det \mathbf{A} = 0. \tag{4.65}$$

Solving the resulting equations, the borders of the instability regions can be identified. Figure 4.5 illustrates the instability domain. The intersection between the instability regions and the frequency response curve gives the critical excitation frequency for which period-doubling bifurcations emerge [111]. Thus, the intersection can be expressed in terms of excitation amplitude $\hat{e}$ to obtain the bifurcation value for chaos.

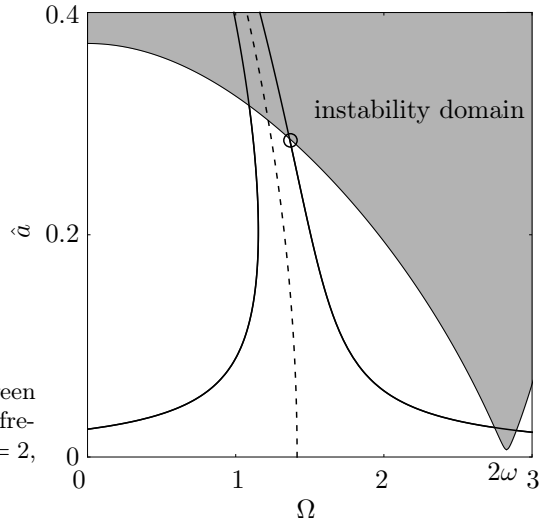

Figure 4.5: Intersection between period-doubling domain and frequency response curve for ($\gamma = 2$, $\mu = 0.02$ and $\hat{e} = 0.1$)

4.3.2. Electromechanical system

In this section an extension for electromechanically coupled equations (3.53) is presented. To this end, the equations of motion for the electromechanical system need to be transformed to a stable equilibrium. This results in the equations

$$\ddot{x}(t) + \mu\ \dot{x}(t) - \kappa\ v(t) + \omega^2 x + \eta\ x^2(t) + \beta\ x^3(t) = \bar{e}\ e(t), \tag{4.66a}$$

$$\phi\ v(t) + \gamma\ \dot{x}(t) + \ \dot{v}(t) = 0, \tag{4.66b}$$

with

$$\omega = \sqrt{2\alpha},$$
$$\eta = 3\sqrt{\alpha\beta}.$$

Applying a variation in $x(t)$ and $v(t)$ and presenting the equations in a Taylor series yields in the Hill type equations

$$\delta\ddot{x}(t) - \kappa\ \delta\dot{v}(t) + \mu\ \delta\dot{x}(t) + \delta x(t)\left(\lambda_0 + \sum_{i=1}^{4}\lambda_i \cos(n\Omega t)\right) = 0, \tag{4.67a}$$

$$\phi\ \delta v(t) + \gamma\ \delta\dot{x}(t) + \delta\dot{v}(t) = 0 \tag{4.67b}$$

with the coefficients

$$\lambda_0 = \frac{57\hat{a}^4\beta^2}{32\alpha} - 3\hat{a}^2\beta + 2\alpha, \qquad \lambda_1 = \frac{3a\beta\left(8\alpha - 5\hat{a}^2\beta\right)}{4\sqrt{\alpha\beta}},$$
$$\lambda_2 = \frac{3}{8}\hat{a}^2\beta\left(8 - \frac{3\hat{a}^2\beta}{\alpha}\right), \qquad \lambda_3 = \frac{3\hat{a}^3\beta^2}{4\sqrt{\alpha\beta}}, \tag{4.68}$$
$$\lambda_4 = \frac{3\hat{a}^4\beta^2}{32\alpha}.$$

Where the approximated solutions (Eqn. 4.28) are used for the variables $x(t)$ and $v(t)$. This yields in the bifurcation condition for stable period-doubling

bifurcations

$$\begin{aligned}3249\hat{a}^8\beta^4\theta + 4096\alpha^4\theta - 1024\alpha^3\left(21\hat{a}^2\beta\theta + \lambda\Omega^2\right) + 64\alpha^2\Big(438\hat{a}^4\beta^2\theta + \\ 24\hat{a}^2\beta\lambda\Omega^2 + \Omega^2\left(16\gamma^2\kappa^2 + 32\gamma\kappa\mu\phi - 8\gamma\kappa\Omega^2 + 4\theta\mu^2 + \theta\Omega^2\right)\Big) - \\ 48\alpha\hat{a}^4\beta^2\left(303\hat{a}^2\beta\theta + 19\lambda\Omega^2\right) = 0.\end{aligned} \tag{4.69}$$

with

$$\theta = 4\phi^2 + \Omega^2, \tag{4.70a}$$

$$\lambda = \theta - 4\gamma\kappa. \tag{4.70b}$$

4.4. Harmonic balance

4.4.1. Bistable system

The harmonic balance method [95] is a powerful tool to obtain steady-state responses of nonlinear differential equations. Furthermore, it can be used to derive bifurcations conditions. A prerequisite for this method is to know characteristics of the solution. According to the expected solution an *ansatz* is made. Otherwise, a high number of terms need to be included in the harmonic expansion

$$x(t) = \sum_{n=1}^{m} A_n \cos\left(n\Omega t\right) + B_n \sin\left(n\Omega t\right), \quad n = 1, 2, ... \tag{4.71}$$

for sufficient accuracy. The accuracy of the method can be checked by considering the error that is represented by the terms higher than a certain order m. Nonetheless, a high number of terms in Eqn. (4.71) should be avoided, since the calculations become rapidly cumbersome and analytically unsolvable. Inserting Eqn. (4.71) into (3.22) and balancing the amplitude coefficients up to

the developed order m leads to

$$\mathbf{A} \begin{bmatrix} \cos(\Omega t) \\ \sin(\Omega t) \\ \vdots \\ \cos(m\ \Omega t) \\ \sin(m\ \Omega t) \end{bmatrix} = 0 \tag{4.72}$$

The solution of Eqn. (4.72) gives different solutions for the amplitudes A_n, B_n. The solutions are either stable or unstable. The stability of each obtained solution can be verified by FLOQUET theory [51]. This helps to identify stable and unstable solutions. The FLOQUET theory will be presented in the next section.

This method is applied to calculate an approximation of stable inter-well oscillations. Solving Eqn. (4.72) for the amplitudes A_n and B_n, three analytic solutions are found, see Fig. 4.6. The critical value for which stable solutions emerge is the bifurcation value for stable inter-well oscillations (b_{snI}). The black dashed lines represent unstable solutions, identified by the FLOQUET theory. The lowest unstable solution branch represents oscillations about the unstable equilibrium with small amplitudes. The second unstable branch emerges from the bifurcation value b_{snI} and is the node of the inter-well saddle.

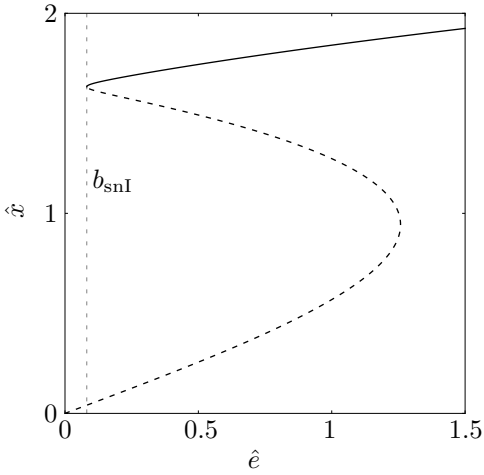

Figure 4.6: Bifurcation diagram obtained by the harmonic balance method. The solid (dashed) branch indicates stable (unstable) solutions. The saddle-node bifurcation b_{snI} is indicated by the vertical gray dashed line ($\alpha = 1, \beta = 2, \mu = 0.05$)

In the case of $m = 1$, the solution can be obtained in closed form. Solving the bifurcation condition for the excitation amplitude $\hat{e}$ leads to

$$\hat{e}_{snI} = \frac{2\mu\sqrt{\alpha + \Omega^2}}{\Omega\sqrt{3\beta}}. \tag{4.73}$$

For higher orders of m, the solution can be obtained numerically. In the same way, coupled equations can be analyzed. However, an analytical solution is usually not possible.

4.4.2. Electromechanical system

For the coupled equations (Eqn. 3.52 or 3.55) the following *ansatz*

$$x(t) = \sum_{n=1}^{m} A_n \cos(n\Omega t) + B_n \sin(n\Omega t), \tag{4.74a}$$

$$v(t) = \sum_{n=1}^{m} C_n \cos(n\Omega t) + D_n \sin(n\Omega t), \tag{4.74b}$$

is made for triggering inter-well oscillations. Inserting Eqn. (4.74) into the reduced equation (3.55) and balancing the different harmonics, solutions for the amplitudes $A_n ... D_n$ can be obtained. These solutions are only stable for specific excitation parameters. For inter-well oscillations the critical excitation amplitude $\hat{e}$ needs to be above the threshold value

$$\begin{aligned}\hat{e}_{snI} = &\frac{2\sqrt{2\kappa}}{9\kappa^2}\Bigg(\left(\Omega^2\left(\lambda-\delta^2\right)+\lambda\phi^2\right)\left(\delta^2\Omega^2\left(\delta^2\left(\Omega^2+9\phi^2\right)-2\kappa(\lambda-9\mu\phi)\right)\right.\\ &\left.+\kappa^2\rho\right)-\sqrt{\left(\delta^2\Omega^2\left(\delta^2\left(\Omega^2-3\phi^2\right)-2\kappa(\lambda+3\mu\phi)\right)+\kappa^2\nu\right)^3}\Bigg)^{1/2},\end{aligned} \tag{4.75}$$

with

$$\lambda = 1 - \Omega^2, \qquad \kappa = \Omega^2 + \phi^2,$$
$$\nu = \left(2 - 3\mu^2\right)\Omega^2 + \Omega^4 + 1, \qquad \rho = \left(9\mu^2 + 2\right)\Omega^2 + \Omega^4 + 1.$$

4.5. FLOQUET theory

FLOQUET theory[2] [51, 95] is a useful tool for analysing the stability of linear systems with periodic coefficients such as parameter excitation or self-excitation. A linear differential equation with periodic coefficients reads

$$\dot{\mathbf{x}} = \mathbf{A}(t)\mathbf{x}. \tag{4.76}$$

The matrix $\mathbf{F}(t)$ which fulfills the equation

$$\mathbf{x}(T) = \mathbf{F}(T)\mathbf{x}_0 \tag{4.77}$$

and $\mathbf{F}(0) = \mathbf{I}$ is the so-called the fundamental matrix of the linear system (4.76). The solution of Eqn. (4.76) can be written as $\mathbf{x}(t) = \mathbf{F}(t)\mathbf{x}_0$. Resulting from the theorem of FLOQUET the fundamental matrix can be approximated by

$$\mathbf{F}(T) = e^{\mathbf{B}T}. \tag{4.78}$$

The matrix $e^{\mathbf{B}T}$ is called the monodromy matrix. With this representation of the fundamental matrix the solution of Eqn. (4.76) is written as

$$\mathbf{x}(T) = e^{\mathbf{B}T}\mathbf{x}_0. \tag{4.79}$$

Thus, eigenvalues of the matrix $e^{\mathbf{B}T}$ determine the stability of the system. The eigenvalues of the monodromy matrix are called FLOQUET multipliers. If the absolute value of one eigenvalue is larger than one, the trivial solution of (4.76) is unstable, if all absolute values of the eigenvalues are smaller than one, the trivial solution is asymptotically stable. It can be shown [51] that the stability of a periodic solution of the linear equation (4.76) also applies for the nonlinear system

$$\dot{\mathbf{x}} = \mathbf{A}(t)\mathbf{x} + \mathbf{h}(x,t) = \mathbf{f}(\mathbf{x},t) \tag{4.80}$$

if the nonlinearity is restricted by

$$|\mathbf{h}(x,t)| \leqslant a\,|\mathbf{x}|^b\,, a \geqslant 0, b > 1. \tag{4.81}$$

[2] After Gaston FLOQUET (1847-1920), published 1883, French mathematician

for analyzing the stability of a periodic solutions of a nonlinear system, the equation initially needs to be transformed into the form (4.80). To this end, the coordinate transformation

$$\mathbf{x} = \mathbf{x}^* + \delta\mathbf{x} \tag{4.82}$$

is made. The vector $\mathbf{x}^*$ is the solution of the nonlinear system (4.80) and $\delta\mathbf{x}$ is a small disturbance of this solution. Inserting this transformation into Eqn. (4.80) yields

$$\dot{\mathbf{x}}^* + \delta\dot{\mathbf{x}} = \mathbf{f}(\mathbf{x}^* + \delta\mathbf{x}, t) \tag{4.83}$$

$$\delta\dot{\mathbf{x}} = \mathbf{f}(\mathbf{x}^* + \delta\mathbf{x}, t) - \dot{\mathbf{x}}^* \tag{4.84}$$

Now the right-hand side can be linearized. This leads to

$$\delta\dot{\mathbf{x}} = \mathbf{A}(t)\delta\mathbf{x}. \tag{4.85}$$

For this formulation FLOQUET's theorem can be applied to determine the stability.

In many cases, only an approximate solution $\tilde{\mathbf{x}}^*$ is known. Thus, it can be advantageous to subtract the equation

$$\dot{\tilde{\mathbf{x}}}^* = \mathbf{f}(\tilde{\mathbf{x}}^*, t) \tag{4.86}$$

from the right-hand side of Eqn. (4.84)

$$\delta\dot{\mathbf{x}} = \mathbf{f}(\tilde{\mathbf{x}}^* + \delta\mathbf{x}, t) - \dot{\tilde{\mathbf{x}}}^* - \left(\mathbf{f}(\tilde{\mathbf{x}}^*, t) - \dot{\tilde{\mathbf{x}}}^*\right). \tag{4.87}$$

With this step, the equation is transformed to the exact periodic solution, thus the error between the exact and the approximation solution is adjusted. This has the benefit of avoiding small error terms and terms of higher order that come along by using an approximate solution for the transformation.

The solution of Eqn. (4.87) can finally be obtained and presented as shown in Eqn. (4.79). The stability is determined according to the eigenvalues of the monodromy matrix.

4.6. Normal form theory

Within this section the normal form theory is presented. The procedure is based on the ones presented by Troger and Steindl [121], Murdock [92] and Hochlenert [57]. The basic idea of the normal form theory is to transform an autonomous system of differential equations to a from with reduced terms. This can be achieved by coordinate transformations. The first reference of this idea seems to be by Poincaré [92]. However, it is difficult to allocate a specific person to this theory since it has been developed and extended by various persons.

The aim of the normal form is to reduce the system's complexity such that it allows to analyze the behavior near a bifurcation point. This includes the analysis of the stability behavior or the estimation of the basins of attraction, e.g. by construction of Lyapunov functions. For example, the normal form theory was applied by Spelsberg-Korspeter et al. [106] to a Van der Pol oscillator to estimate the basins of attraction by construction suitable Lyapunov functions.

4.6.1. Normal form transformation

Let us start with the autonomous system

$$\dot{\mathbf{q}}(t) = \mathbf{A}\mathbf{q}(t) + \mathbf{g}(\mathbf{q}(t)) \tag{4.88}$$

having the trivial solution $\mathbf{q}(t) = \mathbf{0}$. The case of non-autonomous treatment will be presented later. The system (Eqn. 4.88) can be expanded in a Taylor series to read

$$\dot{\mathbf{q}}(t) = \mathbf{A}\mathbf{q}(t) + \mathbf{f}_2(\mathbf{q}(t)) + \mathbf{f}_3(\mathbf{q}(t)) + \cdots . \tag{4.89}$$

In order to apply a normal form transformation, the system matrix $\mathbf{A}$ needs to be decoupled. This can be achieved in the generic case by bringing the system matrix $\mathbf{A}$ to Jordan form by the transformation

$$\mathbf{\Lambda} = \mathbf{R}^{-1}\mathbf{A}\mathbf{R} = \mathrm{diag}[\lambda_1, \cdots, \lambda_n], \tag{4.90}$$

with $\mathbf{R}$ being the modal matrix and λ_i the eigenvalues of $\mathbf{A}$. The coordinates can be transformed to the modal coordinates by

$$\mathbf{q} = \mathbf{R}\mathbf{x}. \tag{4.91}$$

Thus, a system with decoupled linear terms is obtained

$$\dot{\mathbf{x}}(t) = \mathbf{\Lambda}\mathbf{x}(t) + \mathbf{R}^{-1}\mathbf{f}_2(\mathbf{R}\mathbf{x}(t)) + \mathbf{R}^{-1}f_3(\mathbf{R}\mathbf{x}(t)) + \cdots . \tag{4.92}$$

It is convenient to introduce a notation for the following transformation. Equation (4.92) can be rewritten as

$$\dot{\mathbf{x}} = \mathbf{f}(\mathbf{x}) = \mathbf{\Lambda}+\mathbf{F}\mathbf{x}_2 + \mathbf{F}\mathbf{x}_3 + \cdots \tag{4.93}$$

with the vectors containing the polynomials of order i

$$\mathbf{F}\mathbf{x}_i = \begin{bmatrix} \vdots \\ c_{11}x_1^{m_{11}} \cdots c_{1n}x_n^{m_{1n}} + \cdots + c_{j1}x_1^{m_{j1}} \cdots c_{jn}x_n^{m_{jn}} \\ \vdots \end{bmatrix} . \tag{4.94}$$

with

$$\sum_{k=1}^{n} m_{jk} = i. \tag{4.95}$$

The aim of the normal form transformation is to transform (4.93) into to the easier normal form

$$\dot{\mathbf{y}} = \mathbf{h}(\mathbf{y}) = \mathbf{\Lambda}\mathbf{y}(t) + \mathbf{H}\mathbf{y}_2 + \mathbf{H}\mathbf{y}_3 + \cdots \tag{4.96}$$

which allow possible (semi-)analytical investigations. This is done by the yet unknown transformation

$$\mathbf{x} = \mathbf{g}(\mathbf{y}) = \mathbf{y} + \mathbf{G}\mathbf{y}_2 + \mathbf{G}\mathbf{y}_3 + \cdots . \tag{4.97}$$

This transformation clearly shows that the normal form is an approximation of the underlying system. The quality of the approximation can be increased by

the order of the transformation. Moreover, the order should be large enough to preserve the essential features of the original dynamical system.

Inserting the transformation (4.97) into Eqn. (4.93) results in the partial differential equation

$$\frac{\partial \mathbf{g}(\mathbf{y})}{\partial \mathbf{y}}\mathbf{h}(\mathbf{y}) = \mathbf{f}\big(\mathbf{g}(\mathbf{y})\big) \tag{4.98}$$

is obtained. The functions $\mathbf{g}(\mathbf{y})$ and $\mathbf{h}(\mathbf{y})$ can be determined by a coefficient comparison. The linear term is not affected by the transformation as seen in Eqn. (4.97). For higher orders the coefficient comparison reveals the relation

$$\mathbf{H}\mathbf{y}_i = \tilde{\mathbf{F}}\mathbf{y}_i + \mathbf{\Lambda}\mathbf{G}\mathbf{y}_i - \frac{\partial \mathbf{G}\mathbf{y}_i}{\partial \mathbf{y}}\Lambda\mathbf{y}, \tag{4.99}$$

where the polynomial $\tilde{\mathbf{F}}\mathbf{y}_i$ results from the previous transformation orders. This implies that the transformation needs to be carried out consecutively. If a single monomial of (4.99)

$$\mathbf{H}\mathbf{y}_{i,k} = \tilde{\mathbf{F}}\mathbf{y}_{i,k} + \big(\lambda_k - (m_{k1}\lambda_1 + m_{k2}\lambda_2 + \cdots + m_{kn}\lambda_n)\big)\mathbf{G}\mathbf{y}_{i,k} \tag{4.100}$$

is considered, the unknown coefficients can be determined. From the term in the brackets the resonance condition can be formulated

$$\lambda_k = (m_{k1}\lambda_1 + m_{k2}\lambda_2 + \cdots + m_{kn}\lambda_n), \quad k = 1, \cdots, n, \quad \sum_{j=1}^{n} m_{kj} = i. \tag{4.101}$$

If the resonance condition is fullfilled, the monomial $\tilde{\mathbf{F}}\mathbf{y}_{i,k}$ can not be eliminated by the normal form transformation. Thus

$$\mathbf{H}\mathbf{y}_{i,k} = \tilde{\mathbf{F}}\mathbf{y}_{i,k} \tag{4.102}$$

$$\mathbf{G}\mathbf{y}_{i,k} = 0. \tag{4.103}$$

On the other hand, if the resonance condition can not be fullfilled, a transformation can be made

$$\mathbf{H}\mathbf{y}_{i,k} = 0, \tag{4.104}$$

$$\mathbf{G}\mathbf{y}_{i,k} = \frac{\tilde{\mathbf{F}}\mathbf{y}_{i,k}}{(m_{k1}\lambda_1 + m_{k2}\lambda_2 + \cdots + m_{kn}\lambda_n) - \lambda_k}. \tag{4.105}$$

Analogously the back transformation

$$\mathbf{y} = \mathbf{k}(\mathbf{x}) = \mathbf{x} + \mathbf{K}\mathbf{x}_2 + \mathbf{K}\mathbf{x}_3 + \cdots \tag{4.106}$$

can be obtained by a coefficient comparison.

4.6.2. Transformation of non-autonomous systems

Many dynamical systems are non-autonomous, i.e. excitation or periodic coefficients are present. In the previous section, the normal form transformation was applied to autonomous systems. As will be shown now, it is possible to transform non-autonomous systems in the form of Eqn. (4.88). The general form of an non-autonomous system reads

$$\dot{\mathbf{q}}(t) = \mathbf{f}(\mathbf{q}(t), \cos(\mathbf{\Omega}_i t), \sin(\mathbf{\Omega}_i t)), \tag{4.107}$$

where $\mathbf{\Omega}$ is a vector containing all frequency components of the harmonic functions . If the following relations are formulated

$$\cos(\mathbf{\Omega}_i t) = \frac{1}{2}\big(\mathbf{u}_i(t) + \mathbf{v}_i(t)\big), \tag{4.108a}$$

$$\sin(\mathbf{\Omega}_i t) = \frac{1}{2}\big(\mathbf{v}_i(t) - \mathbf{u}_i(t)\big), \tag{4.108b}$$

it is possible to embed harmonic terms into the system equation as new variables. The new variables are defined by

$$u_i(t) = e^{\mathrm{i}\Omega_i t}, \tag{4.109a}$$

$$v_i(t) = e^{-\mathrm{i}\Omega_i t}. \tag{4.109b}$$

The extended system eventually reads

$$\begin{bmatrix} \dot{\mathbf{q}}(t) \\ \dot{\mathbf{u}}(t) \\ \dot{\mathbf{v}}(t) \end{bmatrix} = \begin{bmatrix} \mathbf{f}\big(\mathbf{q}(t), \frac{1}{2}(\mathbf{u}(t) + \mathbf{v}(t)), \frac{1}{2}\mathrm{i}(\mathbf{v}(t) - \mathbf{u}(t))\big) \\ \mathrm{i}\mathbf{\Omega}\mathbf{u}(t) \\ -\mathrm{i}\mathbf{\Omega}\mathbf{v}(t) \end{bmatrix}. \tag{4.110}$$

This system is again an autonomous system

$$\dot{\bar{\mathbf{q}}}(t) = \mathbf{A}\bar{\mathbf{q}}(t) + \mathbf{g}(\bar{\mathbf{q}}(t)), \tag{4.111}$$

which can be brought into normal form as shown in the previous section.

4.6.3. Application to the bistable DUFFING equation

In this section the normal form theory will be used to analyze the bistable DUFFING equation. HOCHLENERT [57] analyzed a monostable DUFFING and a VAN DER POL oscillator using the normal form theory. This allows to predict the domains of attraction amongst others. This worked well, since both oscillators only show two oscillation types. In this case, the phase space or the initial condition can be split between both oscillation types. This will be more involved for the bistable DUFFING equation. In order to apply the normal from transformation, the equation

$$\ddot{p}(t) + \mu\dot{p}(t) - \alpha p(t) + \beta p^3(t) = \hat{e}\cos(\Omega t) \tag{4.112}$$

has to be arranged into a system of first order. The parameters μ and Ω will be interpreted as variables so that the state space is extended. This allows to apply the transformation even though the values will be set later. The normal form needs to be developed about a bifurcation point. This assures, that most of the system features are preserved by the transformation. In this case, it is not possible to develop the transformation about the point for $\alpha = 0$ (supercritical pitchfork bifurcation) due to many resonating terms which do not allow to simplify the equation. The transformation is instead developed about the HOPF[3] -bifurcation point for $\mu = 0$. The modified and extended equation reads

$$\dot{\mathbf{q}} = \mathbf{A}\ \mathbf{q} + \mathbf{g}(\mathbf{q}), \tag{4.113}$$

with the variables

$$\begin{aligned} q_1 &= p, & q_3 &= \sqrt{\hat{e}}\, e^{\frac{1}{2}\mathrm{i}\Omega t}, & q_5 &= \mu, & e(t) &= \frac{1}{2}(q_3^2 + q_4^2), \\ q_2 &= \dot{p}, & q_4 &= \sqrt{\hat{e}}\, e^{-\frac{1}{2}\mathrm{i}\Omega t}, & q_6 &= \Omega - 1, & q_7 &= \alpha - 1 \end{aligned}$$

[3] Eberhard HOPF (1902-1983), Austria-Hungarian mathematician and astronomer

where

$$\mathbf{A} = \begin{bmatrix} 0 & 1 & 0 & 0 & 0 & 0 & 0 \\ -1 & 0 & 0 & 0 & 0 & 0 & 0 \\ 0 & 0 & \frac{\mathrm{i}}{2} & 0 & 0 & 0 & 0 \\ 0 & 0 & 0 & -\frac{\mathrm{i}}{2} & 0 & 0 & 0 \\ 0 & 0 & 0 & 0 & 0 & 0 & 0 \\ 0 & 0 & 0 & 0 & 0 & 0 & 0 \\ 0 & 0 & 0 & 0 & 0 & 0 & 0 \end{bmatrix} \quad \text{and} \tag{4.114}$$

$$\mathbf{g} = \begin{bmatrix} 0 \\ -q_5 q_2 + q_1 q_7 - q_1^3 + \frac{1}{2}(q_3^2 + q_4^2) \\ \frac{1}{2}\mathrm{i}\, q_3 q_6 \\ -\frac{1}{2}\mathrm{i} q_4 q_6 \\ 0 \\ 0 \\ 0 \end{bmatrix}. \tag{4.115}$$

If Eqn. (4.113) is brought in JORDAN form, the normal form transformation can be conducted. Finally, the simplified equation

$$\dot{\mathbf{y}} = \mathbf{h}(\mathbf{y}) = \mathbf{\Lambda}\mathbf{y}(t) + \mathbf{H}\mathbf{y}_2 + \mathbf{H}\mathbf{y}_3 + \cdots \tag{4.116}$$

is obtained. In this case the transformation was carried out up to order 8. An *ansatz* can be made to solve Eqn. (4.116). Thereby, it is convenient to go into polar coordinates by

$$y_1(t) = \frac{1}{2} r e^{\mathrm{i}\left(\varphi + \Omega \mathrm{t}\right)}, \tag{4.117a}$$

$$y_2(t) = \frac{1}{2} r e^{-\mathrm{i}\left(\varphi + \Omega \mathrm{t}\right)}, \tag{4.117b}$$

which leads to differential equations for the phase and the amplitude

$$\dot{r} = -\frac{1}{2}\mu r + \frac{1}{2}\hat{e}\cos\varphi + \frac{3}{16}\hat{e}\left(\alpha\cos\varphi + \mu\sin\varphi\right) + \cdots, \tag{4.118a}$$

$$\dot{\varphi} r = r(1-\Omega) - \frac{1}{2}\hat{e}\sin\varphi + \frac{3}{16}\hat{e}\left(\mu\cos\varphi - \alpha\sin\varphi\right) + \cdots, \tag{4.118b}$$

which are not a functions of time explicitly. Figure 4.7 illustrates these coupled differential equations. The fixed points are shown by the two small circles. Both points represent a stable solution and both of them are os-

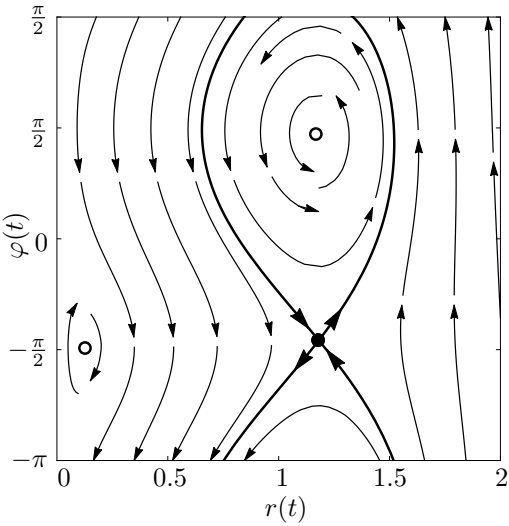

Figure 4.7: $r - \varphi$ phase plane with $\mu = 0.05, \Omega = 1.5, \hat{e} = 0.15\,\Omega^2$, $\alpha = 1$ and $\beta = 1$.

cillations about the unstable equilibrium. The lower left fixed point might represent an excitation-induced stable oscillation as analyzed by Wu, Harne and Wang [131]. The upper right fixed point represents inter-well oscillations. The stable equilibrium for the chosen parameters is about $r_s = 1$. Thus, the upper right fixed point indicates vibrations with amplitudes that go beyond the equilibria. The black dot indicates the saddle point.

Usually, the unstable manifold of a saddle point restricts the different domains of attraction. Nevertheless, from the unstable manifold shown in Fig. 4.7, no auxiliary assertion concerning the domains of attraction can be made. This is justified by the characteristics of the normal form transformation: only the essential characteristics are preserved, whereas the transformation neglects other features. In this case, the transformation does neither consider single-well oscillations nor cross-well oscillations. Thus, the transformation only allows to split the phase plane for the two mentioned oscillation types, which does not represents to full solution space of the underlying equa-

tion. This results in a poor estimation of the domain of attraction. Figure 4.8 shows an estimated domain of attraction. According to the estimation, every initial condition outside the bounded domain leads to inter-well oscillations. Only the inner part of the domain is shown by the red line because later intersections occur between the borders. This is due to the approximated normal form. The normal form was developed for a monostable system, thus the present case is too far from the expansion point. This leads to an increased error for the approximation. With this example the limitations of the developed transformation are perceived. Possible improvements can be made

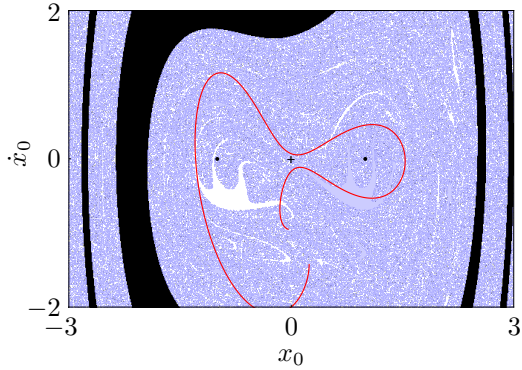

Figure 4.8: Analytically determinded domain of attraction ($\hat{e} = 0.1, \Omega = \sqrt{2}, \mu = 0.05$, $\alpha = 1, \beta = 1$)

by choosing another expansion point. However, this might be difficult due to occurring resonating terms in the transformation. Nevertheless, the normal form transformation allows to prove the existence of inter-well oscillations and allows to show the main features of this kind of oscillation (φ and r), which cannot be done so demonstrative with any other method.

The representation in polar coordinates can be used to compute the inter-well orbit. While the polar representation (Eqn. 4.118) includes only terms with the frequency Ω, in the initial coordinates p contain terms with higher harmonics. The resulting description in p coordinates is shown in Fig. 4.9. Within the graph the gray orbit represents the result from the normal form theory and the black orbit shows a numerically calculated orbit. Both orbits mainly correlate, despite some deviations. This is justified by the developed order of the normal form theory and its approximative character such as the

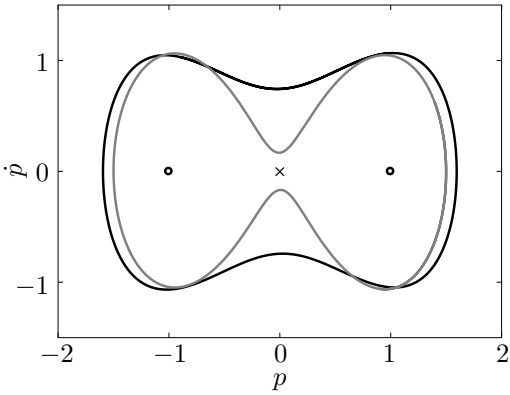

Figure 4.9: Numerically obtained orbit (black) and the analytically determined orbit (gray) for $\mu = 0.05, \Omega = 0.7$, $\hat{e} = 0.15\,\Omega^2, \alpha = 1$ and $\beta = 1$.

chosen development point of the normal from transformation.

4.7. Empiric criteria

In contrast to the analytical bifurcation values, a transformation can be exploited in order to describe the solution's topology of the bistable DUFFING equation. Considering the nondimensionalized and reduced DUFFING equation (3.26) it is apparent that the effect of the stiffness parameters can be eliminated by an appropriate transformation. With this transformation the solution of the bistable DUFFING equation is invariant to the stiffness parameters and only dependent on the damping and the excitation. This implies that the previously derived bifurcation values are only dependent on the damping, if an appropriate transformation to the equation is applied. Consequently, the concept of a generic solution can be introduced. This concept can be used to limit oscillation type domains which can not be limited by analytic bifurcation values or only roughly. Figure 4.10 shows the response map for the snap-through ratio Ψ of the reduced bistable DUFFING equation (3.26). With the transformation (3.28) this topology is invariant, thus a empiric criterion will be derived for limiting the right diffuse boundary of the inter-well domain. This boundary results from transitions of chaotic to periodic inter-well oscillations. This transition is very sensitive to initial conditions. Thus, there

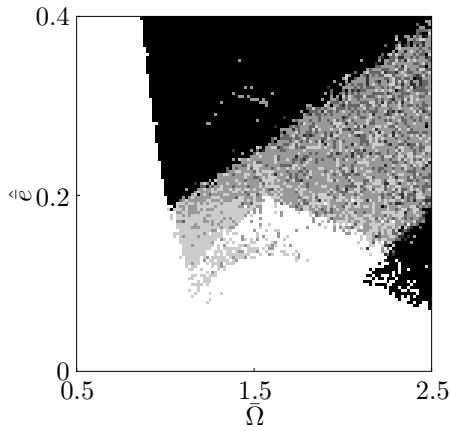

Figure 4.10: Response map for Ψ for the reduced equation (3.26).

is no predefined underlying bifurcation value. However, since the characterization of the inter-well domain in Fig. 4.10 is of great use for bistable energy harvesters, a more precise description is desirable. This can be achieved by exploiting the invariance property that can be used to define a generic solution of the bistable DUFFING oscillator. As shown in Fig. 4.10, the diffuse right edge is an almost linear function in the frequency Ω. This edge can be interpolated by a linear function

$$\bar{e}(\Omega, \mu) = a(\mu) + b(\mu)\ \Omega \tag{4.119}$$

for different damping rations by using the reduced and transformed DUFFING equation (3.29). In this case the lowest amplitude $\hat{e}$ for which $\Psi = 1$ was taken for the interpolation. This was done for all frequencies of the right boundary. Figure 4.11 shows the results for the functions $a(\mu)$ and $b(\mu)$. The dots indicate individual numerical simulations. The graphs show that the offset $a(\mu)$ is mainly affected by the damping μ. The slope $b(\mu)$ of the diffuse edge is almost constant within the shown parameter range. For μ higher than 0.2, the diffuse egde can not be described by a linear function anymore. The solid black line indicates an interpolation of the numerical data. These

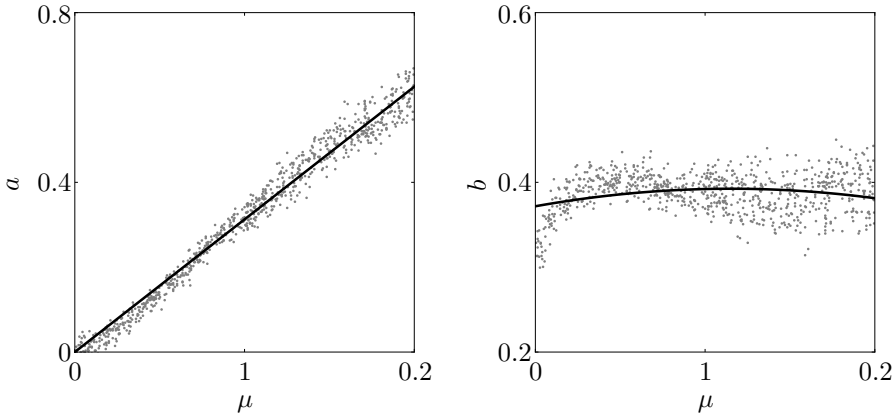

(a) $a(\mu)$ **(b)** $b(\mu)$

Figure 4.11.: Numerical results for the functions $a(\mu)$ and $b(\mu)$ with their interpolation: The gray dots indicate numerical results and the black curves the corresponding interpolation

interpolations are given by

$$a(\mu) = c_0 + c_1\mu, \tag{4.120a}$$

$$b(\mu) = c_2 + c_3(\mu - c_4)^2, \tag{4.120b}$$

with the parameters given in Table 4.1.

Parameter	Value
c_0	$13.78 \cdot 10^{-6}$
c_1	3.12
c_2	-1.56
c_3	0.24
c_4	0.2

Table 4.1: Coefficients for the interpolation functions $a(\mu)$ and $b(\mu)$

5. Analysis of nonlinear energy harvester designs

This chapter provides an analysis of the different structures modelled in Chapter 3. With these investigations this chapter performs a key role in the aim of this thesis. To this end, numerical simulations are performed to characterize the solution's topologies of the different structures. The numerical simulations allows to investigate the energy harvesting capabilities of the different structures. Moreover, the numerical results are compared to the analytic and empiric criteria obtained from the methods presented in Chapter 4. Finally, a short analysis of the considered structures with combined harmonic and noise excitation gives an outlook towards real-world applicability.

5.1. Bistable system

The introductory Chapter 2 presented the different features of multistable structures, e.g. different oscillation types and domains of attraction. These features are described by means of the bistable DUFFING oscillator. Thanks to the simple shape of the equation of the bistable oscillator (Eqn. 2.1), even though the response of such an oscillator cannot be defined as simple, profound investigations can be performed analytically. This is not always possible for nonlinear energy harvesters that are described by more than one differential equation. Hence this section investigates the bistable DUFFING oscillator with the focus on energy harvesting. This is amongst others done by performing a parameter study and a comparison between numerical solutions and the criteria presented in Chapter 4. As it is shown in later sections, many results and observations can be transferred to other structures.

5.1.1. Measure for the harvesting capability

The fully coupled equations need to be considered to account for the harvested energy. However, as will be shown later, the DUFFING oscillator can be used to approximate an electromechanically coupled system. This has the advantage that more and easier analytic criteria can be applied to describe the bifurcation behavior. As shown in Chapter 4, most of the analytic criteria can be stated in closed-form for the DUFFING oscillator, while mainly numerical solutions of the bifurcation conditions are possible for systems with more degrees of freedom. For these reasons it is practical to consider the uncoupled equation (2.1) first.

For investigating the energy harvesting capabilities, a measure for the dissipated energy is introduced. The dissipated energy within an electromechanical system can be divided into energy which is dissipated mechanically due to friction or material damping and energy dissipated within the electrical circuit. The second one corresponds to the harvested energy. In reality, there will also be some electrical losses due to the circuit design. To account for the energy harvest potential, even though the considered structure is purely mechanical, it is convenient to introduce the normalized power [43]

$$P_n = \frac{1}{\Omega^2 \hat{e}(t_2 - t_1)} \int_{t_1}^{t_2} \mu \, \dot{x}^2(t) \mathrm{d}t, \tag{5.1}$$

where

$$t_2 - t_1 = n \, \frac{2\pi}{\Omega}. \tag{5.2}$$

The dissipated power is normalized by the excitation amplitude to compensate for the excitation. Therefore, the normalized power does not have the unit of a power. The parameter n needs to be large enough for P_n to converge, especially for cross-well oscillations. Thus, the value P_n gives a measure for the mean power dissipated due to damping. Figure 5.1 gives a comparison between the snap-through ratio Ψ (Eqn. 2.5) and the normalized power P_n. Note that the values within the response map are normalized by $\max P_n$ referring to the maximal value of P_n within the map in order to use the same legend. The inter-well domain ($\Psi = 1$) can easily be identified as a domain for

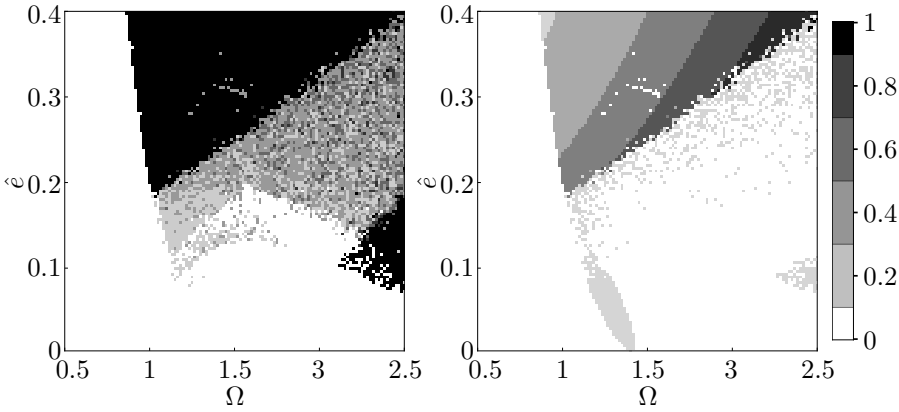

(a) Snap-through ratio Ψ **(b)** Normalized Energy $P_n/\max P_n$

Figure 5.1.: Response maps for $\alpha = 1, \beta = 1$ and $\mu = 0.05$ ($x_0 = x_s, \dot{x}_0 = 0$)

optimal energy harvesting. The large amplitudes of the inter-well oscillations lead to a highly increased dissipation. This reveals the advantage of using bistable structures for the design of energy harvesters. Figure 5.1b shows that for low excitation amplitudes the highest power can be harvested near the resonance frequency $\omega = \sqrt{2\alpha}$. This feature is exploited by linear energy harvesters. The exploitation of subharmonic responses does not contribute significantly to the harvested energy: even though inter-well oscillations are obtained (Fig. 5.1a lower right side), the dissipated energy is small. This is justified by the fact that the response is in a subharmonic of the excitation frequency Ω. Thus, the dissipated power is much lower in this domain. Figure 5.2 depicts the dissipated energy in logarithmic scale. This allows to see the difference between the harvested energy of single-well and cross-well oscillations. Cross-well oscillations show a significant increase in the dissipated energy compared to single-well oscillations. However, both oscillation types lead to much less harvested power compared to inter-well oscillations. This is justified by the occurring lower amplitudes for these oscillation types. This can be illustrated by considering the mean amplitude $\bar{a}$ of a time signal.

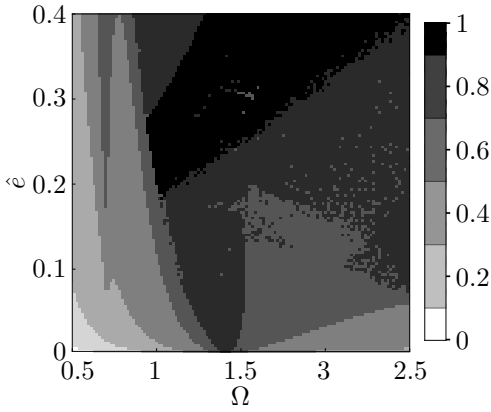

Figure 5.2: Normalized Energy $\log(P_n)/\max(\log P_n))$

The mean amplitude $\bar{a}$ is defined by

$$\bar{a} = \frac{1}{n-i} \sum_{i}^{n} (a_i - a_{i+1}) \,, \tag{5.3}$$

where the parameters a_i are the amplitudes for the extrema as illustrated in Fig. 2.7. Figure 5.3 shows a response map for the parameter $\bar{a}$. As expected, the mean amplitude roughly reflects the results of the normalized power P_n. The mean amplitude increases for higher forcing amplitudes $\hat{e}\,\Omega^2$, which also corresponds to the findings for P_n.

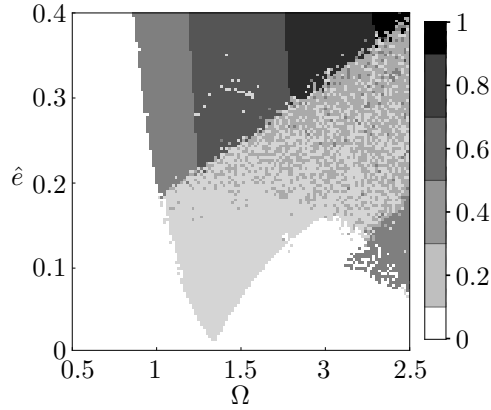

Figure 5.3: Response map for the mean amplitude $\bar{a}/\max \bar{a}$

5.1.2. Parameter study

This section analyzes the influence of the different parameters of the DUFFING equation. The previous section concerns the superior potential of inter-well oscillations for harvesting energy. Thus, the influence of different parameters on the inter-well domain are analyzed primarily.

Influence of the damping

The damping parameter is the only non-conservative term within the system. The lower the term μ is, the easier it is to obtain the desired inter-well oscillations. This is illustrated in Fig. 5.4. An increased damping μ prevents the system to snap through. Hence the inter-well domain is obtained for higher amplitudes $\hat{e}$. Similarly. low damping parameters allow to obtain inter-well oscillations for smaller amplitudes $\hat{e}$.

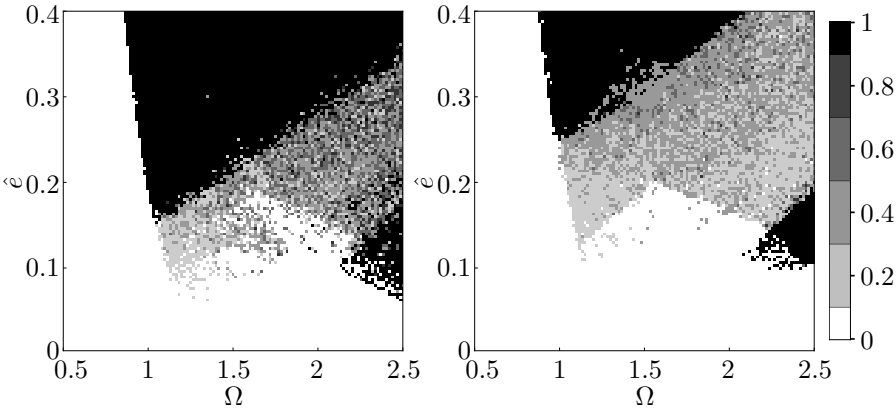

(a) $\mu = 0.025$ **(b)** $\mu = 0.1$

Figure 5.4.: Response maps for the snap-through ratio Ψ $(\alpha = 1, \beta = 1)$ $(x_0 = x_s, \dot{x}_0 = 0)$

Influence of the stiffness parameters

In this section the influence of the stiffness parameters α and β is analyzed. Section 3.1.4 showed that the influence of the stiffness parameters α and β can be eliminated by an appropriate transformation. Nevertheless, both parameters play a major role in a non-transformed equation of motion. The linear stiffness α defines the eigenfrequency as in any other linear system. Figure 5.5 depicts response maps of Ψ for different values of α. Not only the eigenfrequency is shifted to higher frequencies but also the inter-well domain is shifted to higher excitation amplitudes $\hat{e}$ when α is increased. This is caused by the raised stable equilibria $x_s = \pm\sqrt{\frac{\alpha}{\beta}}$. In contrast, an increased cubic stiffness parameter β lowers the stable equilibria, which results in inter-well oscillations that can be obtained for even lower excitation amplitudes $\hat{e}$. Figure 5.6 illustrates this characteristic. The analysis of α reveals a possible design strategy for DUFFING-like energy harvesters: the linear stiffness α should be designed according to a dominating frequency of the host structure, whereas the selection of β should be based on the excitation amplitude. One goal for the design of β is to obtain inter-well oscillations with a sufficient

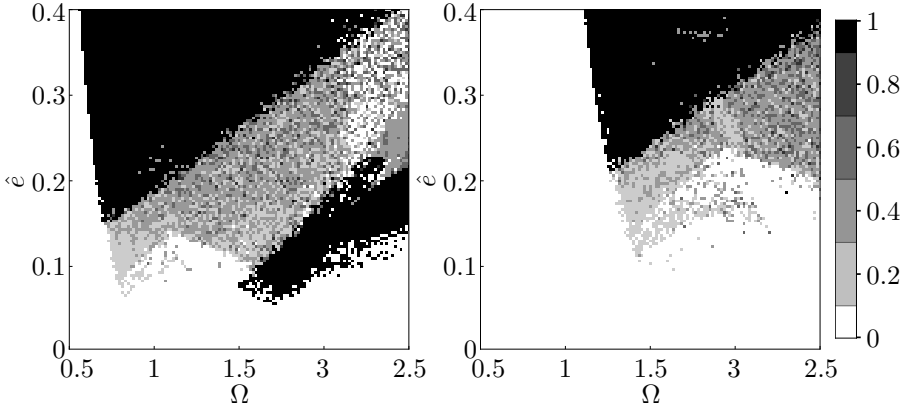

(a) $\alpha = 0.5$ **(b)** $\alpha = 1.5$

Figure 5.5.: Response maps for Ψ with $\beta = 1$ and $\mu = 0.05$, $(x_0 = x_s, \dot{x}_0 = 0)$

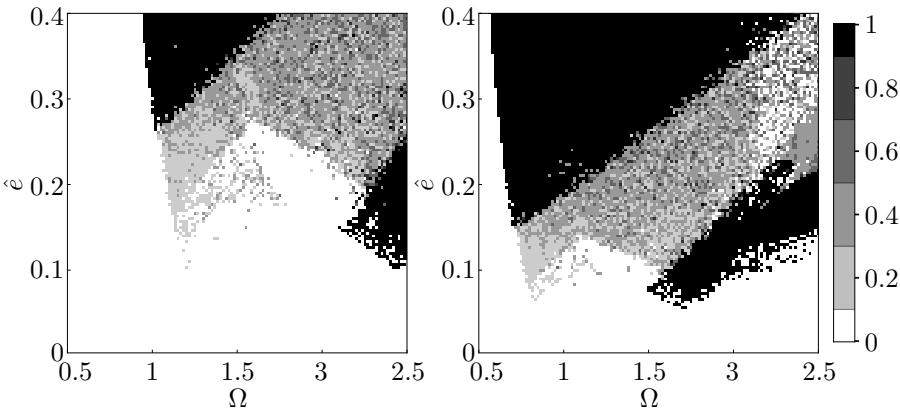

(a) $\beta = 0.5$ **(b)** $\beta = 1.5$

Figure 5.6.: Response maps for Ψ ($\alpha = 1, \mu = 0.05$ and $x_0 = x_s$, $\dot{x}_0 = 0$)

bandwidth. This suggest that β should be high. On the other hand, β should be optimized for an increased energy harvest which, according to Fig. 5.1b, suggests to operate the energy harvester near the lower edge of the inter-well domain. There is, thus, a conflict of aims in the design of β.

Asymmetric potential design

Up to this point, only symmetric potentials have been considered. This resulted in systems with symmetric equilibria and equal eigenfrequencies. In the following an asymmetric potential is investigated concerning the capabilities for extending the bandwidth. The effect of asymmetry will be analyzed by means of a modified equation

$$\ddot{x}(t) + \mu\dot{x}(t) - \alpha x(t) + \gamma x^2(t) + \beta x^3(t) = \hat{e}\ \ddot{e}(t). \tag{5.4}$$

The unstable equilibrium $x_u = 0$ is not affected by the introduced asymmetry parameter γ. The stable equilibria read

$$x_{1s} = \frac{-\gamma + \rho}{2\beta}, \qquad x_{2s} = \frac{-\gamma - \rho}{2\beta}, \tag{5.5}$$

with the corresponding eigenfrequencies

$$\omega_1 = \sqrt{\frac{\gamma(\gamma-\rho)+4\alpha\beta}{2\beta}}, \qquad \omega_2 = \sqrt{\frac{\gamma(\gamma+\rho)+4\alpha\beta}{2\beta}}, \tag{5.6}$$

and

$$\rho = \sqrt{4\alpha\beta+\gamma^2}.$$

For the equilibria and eigenfrequencies the conditions

$$\omega_1 < \omega_2 \quad \text{and} \quad |x_{1s}| < |x_{2s}|$$

hold. The asymmetry parameter γ splits the stable equilibria and eigenfrequencies. This can be seen by Eqn. (5.6). The asymmetry parameter $\gamma = 0$ results in $\omega_1 = \omega_2$. Figure 5.7 illustrates this correlation by means of response maps for the snap-through ratio Ψ. For the initial condition starting in the

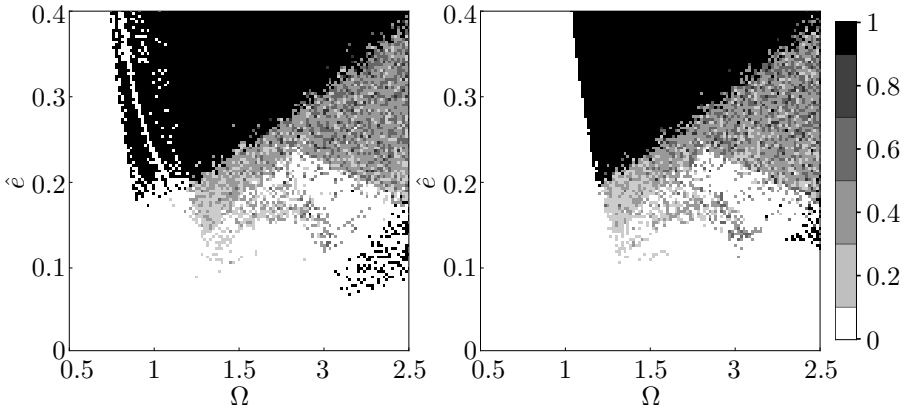

(a) $x_0 = x_{1s}$ **(b)** $x_0 = x_{2s}$

Figure 5.7.: Response maps for Ψ for different initial conditions with $\dot{x}_0 = 0$ ($\alpha = 1, \beta = 1, \gamma = 0.5, \mu = 0.05$)

upper potential well x_{1s} (Fig. 5.7a) the influence of the two different eigenfrequencies can be identified. The left edge of the inter-well domain is limited by

two sharp boundaries. At lower excitation frequencies a first boundary can be identified. This boundary gives the left border of a diffuse inter-well domain. It emerges from the eigenfrequency ω_1 for low excitation amplitudes. The second edge limits the diffuse from the continuous inter-well domain. This boundary emerges emerges from the upper frequency ω_2. The diffuse band between both boundaries results from the split eigenfrequencies. For excitation parameters within this domain, either inter-well oscillations or single-well oscillations are observed. Single-well oscillations occur when the solution $x(t)$ is trapped by the lower potential well of x_{2s}. Once the solution is captured by this well, it can only escape when enough energy can be gathered from the excitation source. This happens near ω_2. Hence the continuous inter-well domain emerges from ω_2 at low excitation amplitudes $\hat{e}$. For solutions which start within the lower potential well (Fig. 5.7b), a sharp left boundary between single-well and inter-well oscillations can be found. This characteristic is similar to the symmetric DUFFING oscillator. Once the solution escapes the lower potential well, enough energy is inherent to the system so that it cannot be trapped by the upper potential well anymore. For this reason, no diffuse inter-well domain can be observed for this specific initial condition.

These observations on a asymmetric potential permit to draw conclusions for bistable energy harvesters. The splitting of the eigenfrequencies does not enhance the broadband capabilities for energy harvesting. This is due to the fact that the bandwidth is not widened by the two different eigenfrequencies. Moreover, the position of the inter-well domain is a matter of probability, as it depends on the initial condition of $x(t)$. Depending on the initial condition, different excitation frequencies Ω are preferable for the escape out of the potential well. Thus, the two different eigenfrequencies cannot be exploited in order to take advantage for the enhancement of the broad bandwidth capabilities for this kind of energy harvesters. This was also concluded by BETTS et al. for the composite plate [17].

5.1.3. Comparison to analytic criteria

This section presents a comparison between numerical results and the criteria developed in Chapter 4. This shows how well the analytic and empiric values can be exploited to characterize the solution's topology. Figure 5.8 shows a comparison between the topology for the DUFFING equation and some analytic criteria introduced in Chapter 4. The upper (blue) saddle-node bifurcation

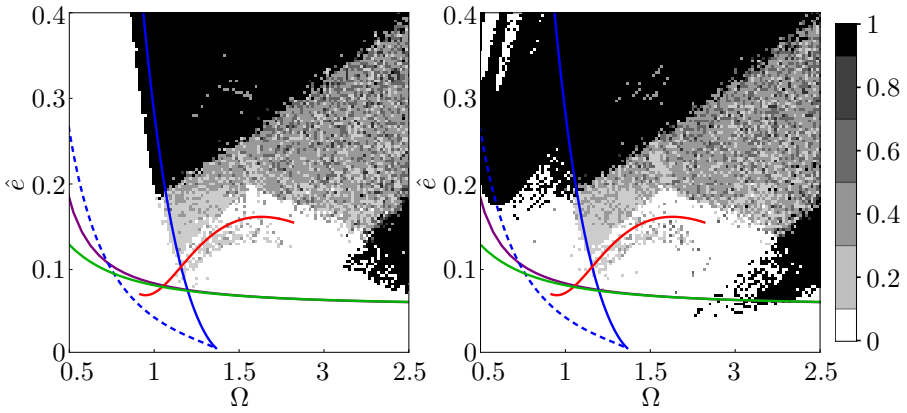

(a) $x_0 = x_s$ **(b)** $x_0 = 0$

Figure 5.8.: Response map for Ψ and some analytic criteria: lower b_{snL} (dashed blue), upper b_{snU} (blue) and b_{snI} (green) saddle-node bifurcations, MELNIKOV function (purple) and criterion for chaos (red).

b_{snU} obtained by the multiple scales method limits the sharp left boundary of the inter-well domain very well. This is explained by the fact that at this bifurcation value the lower non-resonant saddle (S_n) of the single-well oscillations looses stability. Thus, the solution jumps on the next stable saddle which is the branch of inter-well oscillations (S_I). If the initial condition is changed (Fig. 5.8b), the solution is able to follow the inter-well saddle S_I for an even smaller excitation amplitude $\hat{e}\ \Omega^2$. The small deviation between the numerical simulation and the analytic criteria is justified by the approximative character of the multiple scales method, which also neglects higher nonlinear terms. The lower saddle-node bifurcation b_{snL} is shown by the dashed blue

line, but it has no practical relevance, since inter-well oscillations emerge from the bifurcation b_{snI}. The saddle-node bifurcation b_{snI} of the inter-well oscillations (green) and the criterion derived by the MELNIKOV function (purple) provide a lower limit for the inter-well domain. The derivation of both values is completely different, but both provide a necessary condition for inter-well oscillations. Thus, the results are very similar. Both criteria do not consider initial conditions. For this reason, there is a large deviation between the predicted and the observed inter-well domain. The criterion for chaos (red) gives the right boundary for the minimal excitation parameters necessary to obtain period-doubling bifurcations. The left boundary is given by the upper saddle-node bifurcation [111]. According to Fig. 5.8, this criterion limits the right side of the inter-well domain in the best way. It has to be pointed out that the shown inter-well domain in Fig. 5.8a provides a conservative estimate of the domain. For any other initial condition $x_0 \neq x_s$, the domain is increased. This can be explained by the fact that for this initial condition the lowest energy is introduced initially. Any other initial condition introduced initial potential or initial kinetic energy.

In contrast to the analytical bifurcation values, the empiric criterion derived in Section 4.7 can be exploited to describe the solution's topology. This solution is shown in Fig. 5.9 by the pink line. The graph illustrates that the empiric value is able to describe the right diffuse edge. Consequently, it can be used to get a conservative estimate for the right edge of the inter-well domain when the system parameters are known. Thereby, the upper saddle-node bifurcation b_{snU} limits the left sharp edge of the domain.

To conclude, the comparison shows that different criteria can be exploited to design bistable energy harvesters with a single degree of freedom. Hereby, the influence of the electromechanical coupling can be included into the single equation using Eqns. (4.26) and (4.27). The quality of this reduction is shown in the next section. On the one hand, the derived criteria provide a powerful tool to determine optimal system parameters if the excitation source is known. On the other hand, they can be employed to describe the main characteristics of a bistable oscillator when the system parameters are known.

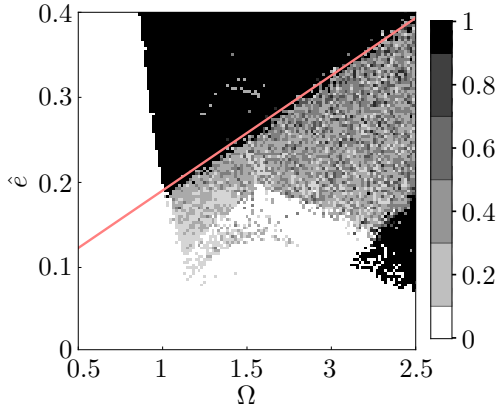

Figure 5.9: Response map for Ψ with the empiric criterion

5.2. Bistable electromechanical system

In Section 3.2 the model of a simple bistable electromechanical system is derived. The model is given by the electromechanically coupled equations

$$\ddot{x}(t) + \mu\ \dot{x}(t) - \delta\ v(t) - \alpha\ x(t) + \beta\ x^3(t) = \hat{e}\ \ddot{e}(t), \tag{5.7a}$$

$$\phi\ v(t) + \eta\ \dot{x}(t) + \dot{v}(t) = 0. \tag{5.7b}$$

This model does not only describe the electromechanical beam, but also other bistable structures with an electromechanical transducer. In the following, some characteristics of such a system will be investigated.

5.2.1. Optimal electrical resistance

The optimal resistance for an electromechanical bistable beam is investigated in this section. This parameter is defined by the value at which the harvested power exhibits a maximum. For this study it is assumed that the harvested energy is dissipated by an electrical resistance. This will give some insight on the occurring energy harvest of an electromechanical system. Stanton and Owens [110] already observed that the optimal resistance which allows to maximize the power output varies for each occurring oscillation type. This optimal resistance differs from the one of linear energy harvesters.

For the analysis the harmonic balance method is applied. Hence the *ansatz*

$$x(t) = A_0 + A_1 \cos(\Omega t) + A_2 \sin(\Omega t), \tag{5.8a}$$

$$v(t) = B_1 \cos(\Omega t) + B_2 \sin(\Omega t), \tag{5.8b}$$

is inserted into Eqn. (5.7) to obtain analytic expressions for the steady-state solution. Balancing the constant and the first harmonic terms, the amplitudes for the deflection and voltage

$$\hat{a} = \sqrt{A_1^2 + A_2^2}, \tag{5.9a}$$

$$\hat{v} = \sqrt{B_1^2 + B_2^2}, \tag{5.9b}$$

can be determined. The mean power follows with

$$P_m = \frac{1}{2}\hat{v}^2\phi. \tag{5.10}$$

Figure 5.10 shows the relation between the amplitude $\hat{a}$ and the mean harvested power P_m with the parameters stated in Table 5.1. These parameters

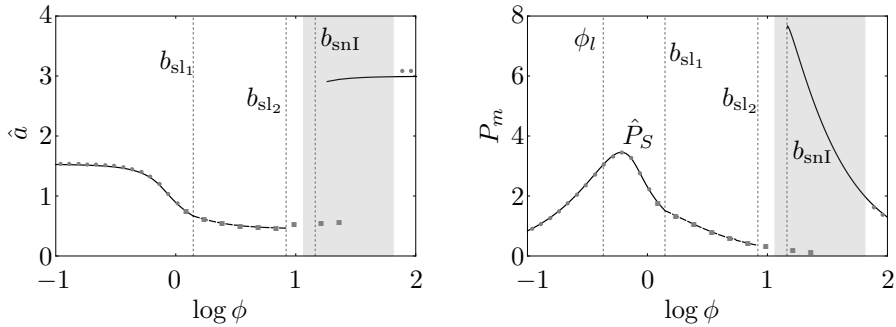

(a) Amplitude $\hat{a}$ **(b)** Mean Power $P_m \cdot 10^5$

Figure 5.10.: Bifurcation diagrams for $\Omega = 2, \hat{f} = 0.5\ x_s$. The black solid (dashed) result from the harmonic balance method for inter-well (single-well) oscillations. The gray dots (squares) indicate numerically inter-well (single-well) oscillations. The gray shaded domain indicates the area, where cross-well oscillations are found numerically.

Table 5.1: Physically reasonable parameters for the reduced electromechanical system

Parameter	Value
α	$\frac{1}{2}$
β	$\frac{3}{4}$
δ	$5 \cdot 10^{-3}$
μ	$5 \cdot 10^{-3}$
η	850

result from a physical reference system which is transformed according to Eqn. (3.57). Note that the electrical conductance is shown on the horizontal axis. The conductance is the inverse of the electrical resistance. Since clarity is ensured in this context by the chosen symbol ϕ, and the fixed relation between conductance and resistance, the terms are used as synonyms in this context. The black lines in the graphs show the results of the harmonic balance method, while the gray dots represent numerical results. The results show that both single-well and inter-well oscillations exhibit different optimal resistance at which the power output reaches a maximum. These resistances deviate strongly compared to the ones calculated for a linear system. The optimal conductance of a linear energy harvester is given by

$$\phi_l = \Omega \sqrt{\frac{\Omega^2 \left(\mu^2 - 2(\alpha + \delta\eta)\right) + (\alpha + \delta\eta)^2 + \Omega^4}{\alpha^2 - 2\alpha\Omega^2 + \Omega^2 \left(\mu^2 + \Omega^2\right)}}. \tag{5.11}$$

This value is obtained by linearizing Eqn. (5.7) for a positive linear term and solving for the extrema in the power by a simple harmonic *ansatz*. This optimal conductance is illustrated in Fig. 5.10b. Within Fig. 5.10a and 5.10b the two bifurcation values b_{sl} (stability loss, determined by FLOQUET theory) and b_{snI} (saddle-node bifurcation) are indicated by the vertical gray dashed lines. Both bifurcation values can also be observed by numerical simulation: for a small parameter ϕ only inter-well oscillations are stable due to the large electrical damping. When the electrical damping is decreased for higher values of ϕ, single-well oscillations become stable. This occurs at the bifurcation value b_{sl_1}. The single-well oscillations loose again stability at the bifurcation value b_{sl_2}. For even lower electrical damping parameters inter-well oscillations

emerge from the bifurcation b_{snI}, whereas the amplitude is significantly higher. This is also reflected in the theoretical harvested power which is predicted analytically. The numerical solution follows this branch only for higher values of ϕ. This is justified by the influence of the initial conditions. As the excitation

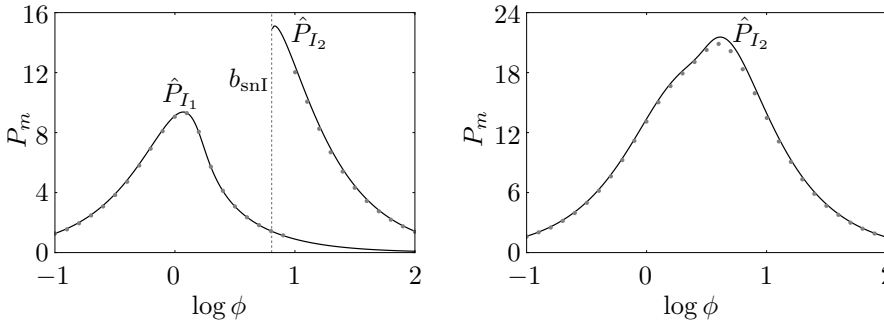

(a) Mean Power $P_m \cdot 10^5$ for $\hat{f} = 1x_s$ **(b)** Mean Power $P_m \cdot 10^5$ for $\hat{f} = 1.5x_s$

Figure 5.11.: Bifurcation diagrams for $\Omega = 2$. The black solid (dashed) line results from the harmonic balance method for inter-well (single-well) oscillations. The gray dots indicate numerical simulation.

increases (Fig. 5.11a), the single-well and cross-well solutions vanish while the inter-well solutions remain. Two peaks ($\hat{P}_{I_1}$ and $\hat{P}_{I_2}$) in the mean harvested harvested power can be identified. For an even more increased excitation amplitude (Fig. 5.11b) both peaks coincide and only one peak remains. Figure 5.11 reveals that the optimal conductance ϕ for the peak $\hat{P}_{I_2}$ theoretically shows the maximal harvested power, but this might not be observed numerically or experimentally due to the initial conditions which need to be met for harvesting along this solution branch. For this reason, no unique parameter ϕ_{opt} can be stated. This is even clearer when looking at the dependency of the power peaks ($\hat{P}_S$, $\hat{P}_{I_1}$ and $\hat{P}_{I_2}$) on the excitation parameters $\hat{e}$ and Ω. Figure 5.12 shows the influence of the excitation parameters on the different power peaks . The graphs show a high sensitivity of the optimal conductance, especially for low excitation parameters.

If the harvesting is performed at high excitation amplitudes $\hat{e}$ the optimal conductance ϕ is less sensitive. Additionally, the optimal conductance varies

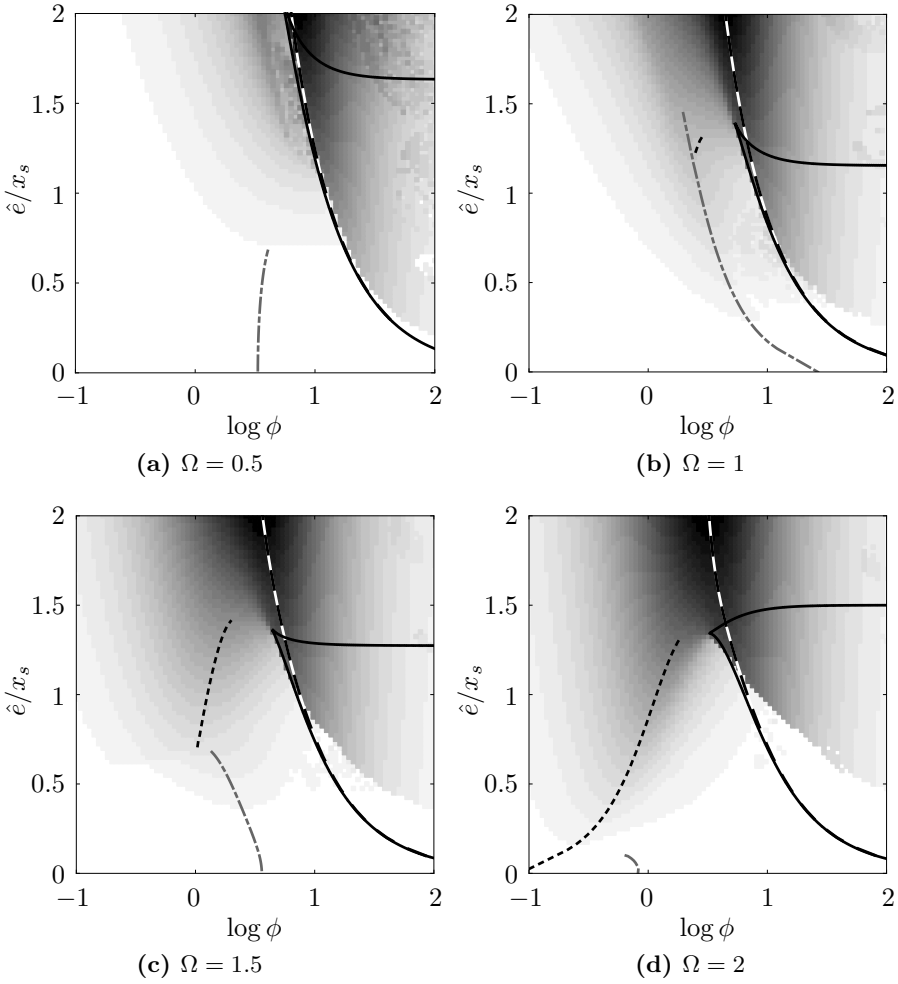

(a) $\Omega = 0.5$ **(b)** $\Omega = 1$

(c) $\Omega = 1.5$ **(d)** $\Omega = 2$

Figure 5.12.: Response maps showing the mean power $P_m / \max P_m$. The gray dashed-dotted line indicates the analytically obtained $\hat{P}_S$. The black dashed (black-white dashed) line indicates the peak value for $\hat{P}_{I_1}(\hat{P}_{I_2})$ and the black solid line the saddle-node bifurcation b_{snI}.

largely for the different solution types. For this reason, an accurate knowledge of the excitation parameters are necessary for a correct design of the electrical circuit. The harmonic balance method does not permit to formulate a closed-form expression for the optimal conductance ϕ_{opt}. However, as illustrated in Fig. 5.12, the peak $\hat{P}_{I_2}$ proceeds closely along the b_{snI} border. Thereby, the bifurcation condition is given by

$$\begin{aligned} &64(\kappa\phi+\lambda\mu)^2\Big(\alpha^2\lambda+2\alpha\nu\Omega^2+\Omega^2\Big(\kappa^2+2\kappa\left(\mu\phi-\Omega^2\right)+\lambda\left(\mu^2+\Omega^2\right)\Big)\Big)^2 \\ &\quad+243\beta^2\hat{e}^4\lambda^4\Omega^2-48\beta\hat{e}^2\lambda\left(\alpha\lambda+\nu\Omega^2\right)\Big(\alpha^2\lambda^2+2\alpha\lambda\nu\Omega^2 \\ &\quad+\Omega^2\Big(\kappa^2\left(\Omega^2+9\phi^2\right)+2\kappa\lambda\left(9\mu\phi-\Omega^2\right)+\lambda^2\left(9\mu^2+\Omega^2\right)\Big)\Big)=0, \end{aligned} \tag{5.12}$$

with

$$\begin{aligned} \lambda &= \phi^2+\Omega^2, \\ \kappa &= \delta\eta, \\ \nu &= \kappa-\lambda. \end{aligned}$$

This bifurcation condition is derived by the harmonic balance method (see Chapter 4). Consequently, this bifurcation condition can be used for the estimation of $\hat{P}_{I_2}$. No simple analytic expression can be stated for the peaks $\hat{P}_S$ and $\hat{P}_{I_1}$. Considering Eqn. (5.12) it is clear that ϕ_{opt} also depends on the damping μ and the coupling parameters δ and η. However, their influence will not be analyzed.

Finally, the results can be compared with the findings of the perturbation calculus in Section 4.1.1. The introduced damping by the electrical circuit is given by (4.27)

$$\mu_e = \frac{\delta\eta\phi}{\omega^2+\phi^2}. \tag{5.13}$$

Figure 5.13 shows the electrical damping μ_e over the conductance ϕ. The optimal parameter ϕ_{opt} is found were the damping exhibits a maximum. This

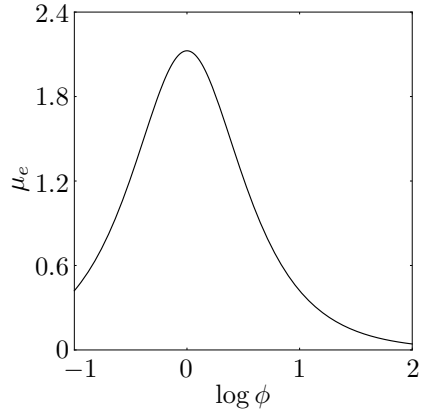

Figure 5.13: Electrical damping μ_e determined by the multiple scales method

leads to

$$\phi_{\text{opt}} = \omega = \sqrt{2\alpha}. \tag{5.14}$$

For ϕ_{opt} the frequency shift ω_e (4.26) is given by

$$\omega_e = \frac{1}{4}\delta\eta. \tag{5.15}$$

For the chosen parameters this leads to

$$\omega_{\text{eff}} = 2.06. \tag{5.16}$$

These results suggest that for excitation frequencies about this effective eigenfrequency ω_{eff} the optimal parameter for ϕ is given by (5.14). Considering $\hat{P}_S$ from Fig. 5.12d, this can be validated: the graph shows a response map for an excitation frequency near ω_{eff}, whereby $\phi_{\text{opt}} \approx \omega$. Consequently, the results from the perturbation can be considered for the description of the optimal ϕ for single-well oscillations as long as the electromechanical system is driven near ω_{eff}. Figure 5.14 shows a response map for ϕ_{opt}. This map was generated by performing an optimization for each excitation parameter set. The different optimal values for ϕ can be identified. The different values also indicate the oscillation type domains. Again, the graphs reveal the sensitive character of ϕ. This needs to be considered in the design of the electrical circuit. One strategy could be to use an adaptive resistance which tries to harvest at the optimal value.

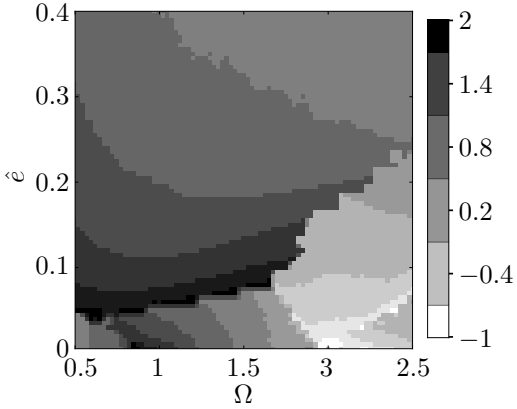

Figure 5.14: Response map for $\log \phi_{\text{opt}}$ with $x_0 = 0, \dot{x}_0 = 0$.

5.2.2. Comparison to analytic criteria

This section concerns a comparison between numerical simulation and the analytical criteria derived in Chapter 4. Thus, the system is not optimized regarding its optimal performance. The comparison will be carried out by means of response maps. Figure 5.15 shows response maps of Ψ and different conductance ϕ. For a lower conductance the inter-well domain is only obtained for higher excitation amplitudes $\hat{e}$. This happens due to the higher introduced electrical damping. The analytical criteria also account for the added damping. For both resistance values, the upper saddle-node bifurcation value b_{snU} limits the left boundary of the inter-well domain in a suitable way. The right edge of the inter-well domain is best limited by the bifurcation value b_{snI} for a high electrical damping and by the criterion for chaos for a lower electrical damping. A reduction for the electromechanically coupled equation was derived in Section 4.1. This transformation can be used to reduce the coupled equations into a single equation. This reduction allows to exploit the analytic and empiric criteria for the DUFFING oscillator. The result is depicted in Fig. 5.16. The graphs show the response maps for Ψ with the analytic and empiric bifurcation criteria. The reduction seems to be suitable because the shown criteria allow to draw useful and reasonable conclusions. This is clearly visible by the empiric description of the right diffuse edge. This criterion limits the diffuse boundary accurately for the reduced system. Thus, the

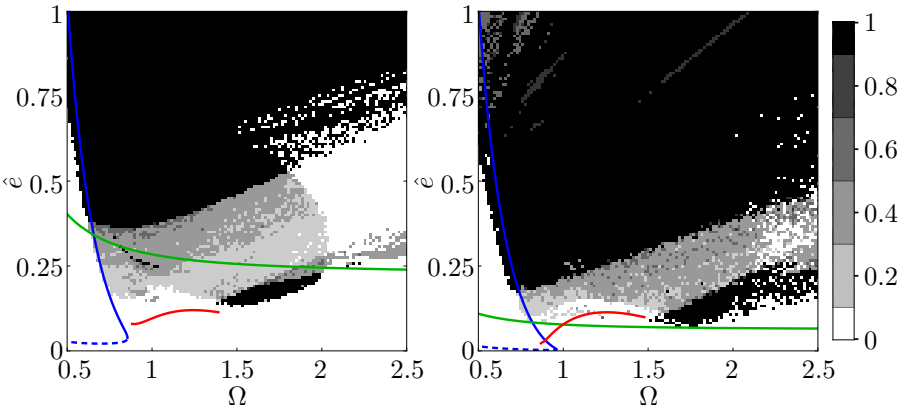

(a) $\phi = 25$ **(b)** $\phi = 100$

Figure 5.15.: Response map for the snap through ratio Ψ and some analytic criteria: lower b_{snL}(blue dashed) and upper (blue) saddle-node b_{snU} bifurcation, (green) saddle-node bifurcation b_{snI} of inter-well oscillations and criterion for chaos (red).

reduction rule gives an appropriate tool to simplify the coupled equations. This is also valid for larger oscillation amplitudes. A comparison between the saddle-node bifurcation values b_{snU} and b_{snI} and the criterion for chaos in Fig. 5.15 and 5.16 reveals that there is no significant difference. This also suggests that the reduction is appropriate for the simplification of the coupled equations.

5.2.3. Optimal domain for energy harvesting

Section 5.1 already shows that inter-well oscillations are the most suitable oscillation type for harvesting energy. This section concerns the optimal range for energy harvesting within the inter-well domain. The domain where the energy should optimally be harvested is limited by two sides in the excitation parameter plane. The lowest values define the point where snap-throughs can be found. These values are given by the left and right boundaries of the inter-well domain. These boundaries can roughly be limited by the analytic

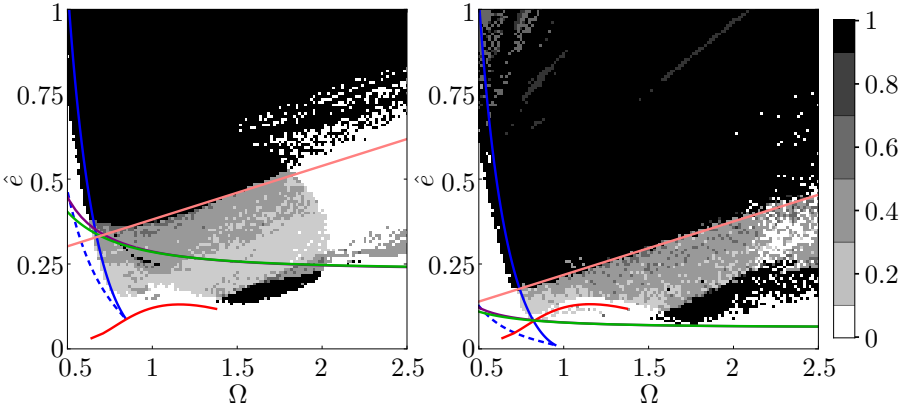

(a) $\phi = 25$ **(b)** $\phi = 100$

Figure 5.16.: Response maps for the snap through ratio Ψ and some analytic criteria for a reduced system: b_{snL} (dashed blue), b_{snU} (blue) and b_{snI} (green) with Melnikov function (purple), criterion for chaos (red) and the empiric criterion for the right diffuse boundary (pink)

and empiric bifurcation values. Harvesting below these boundaries leads to a significant drop in the harvested energy. The upper boundary for the optimal harvest domain is given by the region where the linear term α can be neglected. In this case, the system can be regarded as a monostable system of 4^{th} order. Thus, the benefit of exploiting bistability is not given anymore. To investigate the optimal harvesting domain, the normalized power P_n is introduced which is defined by

$$P_n = \phi \frac{1}{(t_2 - t_1)\,\Omega^2 \hat{e}} \int_{t_1}^{t_2} v^2(t) \mathrm{d}t. \tag{5.17}$$

Here the harvested energy is related to the excitation amplitude. Figure 5.17 illustrates P_n. The graphs show response maps with the normalized power P_n for two electrical resistances. Both graphs show that the normalized power exhibits a significant increase within the inter-well domain. Thus, inter-well oscillations should be exploited to harvest energy in the most efficient way. The optimal region for energy harvesting is near the diffuse boundary. If

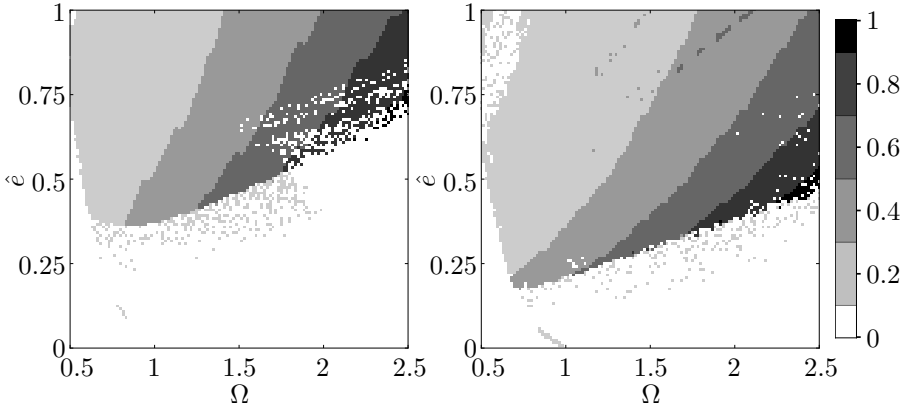

(a) $\phi = 25$ **(b)** $\phi = 100$

Figure 5.17.: Response maps showing the normalized power $P_n / \max P_n$.

the harvesting is performed at a much higher point than this boundary, the normalized energy decreases again. If the harvesting was carried out in this region, an optimization of the energy harvester would allow to increase the performance. This already indicates the necessity of an accurate knowledge of the excitation source to design a bistable energy harvester.

5.3. Composite plate

5.3.1. Principal investigations

In contrast to the model of the bistable beam, the multistable composite plate is described by two coupled differential equations of second order. These equations were derived in Section 3.3. A bistable composite plate also exhibits single-well, cross-well and inter-well oscillations. This can be shown by means of the potential energy. Figure 5.18 shows the double-well potential of the reduced Eqn. (3.91) with the parameters stated in Table 5.2.

The chosen parameters are based on a physically reasonable composite design. Due to the coupling between both degrees of freedom, none of the

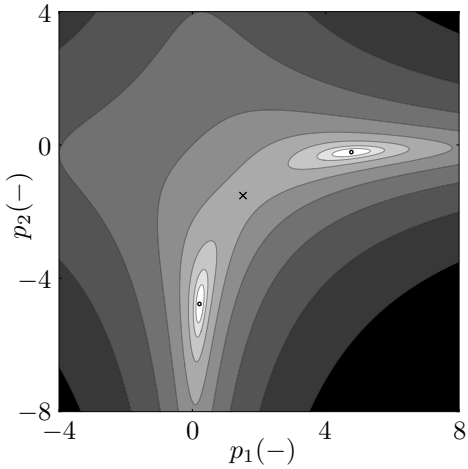

Figure 5.18: Double-well potential $\mathcal{U}(p_1, p_2)$ of a composite plate: The two stable equilibria are indicated by the black dots, the unstable equilibrium is marked by a cross.

Parameter	Value
c_1	-9.9
c_2	9.9
γ	0.14
α	1
m_{12}	0.56
m_{22}	1
μ_{11}, μ_{22}	0.02
μ_{12}	0.011
$\hat{e}_1, \hat{e}_2$	1

Table 5.2: Parameters for the reduced form of the composite equation (3.91)

coordinates p_i are zero for all the equilibria. Moreover, the potential valley is bend almost rectangular in the p_1/p_2-plane. Consequently, the oscillations are essentially pronounced in one degree-of-freedom at once, whereby the change occurs near the unstable equilibrium. This is also true for the equilibria: one coordinate remains close to zero whereby the second coordinate shows a large deflection. Only the unstable equilibrium is symmetric in both coordinates. Due to this characteristic, it is convenient to define the stable equilibria according to the dominant coordinate p_i (p_i-equilibrium). In Fig. 5.19 the characteristic oscillations are illustrated by time signals. In order to describe

the dynamics of a composite plate, not only p_i but also the sum of both coordinates $p_{12} = p_1 + p_2$ can be considered. In many publications on the experimental analysis of composite plates [8,18,30] the measurement is done at a corner of the plate. Thus, both generalized degrees of freedom are measured as well in sum. Therefore, the sum of both coordinates is also shown in the graphs by the black curves. Figure 5.19a shows single-well oscillations about the p_1-equilibrium, while p_2 remains almost constant. This behavior is also shown in the phase diagram (Fig. 5.19b). A similar behavior can be found for cross-well oscillations (Fig. 5.19c). When the coordinate p_1 shows large oscillation amplitudes, the coordinate p_2 remains at low amplitudes. Considering the sum of the time signals p_{12}, a behavior similar to the DUFFING oscillator (Fig. 2.5c) can be observed. Figure 5.19e illustrates that this is also true for inter-well oscillations. In the case of these oscillations in p_{12}, a sophisticated interaction between both degrees of freedom occurs. Thus, the graph suggests that these inter-well oscillations are sensitive to perturbations due to the interactions between both coordinates. This can also be identified by the shape of the inter-well domain within a response map which is shown in the next section.

Response map

Figure 5.20 illustrates the consequence of the sophisticated interaction. The graph shows the snap-through ratio Ψ_{12} obtained from the signal $p_{12} = p_1 + p_2$. To this end, the definition of Ψ_{12} is modified to

$$\Psi_{12} = \frac{1}{n} \sum_{i}^{n} LA_i \quad \text{with} \quad LA_i = \begin{cases} 1, \text{ if } |\hat{a}_i - \hat{a}_{i+1}| \geq \Delta p_1 + \Delta p_2 \\ 0, \text{ other} \end{cases}, \tag{5.18}$$

where the difference Δp_i in coordinate i between both stable equilibria is given by

$$\Delta p_i = \left| p_i \Big|_{p_{1s}} - p_i \Big|_{p_{2s}} \right|, \quad \text{with} \quad p_{is} \text{ being the stable } p_i\text{-equilibrium.} \tag{5.19}$$

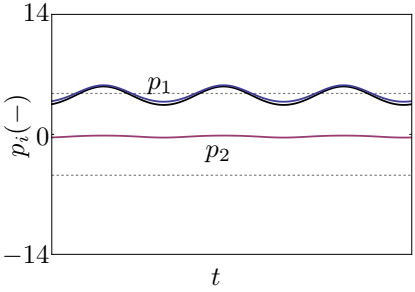

(a) Time Signal: $\Omega = 1, \hat{e} = 0.5$

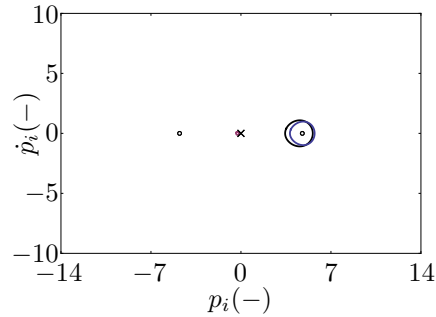

(b) Phase space

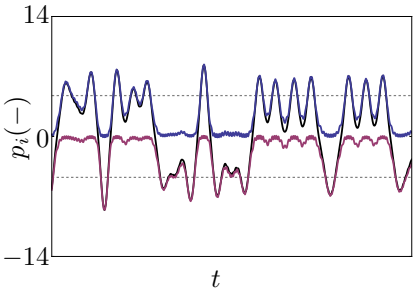

(c) Time Signal: $\Omega = 1.2, \hat{e} = 1$

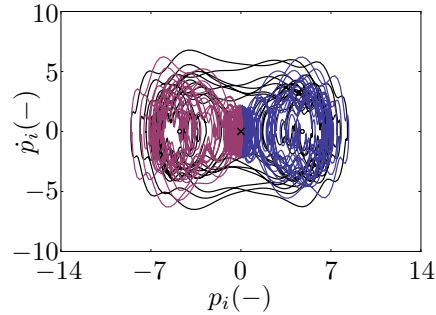

(d) Phase space

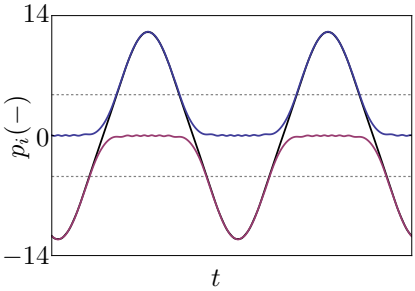

(e) Time Signal: $\Omega = 0.85, \hat{e} = 4$

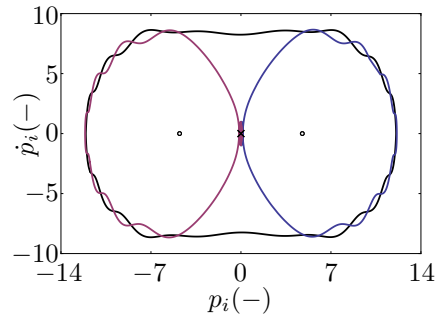

(f) Phase space

Figure 5.19.: Time signals for the different oscillation types. The blue (red) line shows $p_1(p_2)$. The sum $p_{12} = p_1 + p_2$ is given by the black curve.

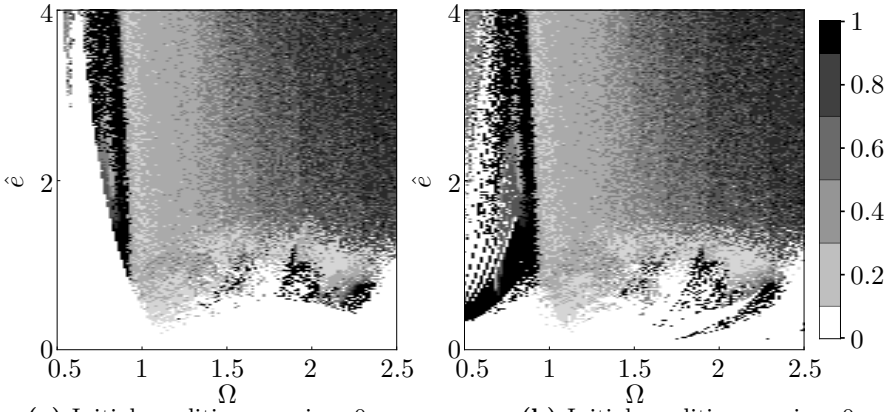

(a) Initial condition p_{1s}, $\dot{p}_i = 0$ **(b)** Initial condition p_u, $\dot{p}_i = 0$

Figure 5.20.: Response map for Ψ_{12}

Figure 5.20 depicts response maps for Ψ_{12} for two initial conditions. Figure 5.20a shows the response for oscillations starting in the stable p_1-equilibrium. Analogously to the bistable DUFFING oscillator, the three differerent oscillation type domains can be identified. Two inter-well domains occur. The lower right inter-well domain shows subharmonic responses, thus it is inappropriate for energy harvesting. When the initial condition is changed to the unstable equilibria p_u (Fig. 5.20b), the inter-well domain increases. This is justified by the fact that more energy is initially introduced. Thus, high energy orbits (inter-well oscillations) can be observed for more excitation parameters. Even though the topology has similarities to the one of the bistable DUFFING oscillator (Fig. 2.9), some major differences can be observed: the inter-well domain is much smaller compared to the one of a DUFFING oscillator. Additionally, the right diffuse boundary of the inter-well domain has a negative slope for the composite plate. This results in a much smaller inter-well domain but larger chaotic domain for these kinds of structures. Section 5.1 illustrates that inter-well oscillations are most suitable for harvesting energy compared to other oscillation types. Therefore, the difference in the topology heavily affects the energy harvesting.

The response map reveals the sensitive character of the inter-well oscil-

lations. The inter-well domain in Fig. 5.20a is not continuous, but is also pervaded by cross-well oscillations. This indicates that small changes in the excitation parameters can prevent the system from performing inter-well oscillations. The numerical simulation also revealed that the stability of the inter-well oscillations depends on the ratio between the eigenfrequencies of the system (4.32). If the ratio is small, it is more likelier for inter-well oscillations to occur. However, this correlation will not be analyzed in detail.

5.3.2. Comparison to analytic criteria

Figure 5.21 shows the response maps for Ψ_{12} in comparison to the analytic criteria. Figure 5.21a demonstrates that the upper saddle-node bifurcation

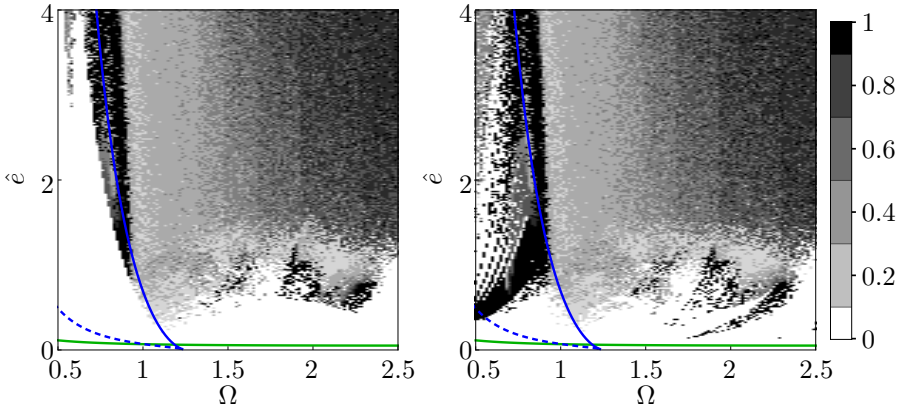

(a) Initial condition p_{1s}, $\dot{p}_i = 0$ **(b)** Initial condition p_u, $\dot{p}_i = 0$

Figure 5.21.: Response map for Ψ_{12} with analytical lower b_{snL} (dashed blue), upper b_{snU} (blue) and b_{snI} (green) saddle-node bifurcations

b_{snU} describes the sharp left boundary of the inter-well domain very well. The small deviation between the numerical and analytical result is due to the approximative character of the perturbation calculus. This is especially perceptible for larger amplitudes $\hat{e}$. The green line shows the bifurcation value b_{snI} which was obtained with the harmonic balance method. To be precise, the criterion shows the threshold value at which large amplitudes in both

degrees of freedom can be observed. This bifurcation value can not be stated as a closed form expression due to its complex bifurcation condition. The bifurcation value is very low, which means that inter-well oscillations may already be observed for low excitation parameters. However, this depends on the initial conditions.

Fig. 5.21b shows such a response map for an initial condition at the unstable equilibrium compared to the analytic criteria. By this initial condition, inter-well oscillations can be observed below the b_{snU} value, but no inter-well oscillation can be observed near and below the b_{snI} bifurcation value. In this case, other initial conditions need to be set. To conclude it can be seen that the analytic bifurcation values can be exploited to roughly describe the solution's topology. Since the inter-well domain is narrow, it can be assumed to be placed along the b_{snU} bifurcation value in conservative case which is given when the initial condition is a stable equilibrium. This gives a good approximation of the topology. Furthermore, the b_{snU} gives the left boundary of the cross-well domain. This domain is significant for harvesting even though inter-well oscillations might not be obtained. Consequently, this analytic bifurcation provides a powerful tool to characterize the solution's topology of the composite plate.

5.4. Electromechanical composite plate

This section presents the results for the electromechanical composite plate. The model was derived in Section 5.4. For the investigations, the non-dimensionalized equation (3.114) with the parameters stated in Table 5.3 will be used. These parameters result from a physical system. Figure 5.22 shows response maps for Ψ_{12} and two different initial conditions. It can be seen that the overall shape does not change compared to a pure composite plate (Fig. 5.20). This is justified by the fact that the electromechanical coupling can be considered as additional damping. The electromechanical coupling allows to determine the normalized harvested power (Eqn. 5.17). Figure 5.23 shows the normalized power for two initial conditions. Similar to the electromechanical beam, a significant increase in P_n can be observed

Parameter	Value
m_{12}	0.56
$m_{22}, \hat{g}_1, \hat{g}_2, \alpha$	1
μ_{11}, μ_{22}	0.015
μ_{12}	0.0086
κ	0.33
γ	0.88
ϕ	0.24
c_1	-10.86
c_2	10.86

Table 5.3: Parameters of the nondimensionalized electromechanical composite plate

for the inter-well domain. This is due to the large amplitudes. Considering the cross-well domain, two areas can be identified. The left side of the cross-well domain which is connected to the inter-well domain shows a relatively small normalized power P_n. This is similar to the results for the electromechanical beam (Fig. 5.17). For larger excitation frequencies Ω the harvested power shows an increase, even though cross-well oscillations are existent. This results from the oscillations with very high amplitudes. Additionally, the do-

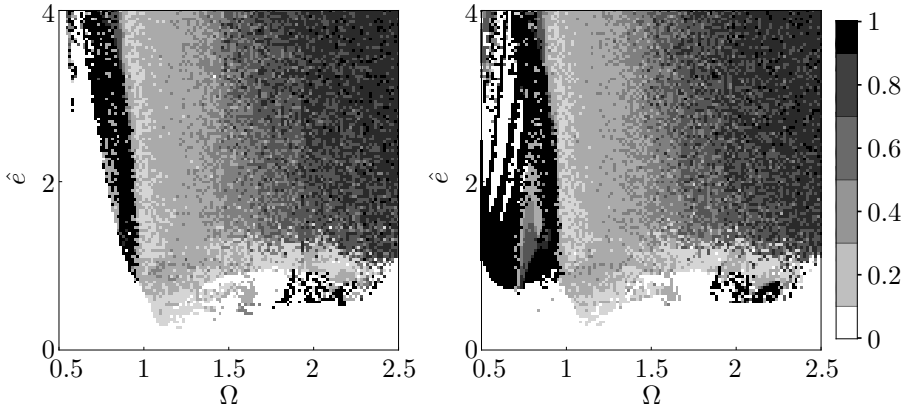

(a) Initial condition p_{1s}, $\dot{p}_i = 0$ **(b)** Initial condition p_u, $\dot{p}_i = 0$

Figure 5.22.: Response map for Ψ_{12}

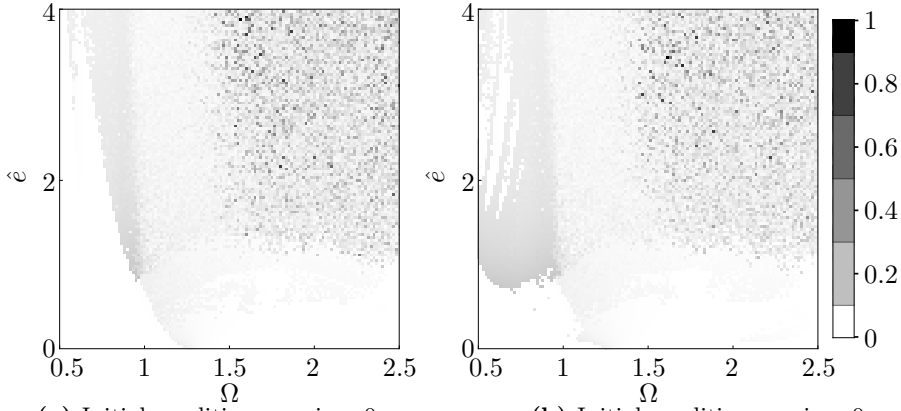

(a) Initial condition p_{1s}, $\dot{p}_i = 0$ **(b)** Initial condition p_u, $\dot{p}_i = 0$

Figure 5.23.: Response map for $P_n / \max P_n$

main shows a large irregularity which results from the chaotic response and the accompanied integration error in the determination of P_n. Due to the high amplitudes, it is not practical to harvest for these amplitudes. At this point it has to be pointed out that the model is only valid for smaller amplitudes, which means that for these high amplitudes responses a model with higher order terms should be considered. Figure 5.24 shows response maps with a

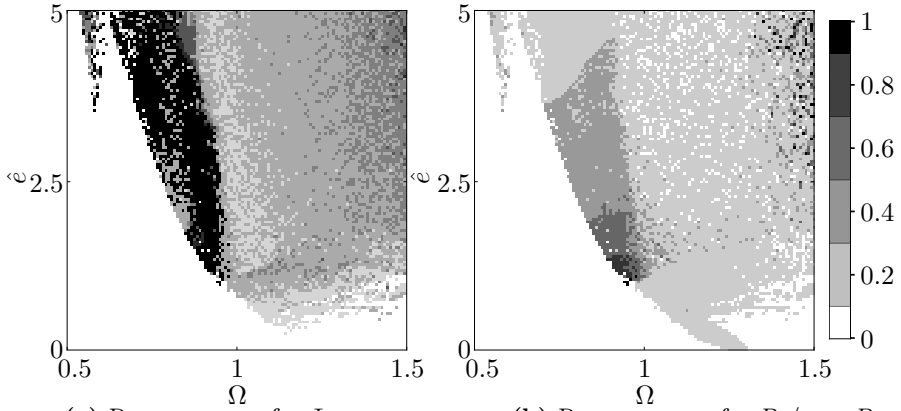

(a) Response map for Ψ_{12} **(b)** Response map for $P_n / \max P_n$

Figure 5.24.: Close-up view of the response maps

close-up view near the inter-well domain. A comparison between the response map showing the snap-through ratio Ψ_{12} (Fig. 5.24a) and the one showing the normalized power (Fig. 5.24b) reveals that the domain for $\Psi_{12} = 1$ coincides with the domain for the highest harvested power. Moreover, for some points at the boundaries of the inter-well domain as well as for some points within the diffuse inter-well domain, a high harvested power can be seen while $\Psi_{12} \neq 1$. This can be explained by looking at a time signal of one of these points. Figure 5.25 shows the time signal for excitation parameters within

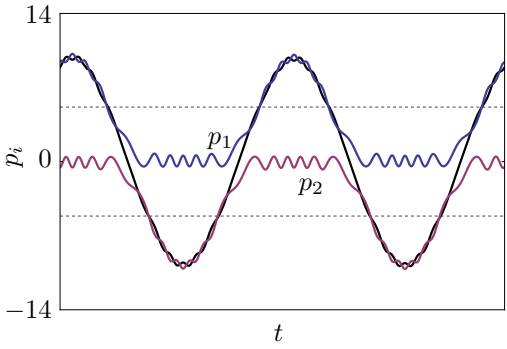

Figure 5.25: Time signal for global inter-well behavior ($\Omega = 0.96, \hat{e} = 2.12$)

the right diffuse edge of the inter-well domain. The graph illustrates global inter-well oscillations. Even though the time signal shows perturbations by an overlayed signal with higher frequency, these oscillations can globally be regarded as inter-well oscillations. These global inter-well oscillations also lead to a high harvested power, although $\Psi_{12} \neq 1$. Thus, the domain with increased harvested power is not diffuse and slightly bigger than the inter-well domain in Fig. 5.24a. Nevertheless, it can be seen that the increase in the harvested power within the inter-well domain is similar compared to the electromechanical beam. Therefore, the inter-well oscillations allow to significantly harvest more power compared to cross-well oscillations. Thus, the composite plate behaves similarly to the electromechanical beam with the large difference that the inter-well domain is much smaller. It was mentioned before that the inter-well domain is very sensitive in the ratio between both eigenfrequencies. This might even be disadvantageous when it comes to robust

energy harvesting.

5.5. Multistable plate

5.5.1. Principal investigations

The response map of the bistable beam (Fig. 5.1a) shows that the inter-well domain emerges from the eigenfrequency of the system. The considered systems were symmetric, so that the eigenfrequencies were the same for both equilibria. This was justified by the fact that no significant advantage is obtained when the eigenfrequencies are split by asymmetry (Section 5.1.2). However, designing systems for which all stable equilibria have more than one eigenfrequency might allow to enhance the broad bandwidth capabilities for energy harvesters. One possibility for doing so is to exploit multiple vibration modes of a structure. However, this does not guarantee that all eigenfrequencies can be designed independently. Another strategy is to exploit multistable structures where the eigenfrequencies can be designed independently. It has to be pointed out that in this context the term multistable is used to describe systems with more than two equilibria. A model for a multistable plate is derived in Section 3.5. The potential energy of the derived model can be written as

$$U(p_1, p_2) = -p_1^2 - \alpha p_2^2 + p_1^4 + \beta p_2^4 + \gamma p_1 p_2 + \eta_1 p_1^3 p_2 + \eta_2 p_1 p_2^3 + \kappa p_1^2 p_2^2, \tag{5.20}$$

whereby the number of parameters were reduced according to (3.133) and (3.135). Selecting the parameters accordingly, a multistable potential can be obtained. Figure 5.26 shows the potential energy $\mathcal{U}$ for the parameters stated in Table 5.4. The considered system is described by Eqn. (3.134). The potential energy shows four stable equilibria for this parameter configuration. The potential is point symmetric. This leads to four different eigenfrequencies for the system, one pair of eigenfrequencies per equilibrium. The difference in the eigenfrequencies dependents on the coupling parameters γ, η_1, η_2 and κ. Due to the high value of the linear coupling parameter γ, it mainly contributes to the deviation of the eigenfrequencies within the equilibria.

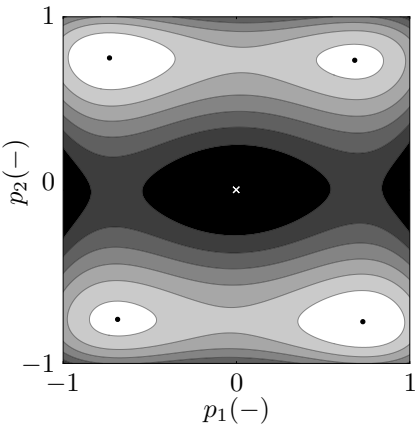

Figure 5.26: Potential energy $\mathcal{U}(p_1, p_2)$ of a multistable plate: The four stable equilibria are indicated by the black dots, whereas the unstable equilibrium is marked by a white cross. The saddle points between the wells are not indicated.

The multistable plate shows similar oscillation types compared to the composite plate. They are illustrated in Fig. 5.27 and 5.28. Figure 5.27 shows single-well and cross-well oscillations. Due to the two degrees of freedom, not the phase-space but the projection of the solution p_1 and p_2 on the potential energy is shown. For the multistable plate, periodic single-well oscillations can occur in all four potential wells. Thereby, the oscillations happen in both degrees of freedom. Cross-well oscillations show a random behavior that can cover the area between two wells or all wells, as shown in Fig. 5.27d. Figure 5.28 shows the two kinds of inter-well oscillations. The oscillations can be about the saddle points between two wells or about the unstable equilibrium

Parameter	Value
α	3.42
β	2.85
γ	0.078
η_1, η_2	0.021
κ	0.0016
m_{22}	1
m_{12}	.11
μ_1, μ_2	0.022
μ_{12}	0.0024

Table 5.4: Parameters of a physical reasonable multistable plate in the reduced form (Eqn. 3.135)

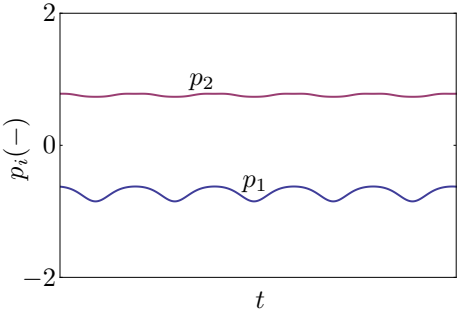

(a) Time Signal: $\Omega = 1.3, \hat{e} = 0.15$

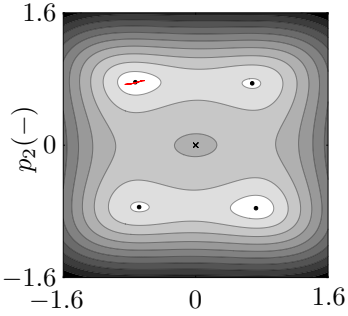

(b) Potential energy

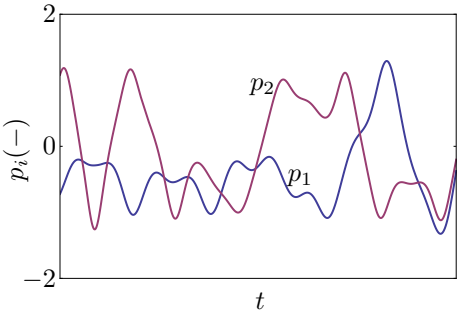

(c) Time Signal: $\Omega = 4.2, \hat{e} = 0.15$

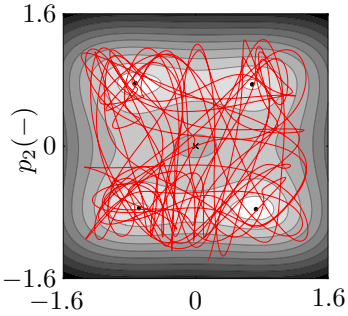

(d) Potential energy

Figure 5.27.: Time signals for single-well and cross-well oscillations. The blue (purple) line shows $p_1(p_2)$. The second graph shows the projection of p_1 and p_2 on the potential energy.

between all equilibria. In the first case, when the oscillations are about a saddle (Fig. 5.28a), one degree of freedom remains mostly unchanged while the other changes its sign, which refers to a snap-through action. For inter-well oscillations about the unstable equilibrium, snap-through actions in both degrees of freedom are observed. Figure 5.28c shows such an oscillation type. For harvesting energy, inter-well oscillations are desired. Both shown inter-well oscillation types emerge from different excitation frequencies Ω. Due to the features of a multistable plate, the eigenfrequencies can be designed in such a way that the domains for the two inter-well types in the excitation parameter

space allow to enhance the bandwidth for energy harvesting. This can be achieved if the different eigenfrequencies are split accordingly. This possible benefit of multistable structures will be investigated in the next section.

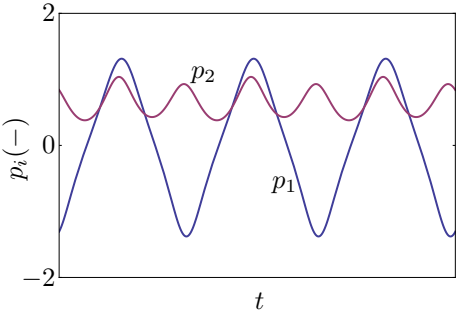

(a) Time Signal: $\Omega = 1.6, \hat{e} = 0.2$

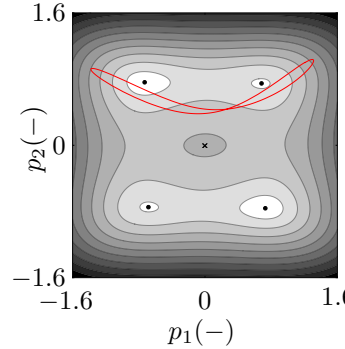

(b) Potential energy

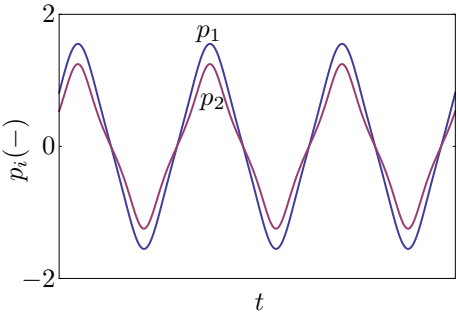

(c) Time Signal: $\Omega = 2, \hat{e} = 0.2205$

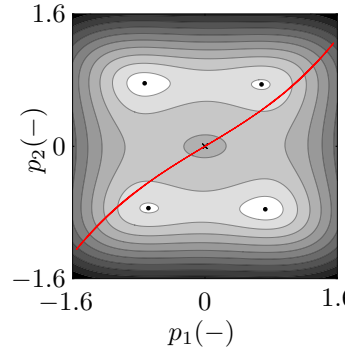

(d) Potential energy

Figure 5.28.: Time signals for the two of inter-well oscillation types. The blue (purple) line shows $p_1(p_2)$. The second graph shows the projection of p_1 and p_2 on the potential energy.

5.5.2. Parameter study

This section presents a parameter study to illustrate the potential benefits of a multistable structure. This will be done by means of the reduced equation

$$\begin{bmatrix} 1 & m_{12} \\ m_{12} & m_{22} \end{bmatrix} \ddot{\mathbf{q}} + \begin{bmatrix} \mu_{11} & \mu_{12} \\ \mu_{12} & \mu_{22} \end{bmatrix} \dot{\mathbf{q}} + \begin{bmatrix} -2q_1 + 4q_1^3 + \gamma q_2 \\ -2\alpha q_2 + 4\beta q_2^3 + \gamma q_1 \end{bmatrix} = \hat{\mathbf{e}}\ \ddot{e}(t). \tag{5.21}$$

As shown in Table 5.4, the linear coupling parameter γ has the greatest influence compared to the higher order coupling terms η_1, η_2 and κ. Thus, the reduced equation only contains the linear coupling parameter γ. The parameters for the following investigations are given in Table 5.5.

Table 5.5: Parameters for the reduced equation of a multistable plate (Eqn. 5.21)

Parameter	Value
α, β, m_{22}	1
γ	0.2
m_{12}	0.01
μ_{11}, μ_{22}	0.05
μ_{12}	0.005

Figure 5.29 shows the influence of the linear stiffness coefficient α on the eigenfrequencies and the equilibria. The coordinates of the equilibria (Fig. 5.29a) and the eigenfrequencies (Fig. 5.29b) are greatly affected by a change of the parameter α. This coherence was also observed for the bistable DUFFING oscillator. Thus, the linear stiffness parameter is crucial for the tuning of the eigenfrequencies.

Figure 5.30 shows the influene of the cubic stiffness coefficient β. As depicted in Fig. 5.30b, a change in the coefficient β mainly affects the equilibria while the eigenfrequencies remain almost constant. Figure 5.31 illustrates the influence of the linear coupling term γ. The graphs show that the parameter γ splits the eigenfrequencies and the equilibria coordinates. Thus, the parameter introduces an asymmetry. As already discussed in Section 5.1.2, asymmetry

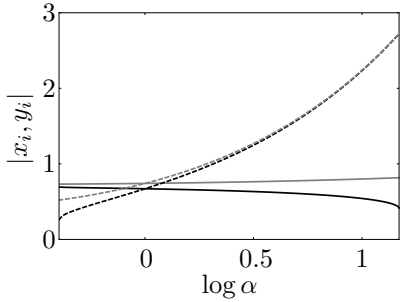

(a) Coordinates of stable equilibria: The solid (dashed) lines indicate the x (y)-coordinate. Lines of same color belong together.

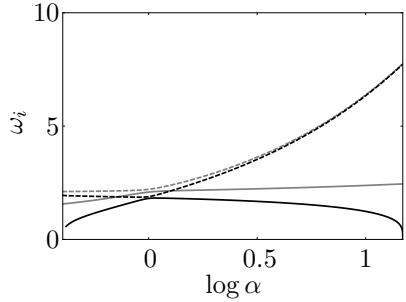

(b) Eigenfrequencies: The solid (dashed) lines indicate the first (second) eigenfrequency. Lines of same color belong together.

Figure 5.29.: Influence of the linear stiffness coefficient α

does not introduce benefits for energy harvesting. Thus, it is desired to keep the coupling parameter γ small. This can be achieved by designing the system accordingly. However, due the nature of the considered structure, it cannot be fully avoided. Figure 5.32 shows response maps for different parameter configurations. The response maps show the sum of the snap-through ratios $\Psi_{12} = \Psi_1 + \Psi_2$ of both degrees of freedom. The parameters Ψ_i were calculated according to

$$\Psi_i = \frac{1}{n} \sum_{i}^{n} LA_i \quad \text{with} \quad LA_i = \begin{cases} 1, \text{ if } |\hat{a}_i - \hat{a}_{i+1}| \geq \Delta p_i \\ 0, \text{ other} \end{cases}, \tag{5.22}$$

whereby the difference Δp_i in coordinate p_i between the equilibria is given by

$$\Delta p_i = |\max p_i - \min p_i| \,. \tag{5.23}$$

Figure 5.32a shows the response map for equal stiffness parameters in both degrees of freedom. The topology is similar to the one of a simple DUFFING oscillator. Thus, no advantage is given for this configuration. The benefit of a multistable structure is obtained when both stiffness parameters α and β are tuned to split the eigenfrequencies while keeping the equilibria coordinates

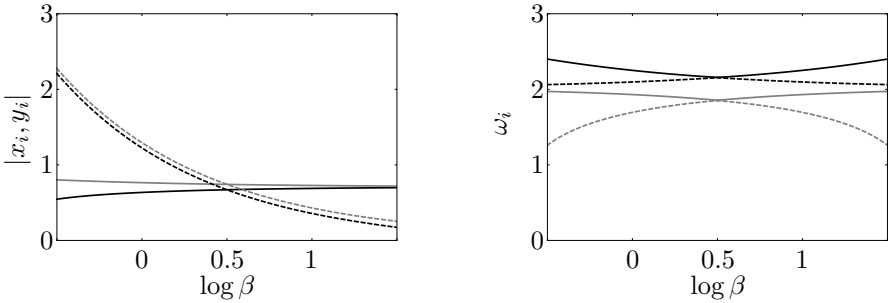

(a) Stable Equilibria **(b)** Eigenfrequencies

Figure 5.30.: Influence of the cubic stiffness coefficient β

mostly unchanged. This is shown in Fig. 5.32b. Due to the chosen parameters the inter-well oscillation domains are shifted against each other. On the left side a region with the value $\Psi_{12} = 1$ can be identified. Within this domain snap-throughs in the first degree of freedom can be observed ($\Psi_1 = 1$). On the right side of this domain an even larger $\Psi_{12} = 2$ domain that corresponds to inter-well oscillations about the unstable equilibrium (Fig. 5.28d) is shown. This means that $\Psi_i = 1$ for both coordinates. Both domains are suitable for energy harvesting. This shows that by a suitable design of a multistable plate the bandwidth for energy harvesting can be increased. This increase is

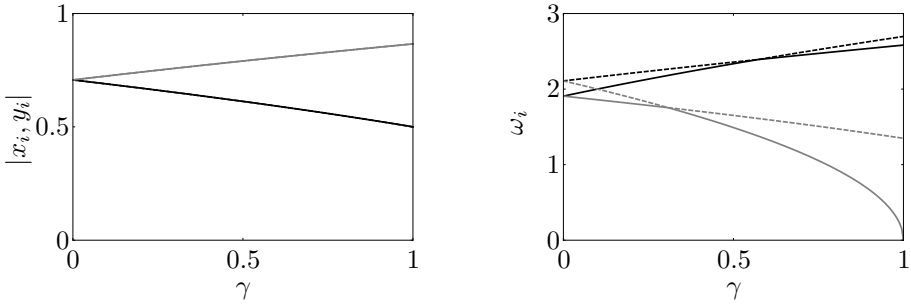

(a) Stable Equilibria **(b)** Eigenfrequencies

Figure 5.31.: Influence of the cubic stiffness coefficient γ

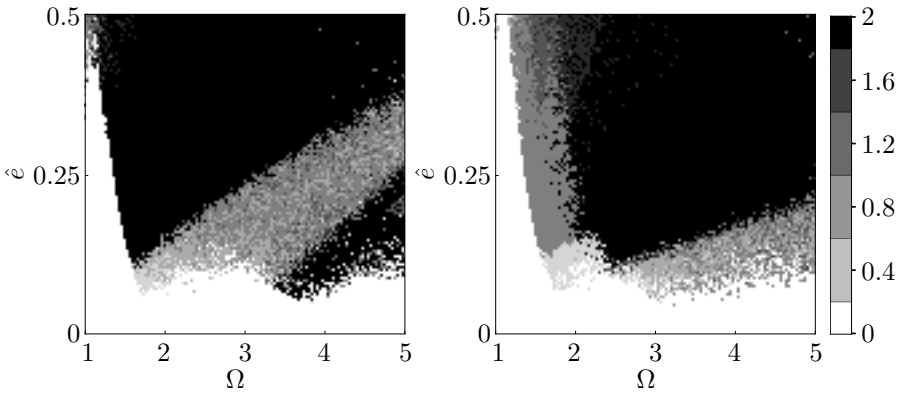

(a) Ψ_{12} for $\alpha = 1, \beta = 1, \gamma = 0.2$ **(b)** Ψ_{12} for $\alpha = 3, \beta = 3, \gamma = 0.2$

Figure 5.32.: Response maps for $\Psi_{12} = \Psi_1 + \Psi_2$ for different parameter configurations. Initial condition: Lower potential well and $\dot{p}_i = 0$

also shown by the graph in Fig. 5.33. It is demonstrated that the bandwidth for inter-well oscillations and thus for energy harvesting can be enhanced by orders of magnitude. This illustrates the ability to enhance the harvesting bandwidth considerably by this kind of structure.

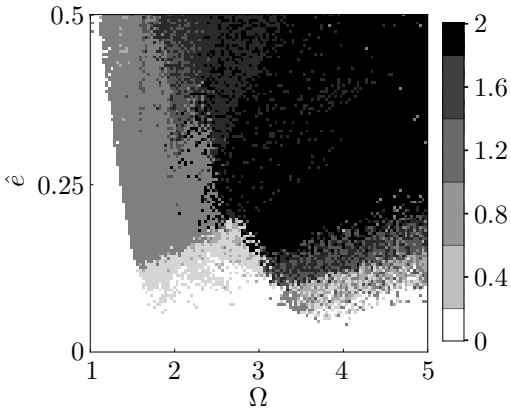

Figure 5.33: Response maps for $\Psi_{12} = \Psi_1 + \Psi_2$ with $\alpha = 5$, $\beta = 5$, $\gamma = 0.2$. Initial condition: Lower potential well and $\dot{p}_i = 0$

5.6. Combined harmonic and noise excitation

In this section, the previously presented structures are shortly analyzed concerning combined harmonic and noise excitation. One fundamental assumption of the preceding analysis is that the real-world excitation can mainly be modelled as harmonic. In this case the bifurcation values derived in Chapter 4 provide a powerful framework for the description of the solution's topology. In the following, the systems will be investigated for a combined harmonic and noise excitation, with focus on the change of the solution's topology. It has to be pointed out that this section does not aim to conduct a full qualitative analysis of these systems under noise. Thus, some assumptions and limitations on the characterization of the noise excitation are made. However, the analysis gives insight in how well the results for pure harmonic excitation can be transferred to real-world excitations. A related work for the DUFFING oscillator can be found in the publication by WIEBE and SPOTTSWOOD [73]. Their focus is on the co-existence of different solution types under noise.

5.6.1. Bistable DUFFING oscillator

The bistable DUFFING oscillator with combined harmonic and noise excitation will be analyzed in this section. This will be done by means of the equation

$$\ddot{x}(t) + \mu\,\dot{x}(t) - \alpha\,x(t) + \beta\,x^3(t) = \hat{e}\,\ddot{e}(t) + \rho\,\omega^2 x_s\,\sigma_i(t), \tag{5.24}$$

with

$$e(t) = \sin\Omega t$$

and the parameters given in Table 5.6. The term $\rho\,\omega^2 x_s$ provides the amplitude for the stochastic process $\sigma_i(t)$, yet to be defined. The parameters

Table 5.6: Parameters for the bistable DUFFING oscillator

Parameter	Value
α, β	1
μ	0.05

ω and x_s are given by Eqns. (2.3) and (2.4). The factor $\omega^2 x_s$ is introduced such that the intensity amplitude ρ is dimensionless. Equation (5.24) is investigated for a GAUSSian and a pink noise process. A GAUSSian process (GAUSSian noise) $\sigma_g(t)$ is characterized by a constant power spectral density and pink noise $\sigma_p(t)$ by a decreasing power spectral density over the frequency by $1/f$. Real-world excitations show similarities to pink noise, because the amplitudes decrease over the frequency and, thus the power spectral density. Moreover, the excitation spectra reveal some dominating frequencies which indicate the eigenfrequencies of the structure. This is illustrated in the introduction (Fig. 2.1). Thus, in this section real-world excitation is approximated by a combined harmonic and noise excitation. For the following investigation the stochastic process $\sigma_i(t)$ contains frequency components up to ten times the eigenfrequency $\omega = \sqrt{2\alpha}$. This low-pass filter is applied to reduce the numerical effort which comes along with high frequencies components in teh stochastic process $\sigma_i(t)$.

For the analysis, various response maps in the range $0 < \hat{e} \leq 0.4$ and $0.5 \leq \hat{\Omega} \leq 2.5$ are generated by the integration of Eqn. (5.24) for different intensity amplitudes ρ. Figure 5.34 shows response maps for the snap-through

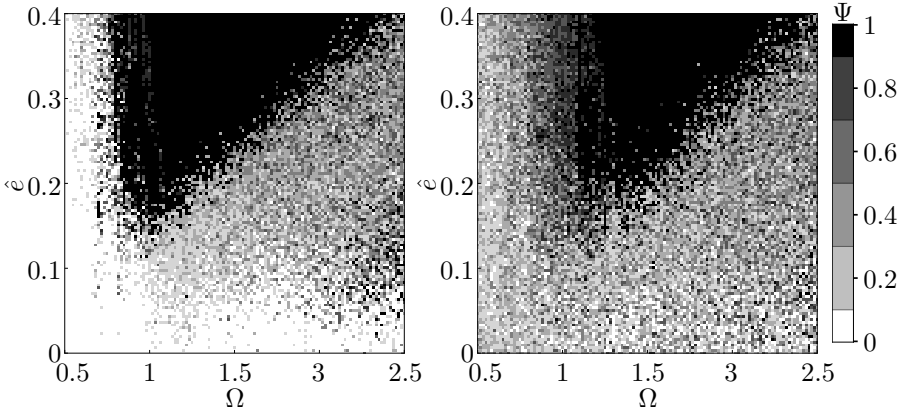

(a) $\rho = 0.01$ **(b)** $\rho = 0.02$

Figure 5.34.: Response maps for Ψ for different intensities ρ (GAUSSian noise)

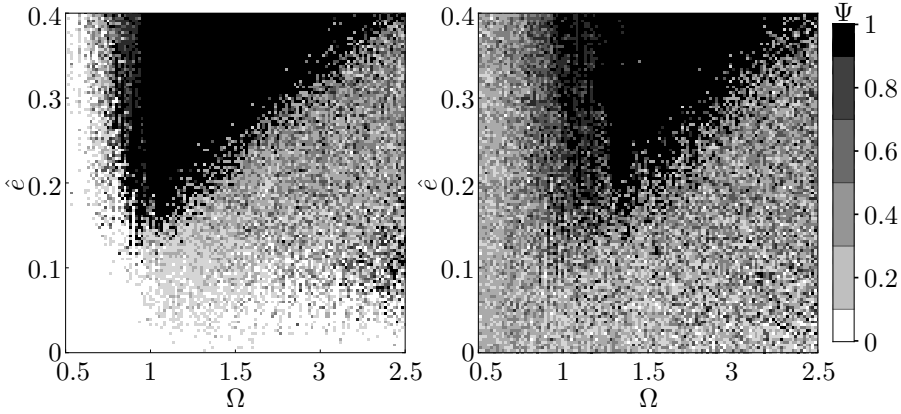

(a) $\rho = 0.01$ **(b)** $\rho = 0.02$

Figure 5.35.: Response maps for Ψ for different intensities ρ (Pink noise)

ratio Ψ under combined harmonic and GAUSSian noise excitation. Each point presents a single integration for a stochastic process $\sigma_i(t)$ over a long time to ensure a steady state-like oscillation. Figure 5.34a shows that the inter-well domain increases along the boundaries. A comparison of this graph with Fig. 2.9a shows that the inter-well domain mainly increases on the left side. This corresponds to the observation that changed initial conditions lead to a magnification of the inter-well domain on the left side (Section 2.1.3). The effect of noise can be interpreted as modified initial conditions. The right diffuse edge of the inter-well domain remains essentially unchanged. This verifies the statement that the inter-well domain is minimal for a low initial energy, but increases for other initial conditions which has the same effect as noise. Figure 5.34b shows that almost all single-well oscillations are vanished. What remains are mainly cross-well and inter-well oscillations. However, the main shape of the inter-well domain is still preserved. Figure 5.35 shows two response maps for pink noise. For the value $\rho = 0.01$ the response map is similar to the one for GAUSSian noise (Fig. 5.34a). The inter-well domain increases mainly about the left boundary. Figure 5.35b shows a response

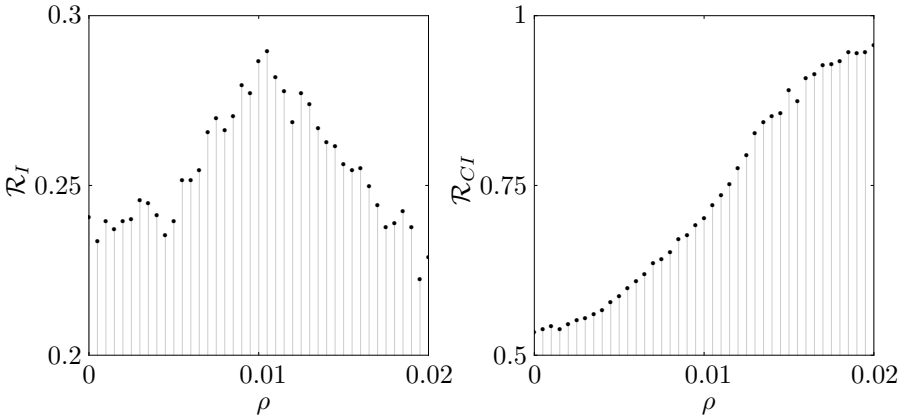

(a) $\mathcal{R}_I$ over the noise intensity ρ **(b)** $\mathcal{R}_{CI}$ over the noise intensity ρ

Figure 5.36.: Snap-through ratio $\mathcal{R}_I$ and $\mathcal{R}_{CI}$ over the intensity ρ for GAUSSian noise ($\alpha = 1, \beta = 1, \mu = 0.05, \Omega = \sqrt{2}$)

map for a higher intensity amplitude ρ. The graph shows that all single-well oscillations have vanished for this intensity amplitude. A comparison between the graph with Fig. 5.34b reveals that the ratio of inter-well oscillations is slightly higher.

The shown response maps illustrate the influence of noise. On the first hand, the topology of the solution does not change significantly. This implies that the analytical bifurcations values from Chapter 4 can also be applied to systems with combined harmonic and noise excitation. Hereby, the accuracy is higher for low intensity amplitudes ρ. On the other hand, the added noise leads to an increased inter-well domain which is beneficial for energy harvesting. This shows that the inter-well domain for minimal initial energy is a conservative estimate. Not only changed initial conditions lead to a magnification, but also added noise in the excitation.

The influence of the intensity amplitude ρ on the different oscillation types is analyzed in the following. Various response maps for different intensity amplitudes ρ are generated. From each response map the overall ratio of inter-well oscillations $\mathcal{R}_I$ and the ratio of inter- and cross-well oscillations $\mathcal{R}_{CI}$ are calculated. Figure 5.36 shows both ratios over the intensity amplitude ρ for

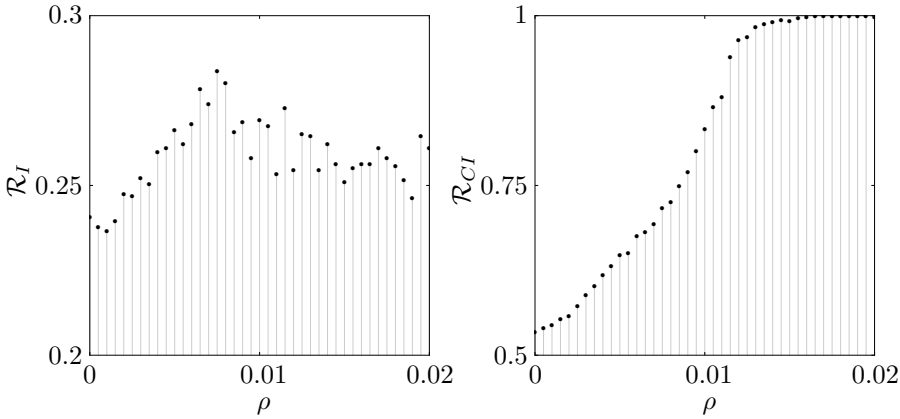

(a) $\mathcal{R}_I$ over the noise intensity ρ **(b)** $\mathcal{R}_{CI}$ over the noise intensity ρ

Figure 5.37.: Snap-through ratio $\mathcal{R}_I$ and $\mathcal{R}_{CI}$ over the intensity ρ for pink noise ($\alpha = 1, \beta = 1, \mu = 0.05, \Omega = \sqrt{2}$)

Gaussian noise.

In Fig. 5.36a the ratio of inter-well oscillations $\mathcal{R}_I$ initially increases for a growing amplitude ρ. At an amplitude of $\rho \approx 0.01$ the ratio decreases again. This shows that the additional Gaussian noise helps to increase the number of inter-well oscillations for the considered excitation parameter domain when the intensity amplitude is small. At a further increase of the amplitude ρ, the ratio inter-well oscillations decreases. What follows is a reduction of the ratio $\mathcal{R}_I$. This correlation is illustrated in Fig. 5.36b. The graph shows that the ratio of single-well oscillations steadily decreases with a growing amplitude ρ. The ratio $\mathcal{R}_{CI}$ converges to 1 for large amplitudes. It implies that primary cross-well and inter-well oscillations are existent. This positively affects the energy harvest. Figure 5.37 shows the same ratios for pink noise. Figure 5.37a reveals that pink noise helps to increase the ratio of inter-well oscillations in the whole considered intensity amplitude domain. This is also illustrated in the graph for $\mathcal{R}_{CI}$ in Fig. 5.37b. The graph shows that the ratio of single-well oscillations decreases earlier compared to Fig. 5.36b.

Figures 5.36 and 5.37 show that the added noise even increases the overall performance of bistable Duffing oscillator like energy harvesters. This is

justified by the increase of the ratio for inter-well and cross-well oscillations in the considered domain. According to the results of Section 3.1, this affects the energy harvest beneficially.

5.6.2. Bistable electromechanical system

This section presents a short analysis of an electromechanically coupled system under different combined harmonic and noise excitation. In the previous section it was already shown that the ratio of inter-well and cross-well oscillations increases when noise is added to the excitation. Thus, this section will only investigate the consequence for harvesting energy. To this end, the equation

$$\ddot{x}(t) + \mu\ \dot{x}(t) - \delta\ v(t) - \alpha\ x(t) + \beta\ x^3(t) = \hat{e}\ \ddot{e}(t) + \rho\omega^2 x_s \sigma_i(t), \quad (5.25a)$$

$$\phi\ v(t) + \eta\ \dot{x}(t) + \dot{v}(t) = 0, \quad (5.25b)$$

will be considered. The noise is given by the stochastic process $\sigma_i(t)$ and the amplitude $\rho\,\omega^2 x_s$. The stochastic process is defined in the previous section. The coefficient ρ is the non-dimensional intensity amplitude and ω and x_s the eigenfrequency and the stable equilibrium of the system (2.3 and 2.4). For the function $\sigma_i(t)$, GAUSSian noise ($\sigma_g(t)$) and pink ($\sigma_p(t)$) noise are examined. Various response maps for the normalized power P_n (5.17) in the excitation parameter range $0 < \hat{e} \leq 0.4$ and $0.5 \leq \hat{\Omega} \leq 2.5$ are generated by the integration of Eqn. (5.25). It is convenient to consider a single reference value. Thus, from each response map the mean power $\bar{P}$ is calculated. This value is obtained by averaging the sum of P_n for every integration point. Therefore, the value $\bar{P}$ gives a lumped statement about the harvested energy. For convenience the results for $\bar{P}$ are normalized by $\bar{P}_{\rho=0}$. This gives a measure of the variation for the mean power compared to pure harmonic excitation. Figure 5.38 shows the normalized power $\bar{P}$ over different noise intensities ρ for GAUSSian and pink noise. Both graphs show that the mean power P_n increases for both noise functions by a considerable amount. This is justified by the underlying oscillation types. Similar to the results of the previous section the ratio R_I decreases over the intensity amplitude ρ. This is exemplarily

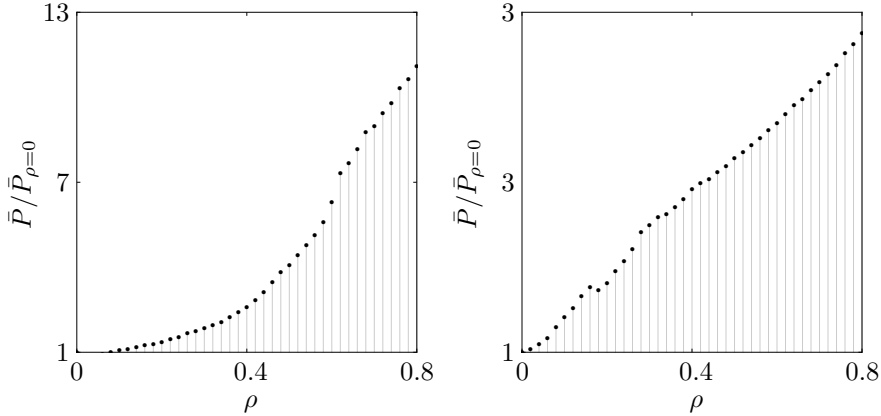

(a) Gaussian noise **(b)** Pink noise

Figure 5.38.: Mean power $\bar{P}/\bar{P}_{\rho=0}$ for different noise functions

shown in Fig. 5.39.

A comparison between both graphs (Fig. 5.38) reveals that the increase in the normalized power is higher for Gaussian noise. This can be explained in terms of the decreasing amplitude over the frequency for pink noise: less energy is available for higher frequencies, thus the gain is decreased. However, the increase for both normalized $\bar{P}$ is large. The chosen intensity amplitude ρ range was chosen such that that the response of the system is dominated by

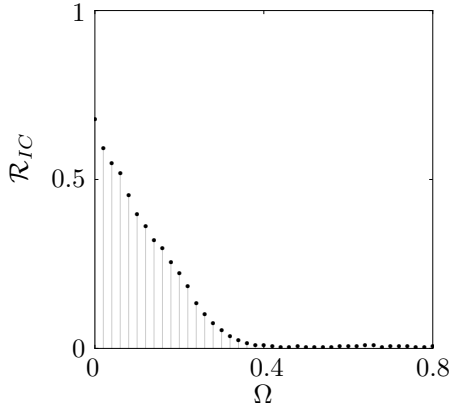

Figure 5.39: Ratio of inter-well oscillations $\mathcal{R}_I$ over ρ for Gaussian noise

the noise excitation for the parameter $\rho = 0.8$. This explains the steep gain in the power. However, no qualitative statement can be made by the parameter $\bar{P}$ because it averages the whole excitation parameter domain. In real-world applications the harvesting is preferably conducted in the inter-well domain, this is not considered by the parameter $\bar{P}$.

5.6.3. Composite plate

This section presents a short study of the reduced composite plate discussed in Section 5.3. Based on Eqn. (3.91) with the parameters given in Table 5.2 the stochastic process

$$n(t) = \rho\omega_1^2 p_1\Big|_{p_{1s}} \sigma_i(t) \tag{5.26}$$

is added to the right side of the equation. The parameter ρ denotes the nondimensional intensity amplitude, ω_1 the lowest eigenfrequency and $p_1\Big|_{p_{1s}}$ the p_1-coordinate of the p_1-equilibrium. Two different stochastic processes $\sigma_i(t)$ are investigated: GAUSSian noise (σ_g) and pink noise (σ_p). With the modified equation various response maps in the range of $0 < \hat{e} \leq 4$ and $0.5 \leq \hat{\Omega} \leq 1.5$ for different intensity amplitudes ρ are generated. Figure 5.40 shows response maps for the snap-through ratio Ψ_{12} (5.22) for two intensity amplitudes ρ. The graph shows that the diffuse inter-well domain is reduced by the introduced GAUSSian noise. This can be explained by the sensitive interactions between both degrees of freedom that are perturbed by the noise. Moreover, the cross-well domain increases. This is induced also by the noise which helps the system to exhibit snap-throughs. Figure 5.41 shows similar results for pink noise. However, the solution's topology for pink noise does not dissolve to the same extent than for GAUSSian noise. This can be explained by the decreasing amplitude over frequency for pink noise, thus the energy introduced by pink noise is lower

From each response map the ratio of inter-well oscillations is calculated. This results in the overall inter-well ratio $\mathcal{R}_I$. Analogously, the ratio for $\Psi_{12} \neq 0$ values results in the ratio $\mathcal{R}_{CI}$. The results for both rations $\mathcal{R}_I$ and $\mathcal{R}_{CI}$ under added GAUSSian noise are shown in Fig. 5.42. Figure 5.42a

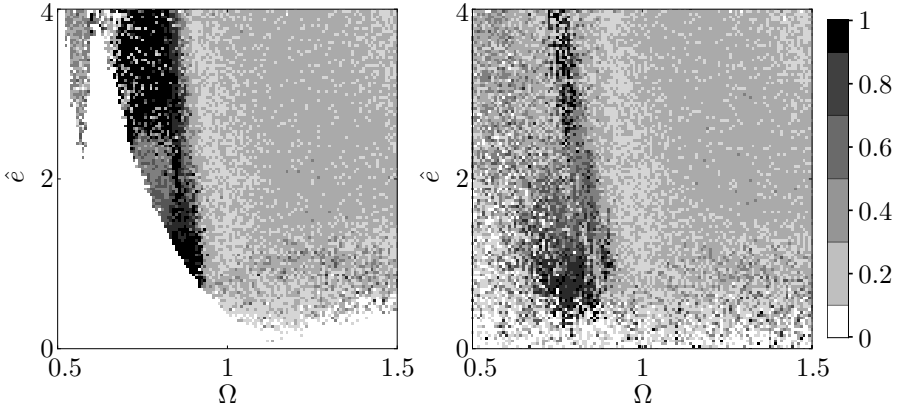

(a) $\rho = 0.004$ **(b)** $\rho = 0.008$

Figure 5.40.: Response map for Ψ_{12} under GAUSSian noise

shows that the ratio of inter-well oscillations decreases when noise is added. This can be explained by the sensitive interaction between both degrees of freedom that results in inter-well oscillations. When noise is introduced, this oscillation type is perturbated so that it looses stability. Moreover, the single-well oscillations become unstable by the noise. This is illustrated in Fig. 5.42b. The graph represents an increasing ratio $\mathcal{R}_{CI}$ over the amplitude ρ. For a large amplitude ($\rho = 0.008$), single-well oscillations have mostly vanished. A similar behavior can be seen for pink noise excitation. Figure 5.43 shows the rations $\mathcal{R}_I$ and $\mathcal{R}_{CI}$ over the amplitude ρ. A comparison between Fig. 5.42 and 5.43 clarifies that pink noise does not lead to such a strong decrease for the ratio $\mathcal{R}_I$ compared to GAUSSian noise. While the inter-well ratio drops close to zero for GAUSSian noise, the ratio is about $\mathcal{R}_I \approx 0.125$ for pink noise. This can be explained by the decreasing amplitude for higher frequencies that do not destabilize the inter-well oscillations in the same way as GAUSSian noise. However, the ratio of single-well oscillations (Fig. 5.43b) proceeds similarly for both noise excitations. This means that in both cases the single-well oscillations loose stability while the cross-well domain increases.

These observations lead to the conclusion that the combined excitation

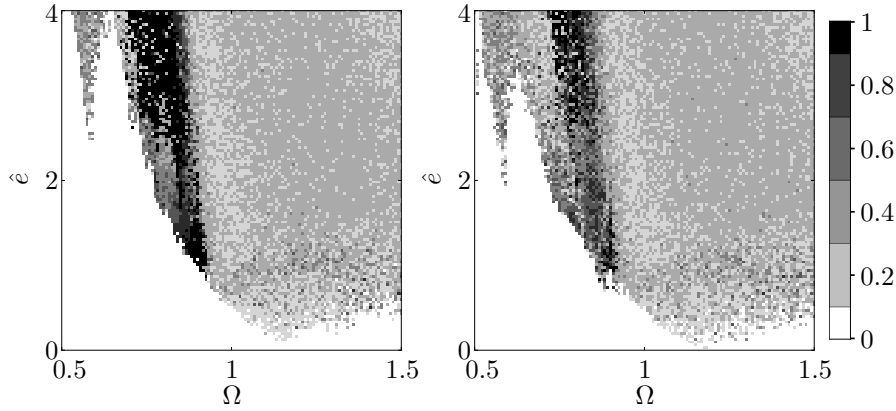

(a) $\rho = 0.004$ **(b)** $\rho = 0.008$

Figure 5.41.: Response map for Ψ_{12} under pink noise

affects the inter-well domain negatively. The ratio of inter-well oscillations decreases for both noise signals and, thus the domain for effective energy harvesting. However, considering the definition of the snap-through ratio Ψ_{12} (Eqn. 5.22), it is apparent that a slight irregularity in the time signal

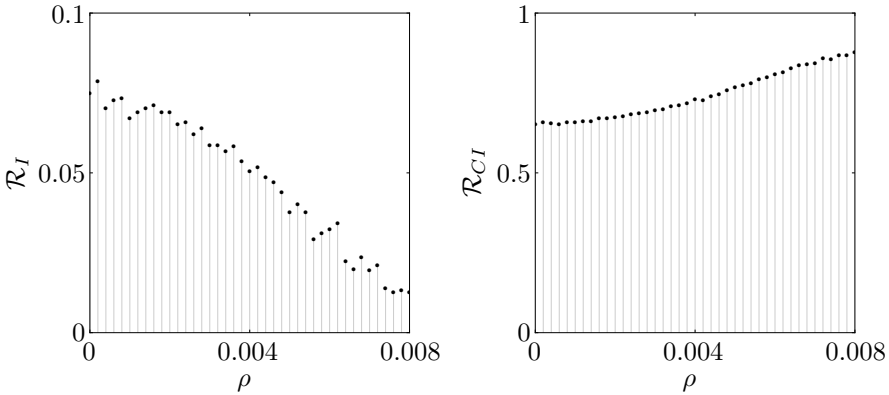

(a) $\mathcal{R}_I$ over the noise intensity ρ **(b)** $\mathcal{R}_{CI}$ over the noise intensity ρ

Figure 5.42.: Influence of the the intensity amplitude ρ on the ratios $\mathcal{R}_I$ and $\mathcal{R}_{CI}$ for Gaussian noise

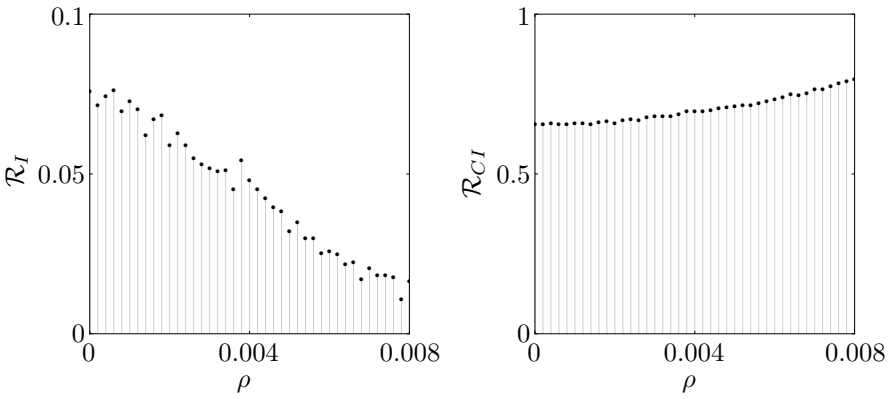

(a) $\mathcal{R}_I$ over the noise intensity ρ **(b)** $\mathcal{R}_{CI}$ over the noise intensity ρ

Figure 5.43.: Influence of the the intensity amplitude ρ on the ratios $\mathcal{R}_I$ and $\mathcal{R}_{CI}$ for pink noise

leads to $\Psi < 1$. Inter-well oscillations for the composite plate result from a sensitive interaction between both degrees of freedom. The noise perturbes this interaction. Thus, not every time signal might show a significant drop for the harvested energy, even though no inter-well oscillations according to the snap through ratio Ψ_{12} are existent. This was already discussed in Section 5.4.

A comparison between the results for the composite plate (Figs. 5.42 and 5.43) and the results for the bistable beam (Figs. 5.36 and 5.37) reveals a significant difference between these structures. Whereas the ratio $\mathcal{R}_I$ shows an increase, for the beam with GAUSSian and pink noise, the composite plate only shows a decrease. This difference was explained in terms of the sensitive interactions of the inter-well oscillations for the composite plate. This significant difference between the structures implicates consequences for the energy harvesting capabilities. This consequence can be illustated in terms of the response maps for the beam (Fig. 5.35) and the composite plate (Fig. 5.41). The inter-well domain of the beam is expanded, while being diminished for the composite by the noise. Moreover in Sections 5.2 and 5.4 is was shown that the inter-well domain is the most suitable domain for energy harvesting. This is valid for both structures. This implies that the noise influences the

energy harvesting beneficial when the harvesting is done by an electromechanical beam. In contrast to the electromechanical beam, the electromechanical composite plate reduces its efficiency under noise.

This section is concluded by pointing out that for robust energy harvesting the excitation source needs to be considered carefully when designing the energy harvester. The characterization of the excitation is crucial not only for designing the system parameters accordingly but also for selecting the mechanical structure of the harvester.

6. Experimental investigations

This chapter presents experiments of the different structures analyzed in the previous chapter. The experiments are carried out to analyze how well the numerical and analytical findings can be transferred to real-world applications. This is done by means of three different structures which are investigated on simple test rigs. First of all, a bistable beam is investigated. This allows to verify experimentally the analytical and numerical results of a structure described by the bistable DUFFING equation. The second system consists in a bistable electromechanical beam which is analyzed concerning its main features discussed in Chapter 5. Moreover, the experimental results are compared to the analytic and empiric criteria (Chapter 4). Eventually, a bistable electromechanical composite plate is investigated.

6.1. Experiments with beam structures

6.1.1. Experimental setup

Figure 6.1 shows the experimental setup. The setup consists of a guided mounting which is excited with a motor by means of a slider-crank mechanism. The considered beam structures are attached to the mounting. Figure 6.1b shows a fixed beam in the guided mounting. The guide is realized by a linear bearing. Figure 6.2 shows the crank mechanism, realized by a pin that sits on a movable sled. This sled can be shifted to adjust the excitation amplitude. The asynchronous motor is controlled by a frequency converter to run at various frequencies. By this setup, only harmonic excitations are feasible. Contrary to the derivation of the beam model in Section 3.1, the nonlinearity is obtained by a magnet arrangement as indicated in Fig. 6.1b. To this end, one magnet is fixed to the tip of the beam. The other magnet is attached

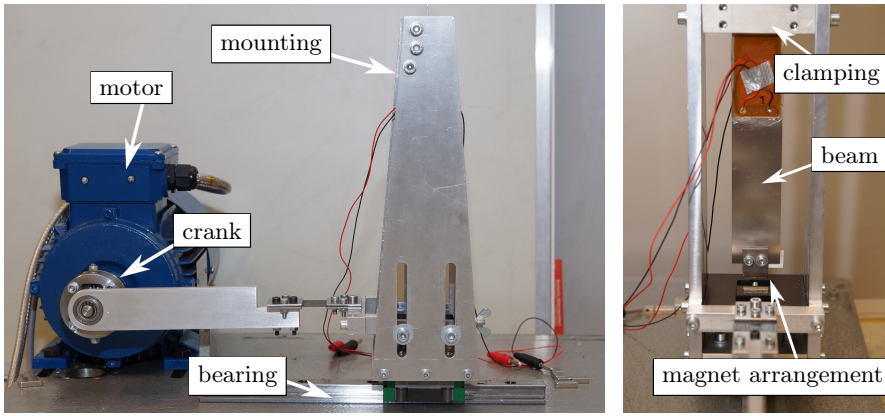

(a) Side view **(b)** Mounting

Figure 6.1.: Experimental setup

to a movable table to tune the system's parameters. The displacement of the beam is captured by laser triangulation sensors. The signal acquisition is performed by a CompactDAQ platform from National Instruments® in combination with LabView.

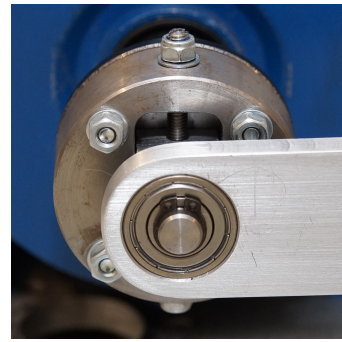

Figure 6.2: Close view of the crank mechanism

6.1.2. Bistable prestressed beam

The bistable beam is described by the bistable DUFFING equation

$$\ddot{x}(t) + \mu\,\dot{x}(t) - \alpha\,x(t) + \beta\,x^3(t) = m_e\;\hat{e}\;\ddot{e}(t), \tag{6.1}$$

with m_e being the ratio of the modal mass and the excitation mass. The parameters of this equation are identified with convenient methods [64]. Initially, the system is tuned to have equal eigenfrequencies for both equilibria. The parameters are subsequently accessed by considering the eigenfrequencies, equilibria and decay functions. The proportionality factor m_e is determined by comparing experimental results with numerical simulations. The parameters for the beam are stated in Table 6.1. With the shown experimental

Parameter	Value	Unit
α	4424.3	$\frac{1}{\mathrm{s}^2}$
β	$13 \cdot 10^7$	$\frac{1}{\mathrm{s}^2\mathrm{m}^2}$
μ	0.2645	$\frac{1}{\mathrm{s}}$
m_e	1.0563	-

Table 6.1: Experimentally obtained parameters from the setup

setup, a response map for the snap-through ratio Ψ is generated. Figure 6.3 shows the experimental results. The topology is similar to the numerical simulations. The map reveals inter-well oscillations for $\hat{e} > 1$ mm. The upper

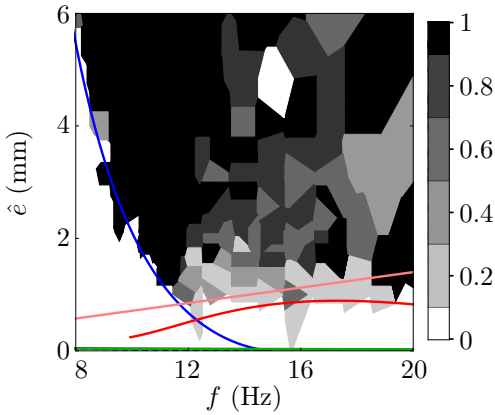

Figure 6.3: Response map for Ψ

saddle-node bifurcation b_{snU} is shown by the blue solid line. This bifurcation value limits, similar to the numerical simulations (Fig. 5.8a), the left edge of the inter-well domain in a nice way. The criterion for chaos is depicted by the red line. The bifurcation value for the saddle-node bifurcation b_{snI} (green line) and the results from the MELNIKOV function (purple line) are hardly visible, as they are at the bottom of the graph. The same applies to the lower saddle-node bifurcation b_{snU} (blue dashed line). For the frequency domain shown in Fig. 6.3, both bifurcation values are too low to give useful limitations of the inter-well domain. Still, the evidence from these bifurcation values are the same. Stable inter-well oscillations exist above the b_{snI} value, though for other initial conditions. However, this is not easy to realize in the experiment. The empiric criterion is shown by the pink line. This line is above all other bifurcation values, giving an empiric description of the diffuse right edge of the inter-well domain. It is apparent from Fig. 6.3 that the inter-well domain does not show this characteristic edge as in Fig. 5.1a.

In the experiment chaotic solutions are found above the empiric criterion while inter-well oscillations are expected according to numerical simulations. Moreover, the diffuse right edge of the inter-well domain is much steeper compared to numerical simulation (Fig. 5.9). This might be explained with the model describing the bistable beam. The damping is modelled by a viscoelastic constant μ. This approximation might be inaccurate, especially for large amplitudes when the damping is more involved. Another reason might be that the model is only developed up to the third order. Thus, the model looses accuracy for larger deflections.

This correlation is also depicted in the bifurcation diagram (Fig. 6.4). The graph shows the amplitude $\hat{a}$ over the frequency f. The lines indicate analytic results which are obtained by the multiple scales and the harmonic balance method. Single-well oscillations are shown by the black lines and the inter-well oscillations by the blue ones. The dashed lines indicate unstable nodes. The experimental results are given by the gray points, whereby different initial conditions are used to obtain these points. For small amplitudes $\hat{a}$ a good agreement between the analytical prediction and the experiment exists. Considering the inter-well saddle S_I, the agreement is only satisfactory for lower

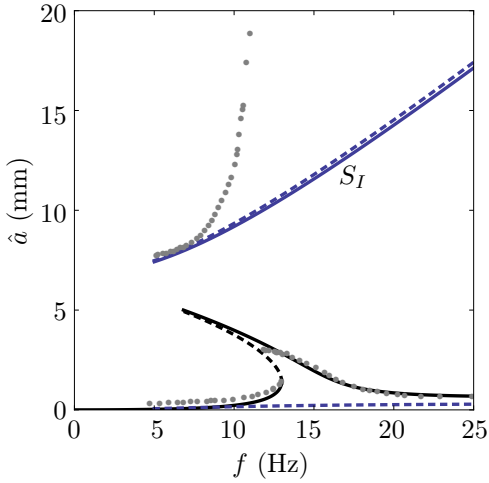

Figure 6.4: Bifurcation diagram comparing analytical results (lines) with experimental results (gray dots) for $\hat{e} = 0.32\,\mathrm{mm}$

amplitudes. As the amplitude increases, the experimental amplitudes drift away from the analytical prediction. Thus, the bifurcation diagram nicely illustrates the constraints of the model (Eqn. 6.1) for large amplitudes. This deviation can be remedied by modelling the beam with higher order terms.

Nonetheless, it has to be pointed out that the analytical methods provide a powerful tool to give an estimate of the systems' topology in advance. Figure 6.3 shows that especially the upper saddle-node bifurcation b_{snU} and the criterion for chaos can be exploited to limit the inter-well domain. The empiric value provides an even closer limit for this domain. Thus, these tools can successfully be exploited for the design and description of bistable systems. This proves the efficiency of the developed criteria for DUFFING oscillator-like harvesters.

6.1.3. Bistable electromechanical beam

The experiments for the bistable electromechanical beam are also performed on the test rig presented in Section 6.1.1. The considered beams are similar to the bistable beam presented in Section 6.1.2, although two piezoceramic elements are symmetrically linked near the root of the beams. This position is chosen because it gives the highest strain. Thus, this leads to a high coupling

factor. Two different electromechanical beams are produced. The difference is only in the piezoelectric element types chosen. The first piezoelectric patch type (P-876.A12) from PI® has an element height of 0.2 mm and the second one (P-876.A15) of 0.5 mm. These different types were chosen to investigate the effect of the different coupling parameters. The beam with the piezoelectric element type P-876.A12 will be referred to as 'beam 1', and the beam with the element type P-876.A15 as 'beam 2'. The model for the electromechanical beam reads

$$\ddot{x}(t) + \mu\,\dot{x}(t) - \delta\,v(t) - \alpha\,x(t) + \beta\,x^3(t) = m_e\;\hat{e}\;\ddot{e}(t), \tag{6.2a}$$

$$\phi\,v(t) + \gamma\,\dot{x}(t) + \dot{v}(t) = 0. \tag{6.2b}$$

The equations suppose a coupling of the two piezoelectric elements. In this case, a series connection is chosen. The identified parameters are listed in Table 6.2 and 6.3. The mechanical parameters are identified similar to the parameters of the bistable beam. The coupling parameters δ and γ are obtained by exploiting the inverse piezoelectric effect. The capacity C_p is measured by a multimeter, where the conductance parameter ϕ is calculated by

$$\phi = \frac{1}{C_p R}. \tag{6.3}$$

The resistance R is adjusted by an resistance decade box.

Table 6.2: Experimentally identified parameters for beam 1

Parameter	Value	Unit
α	4750	$\frac{1}{\mathrm{s}^2}$
β	$90 \cdot 10^6$	$\frac{1}{\mathrm{s}^2\mathrm{m}^2}$
μ	1.1258	$\frac{1}{\mathrm{s}}$
m_e	1.0632	-
δ	0.0142	$\frac{\mathrm{As}}{\mathrm{kg}}$
γ	8596	$\frac{\mathrm{kg\ m}}{\mathrm{As}^3}$
C_p	$30.81 \cdot 10^{-9}$	$\frac{\mathrm{s}^4\mathrm{A}^2}{\mathrm{m}^2\mathrm{kg}}$

Parameter	Value	Unit
α	2975.3	$\frac{1}{s^2}$
β	$196.95 \cdot 10^6$	$\frac{1}{s^2 m^2}$
μ	1.4923	$\frac{1}{s}$
m_e	1.0632	-
δ	0.0094	$\frac{As}{kg}$
γ	22600	$\frac{kg\ m}{As^3}$
C_p	$19.07 \cdot 10^{-9}$	$\frac{s^4 A^2}{m^2 kg}$

Table 6.3: Experimentally identified parameters for beam 2

Fixed electrical resistance

In this section, measurements with a fixed resistance are carried out. This involves response maps for the dissipated mean power P_m (Eqn. 5.10) and the snap-through ratio Ψ (Eqn. 2.5). Figure 6.5 shows the response maps that were obtained experimentally for Ψ and the mean power P_m for the electromechanical beam 1. Figure 6.5a shows that the left edge of the inter-

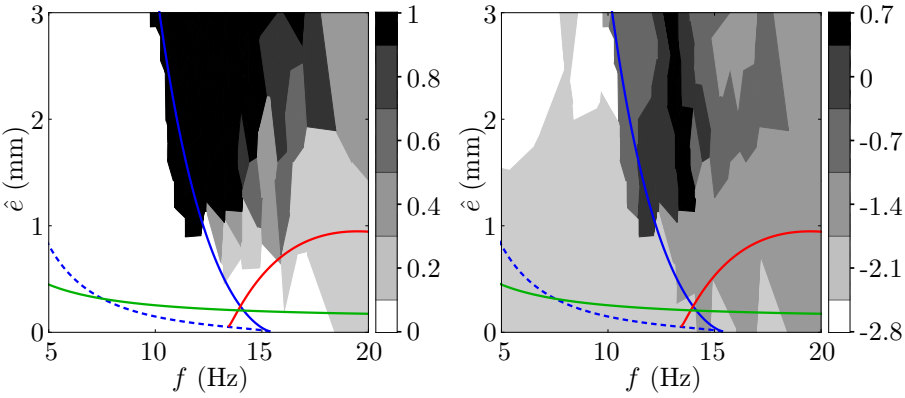

(a) Response map for Ψ $(-)$ **(b)** Response map for $\log P_m$

Figure 6.5.: Response maps for beam 1 ($R = 20$ kΩ) with the analytic criteria: lower b_{snL}(blue dashed) and upper (blue) saddle-node b_{snU} bifurcation, saddle-node bifurcation b_{snI} (green) and criterion for chaos (red).

well domain can be described by the upper saddle-node bifurcation value b_{snU}. Similar to the experiments with the bistable beam, the right diffuse edge is much steeper compared to numerical simulation. This can also be explained by the constraints of the model, as discussed in the previous section. Figure 6.5b shows the mean power P_m. As expected, the power shows a maximum within the inter-well domain. The graph shows that the harvested power is by magnitudes higher when the harvesting is performed while having inter-well oscillations. The decrease of P_m in the upper left corner of the graph can be explained with the optimal resistance, which will be discussed later. Figure 6.6 shows response maps for beam 2. Similar to the results for beam 1, the bifurcation value b_{snU} and the criterion for chaos limit the inter-well domain in an accurate way. The response map for the mean power P_m (Fig. 6.6b) exhibits the maximum within the inter-well domain, which agrees with the previous results. At this point, it has to be pointed out that the chosen resistance R is not optimal, thus the harvested power can be increased by choosing an appropriate resistance.

Considering the results of the perturbation calculus in Section 4.1.1, the

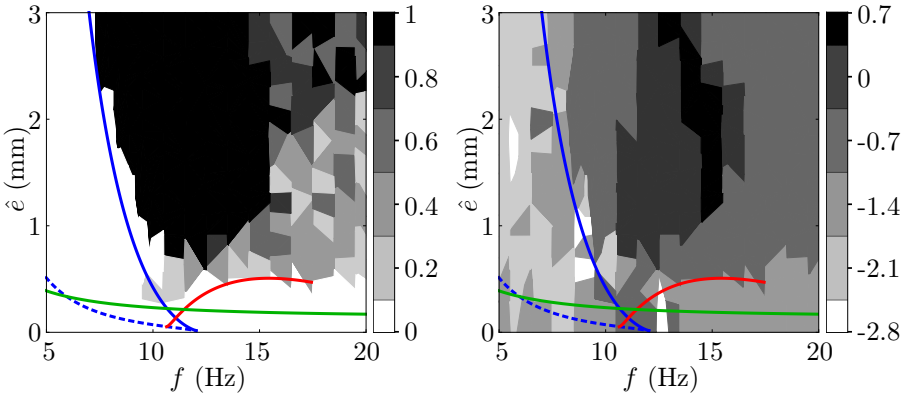

(a) Response map for Ψ $(-)$ **(b)** Response map for $\log P_m$

Figure 6.6.: Response maps for beam 2 ($R = 100$ kΩ) with the analytic criteria: lower b_{snL}(blue dashed) and upper (blue) saddle-node b_{snU} bifurcation, saddle-node bifurcation b_{snI} (green) and criterion for chaos (red).

effect of the electromechanical coupling can be considered by a frequency shift and an increased damping. This reduction allows to apply significantly more analytic criteria to describe the topology of an electromechanical system. The frequency shift and the effective damping are given by Eqns. (4.26 and 4.27). Figure 6.7 depicts a comparison of response maps for the snap-through ratio Ψ with the criteria of the reduced systems. The graphs show that this reduction leads to a proper result. The criteria limit the regions in an accurate way which suggests that this reduction is suitable for the simplification of an electromechanically coupled system. The advantage of the reduction is particularly useful since it gives the possibility to exploit the empiric criterion to describe the right edge of the inter-well domain. As illustrated in both graphs, the inter-well domains are limited in the best way by this criterion. This can be exploited for the analysis of the solution's topology.

The presented response maps are generated by keeping the initially introduced energy as small as possible. This refers to an initial condition starting within a stable equilibrium and zero velocity. In the experiment this is

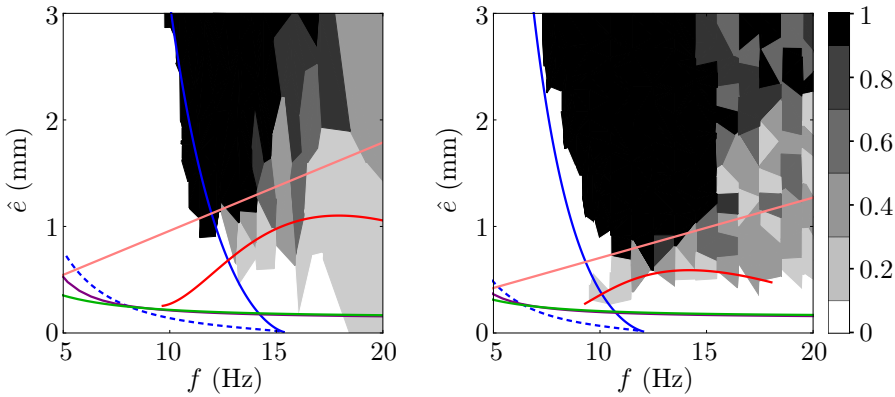

(a) Beam 1 **(b)** Beam 2

Figure 6.7.: Response maps for the two electromechanical beams with the analytic criteria for a reduced 1-DOF system: lower b_{snL}(blue dashed) and upper (blue) saddle-node b_{snU} bifurcation, saddle-node bifurcation b_{snI} (green), MELNIKOV function (purple), criterion for chaos (red) and the empiric criterion (pink)

achieved by perturbing the beam manually, aiming to lower the initial energy. Thus, the response maps shown can be compared with numerically obtained response maps with the initial conditions $x_0 = x_s$ and $\dot{x}_0 = 0$. In the following, the effect of different initial conditions is investigated. To do so, the system is again manually perturbed in order to achieve a high initial energy. This is done for various excitation parameters. The minimal excitation parameters for which inter-well oscillations appear can be regarded as the experimental bifurcation value b_{snI}. Figure 6.8 shows the response map for Ψ comparing the experimental (purple) and analytical (green) bifurcation value b_{snI}. The graph shows that the inter-well domain can largely be increased by changing the initial condition. These results equate the numerical results in Section 2.1.3. The comparison between the analytical and the experimental value shows a discrepancy. This is explained by the scattered attractor for inter-well oscillations. The scattered attractor shows a high sensitivity on the initial conditions. This leads to a large deviation between both bifurcation values, especially for low excitation frequencies, because it is difficult to obtain inter-well oscillations. This tendency can also be seen in Fig. 2.9b. With larger frequencies both values converge. To conclude, the experiments show that the measured inter-well domains (Fig. 6.7) are a conservative estimation. For real-world applications inter-well oscillations can be observed in an even larger domain which affects the energy harvest positively. This is also shown numerically in Section 2.1.3.

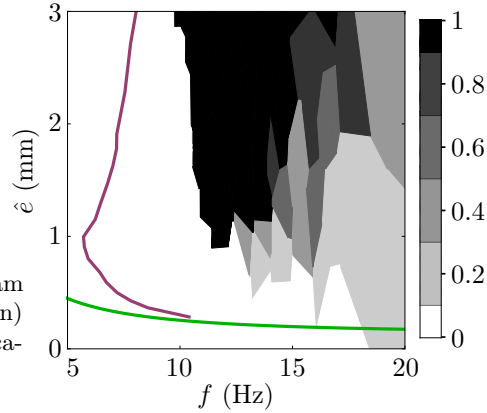

Figure 6.8: Response map for Ψ (beam 1) showing the analytical (green) and experimental (purple) bifurcation value b_{snI}

Variable electrical resistance

In this section the electromechanical beams are investigated regarding the optimal electrical resistance. In Section 5.2.1 it is illustrated that the resistance for nonlinear electromechanical systems differs a lot from the one of linear systems. This is in the following veryfied by experiments. For doing so, the piezoelectric elements are connected in series over a variable resistance R. Figure 6.9 shows the optimal resistance while having single-well oscillations for the electromechanical beam 1. The optimal parameter R is indicated by the vertical dashed line. When the frequency is fixed (Fig. 6.9a), the optimal resistance does not change substantially. A slightly higher change in R_{opt} can be seen when the excitation frequency is changed while maintaining the excitation amplitude. However, due to the slight change in the frequencies, the difference for the optimal parameter R is only small. For the second

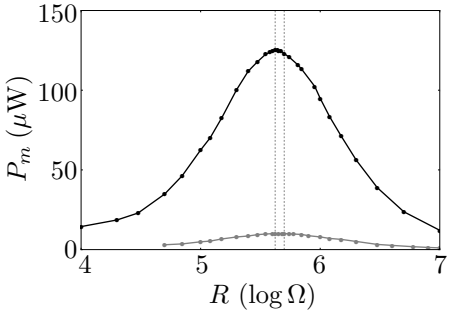

(a) Fixed frequency $f = 8.5$ Hz: the gray line corresponds to $\hat{e} = 0.88$ mm and black to $\hat{e} = 3.19$ mm

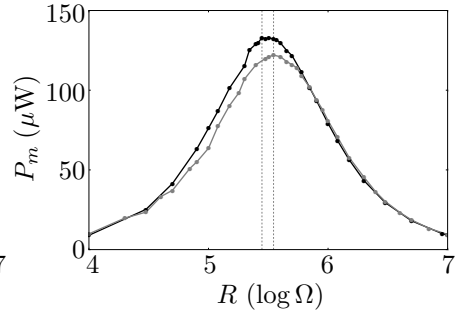

(b) Fixed amplitude $\hat{e} = 0.73$ mm: the gray line corresponds to $f = 10.7$ Hz and black to $f = 12.7$ Hz

Figure 6.9.: Influence of the excitation frequency and amplitude on the optimal resistance R for single-well oscillations (beam 1)

beam with a higher coupling (Fig. 6.10) the change in R_{opt} is still small when the excitation amplitude is increased. Even though, the amplitude is increased more than four times, the difference in the optimal resistance stays small (Fig. 6.12a). Figure 6.12b indicates that an altered frequency f influences the optimal resistance more than the excitation amplitude $\hat{e}$. This is

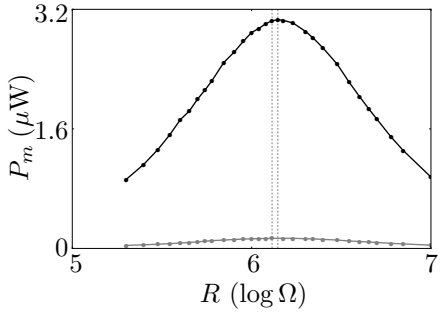

(a) Fixed frequency $f = 5.25$ Hz: the gray line corresponds to $\hat{e} = 0.78$ mm and black to $\hat{e} = 3.57$ mm

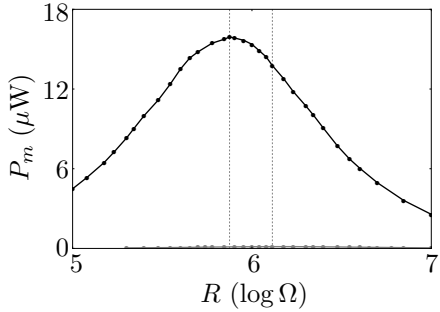

(b) Fixed amplitude $\hat{e} = 0.78$ mm: the gray line corresponds to $f = 5.25$ Hz and black to $f = 10.34$ Hz

Figure 6.10.: Influence of the excitation frequency and amplitude on the optimal resistance for single-well oscillations (beam 2)

in accordance with the numerical results depicted in Fig. 5.12. Figures 6.11 and 6.12 show the mean power P_m over the resistance R. Interestingly, for a modified excitation amplitude $\hat{e}$ both beams do not show any difference in the parameter R_{opt}. Moreover, if the frequency is changed (Fig. 6.11b), the

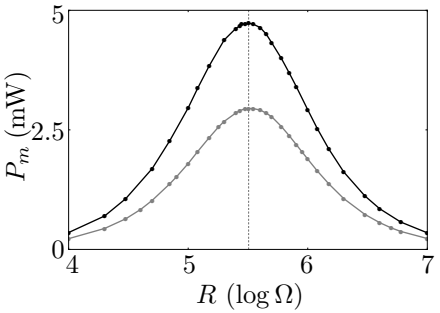

(a) Fixed frequency $f = 9.6$ Hz: the gray line corresponds to $\hat{e} = 0.3$ mm and black to $\hat{e} = 3$ mm

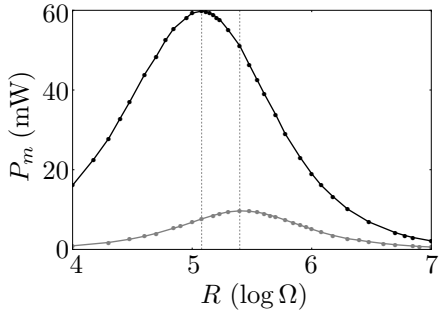

(b) Fixed amplitude $\hat{e} = 0.73$ mm: the gray line corresponds to $f = 10.7$ Hz and black to $f = 13.4$ Hz

Figure 6.11.: Influence of the excitation frequency and amplitude on the optimal resistance for inter-well oscillations (beam 1)

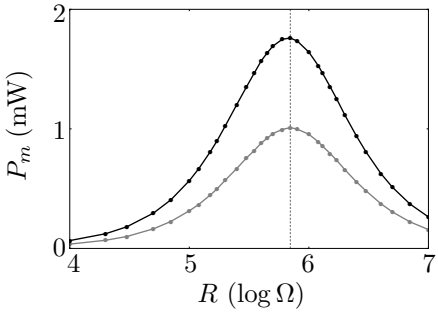

(a) Fixed frequency $f = 9.4$ Hz: the gray line corresponds to $\hat{e} = 0.26$ mm and black to $\hat{e} = 3.6$ mm

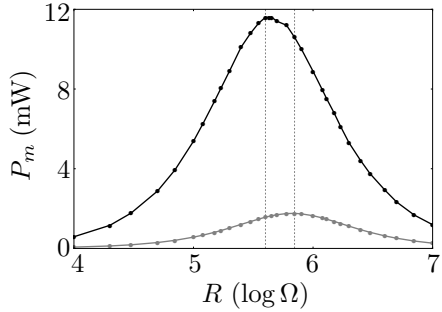

(b) Fixed amplitude $\hat{e} = 3.6$ mm: the gray line corresponds to $f = 9.4$ Hz and black to $f = 11.8$ Hz

Figure 6.12.: Influence of the excitation frequency and amplitude on the optimal resistance for inter-well oscillations (beam 2)

optimal resistance changes significantly, even though the change in f is quite small. The deviation is about 130 kΩ while the frequency changed by 2.7 Hz. For beam 2 with the higher coupling this deviation increases even more. Figure 6.12b shows that the optimal resistance changes by 300 kΩ even though the excitation frequency is only changed by 2.4 Hz. These findings affirm

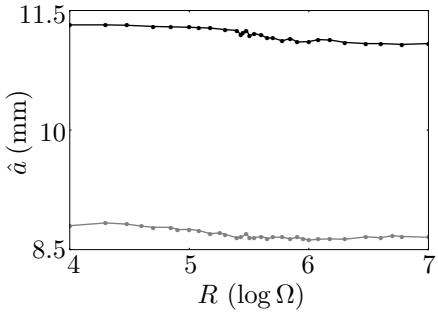

(a) Fixed frequency $f = 9.6$ Hz: the gray line corresponds to $\hat{e} = 0.34$ mm and black to $\hat{e} = 3$ mm (beam 1)

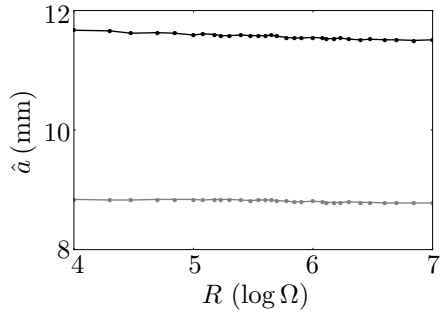

(b) Fixed frequency $f = 9.4$ Hz: the gray line corresponds to $\hat{e} = 0.26$ mm and black to $\hat{e} = 3.6$ mm (beam 2)

Figure 6.13.: Oscillation amplitude $\hat{a}$ over the resistance R for inter-well oscillations

the numerical findings, where the optimal resistance for inter-well oscillations is much more sensitive to changes in the excitation parameters compared to single-well oscillations.

Figure 6.13 shows the amplitude $\hat{a}$ over the resistance R. Both graph show how the introduced electrical damping leads to a decrease of the oscillation amplitude, even though the reduction is marginal. However, this illustrates the electromechanical feedback of the electrical circuit on the mechanical structure.

6.2. Composite plate

This section presents a short experimental analysis of an electromechanical composite plate. To focus is on the solution's topology and not the produced voltage.

6.2.1. Experimental setup

The model of such a plate is derived in Section 5.4. The composite plate is mounted on a different test rig. Figure 6.14 shows the experimental setup. A bistable composite plate is mounted on a shaker. A laser triangulation sensor measures the excitation at the mounting. The deflection of the plate

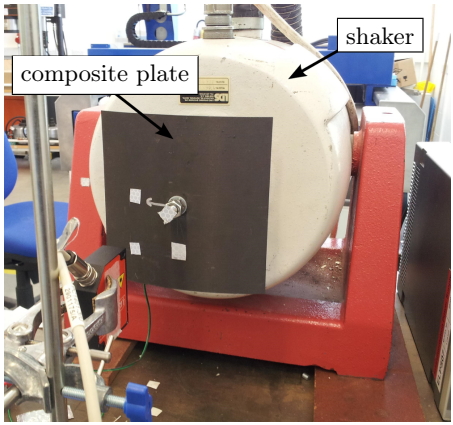

Figure 6.14: Experimental setup for the composite plate

is captured by a laser DOPPLER[1] vibrometer at one point. The measurement point is near a corner of the plate. This means that both degrees of freedom are captured in sum. Contrary to the investigations of a beam, this involves some difficulties. On the first hand, the identification of the parameters is challenging because more parameters are necessary to describe the system (Eqn. 3.111). This hinders a experimental parameter identification. Thus, the analytical model (Eqn. 3.108) can be considered to identify the parameters. Here, a difficulty arises. The measured temperature difference ΔT between curing and operation causes the model to give highly different values compared to the expected ones. This is justified by the production of the composite plate. Usually the temperature gradient ΔT is determined by the difference between the operating and the curing temperature. However, the real temperature difference ΔT needs to be measured between gel point and operating temperature. The considered composite plate is made by pre-impregnated composite fibers (pre-preg), thus the gel point depends on the history of the prepreg. Thus, the temperature gradient ΔT is accompanied by a high uncertainty. On the other hand, it is difficult to obtain the system parameters by only measuring at one point. Both points mentioned reveal the challenges for accurate experiments with a composite plate. A further difficulty for the experiment is the asymmetry which cannot easily be adjusted compared with the beam.

6.2.2. Experimental results

Analogously to the beam a response map is generated. It needs to be pointed out that it was difficult to distinguish between cross-well and inter-well oscillations from the measured time data. This is die to the reduced information for both degree of freedoms within one signal. Another reason is given by the phenomenon of global inter-well oscillations. This is discussed in Section 5.4. However, it is possible to identify the main features of a composite plate. Figure 6.15 shows the measured response map. In this map only two domains can be identified. The white domain indicates single-well oscillations. The black

[1] Christian Andreas Doppler (1803-1853), Austrian mathematician and physicist

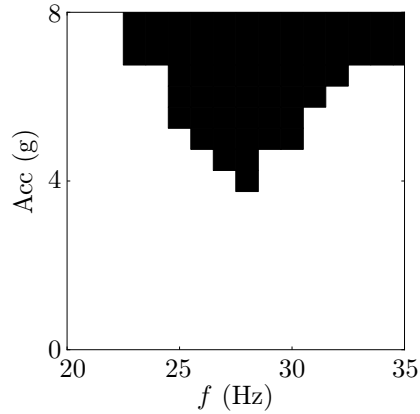

Figure 6.15: Response map for the composite plate

domain indicates a region where snap-throughs are found. Due to the reasons mentioned, with the experimental setup no distinction between cross-well and inter-well oscillations is possible. However, the main features can be identfied. The sharp right edge is seen in the graph. It is also observed that the ratio of snap-throughs within the time signal decreased near the right edge of the snap-through domain. This agrees with the numerical findings even though it is not noticeable in the graph.

The experiment on the electromechanical composite plate shows the occuring challenges for energy harvesters based on composite plates. A first issue is the precise determination of the temperature gradient ΔT. The system parameters are very sensitive to this parameter, thus a precise determination and design of the temperature gradient ΔT is crucial. This also affects the operation temperature. A variable operating temperature might change the system's characteristics enormously. A second issue is the asymmetry which is difficult to adjust. This also needs to be considered in the design of such an energy harvester. Moreover, a comparison with the analytic criteria (Chapter 4) is still pending.

7. Conclusion

This thesis investigates different multistable energy harvester designs. The field of energy harvesting aims to transform ambient energy into electrical energy. For example, this energy can be used to operate autonomous sensor units for structural health monitoring or to supply smart structures. Smart structures permit to employ new materials and technologies helping to increase safety, performance and reliability. For these applications, robust energy harvesters that allow to harvest sufficient energy over a broad frequency range are crucial. In this context multistable energy harvesters offer promising features.

The aim of this thesis is to analyze different energy harvester designs in order to optimize their performance and formulate design criteria. Chapter 1 provides overview over the research activities in the field of energy harvesting. A introduction to vibrational energy harvesting with focus on multistable structures is given in Chapter 2. Chapter 3 presents the different analytical harvester models. In the first step, the model of a prestressed bistable beam is introduced as is exhibits the main features of any multistable system. Subsequently, a model describing a bistable electromechanical beam is presented. This model is given by a nonlinear differential equation of second order for the mechanical characteristics coupled with a linear differential equation of first order for the electric circuit. The analytical model of a composite plate, described by two equations, is established subsequently. This model allows to investigate the mechanical characteristics of energy harvesters exploiting structural bistability by composite plates. In the following, the model of an electromechanical composite plate is introduced. This model presents the second design of an energy harvester. It is given by a minimum of three coupled nonlinear equations. Finally, the chapter introduces a model of a multistable plate in order to analyze the potential of structures with more than two equilibria.

Since multistable energy harvesters are described by nonlinear equations, the majority of research works are done numerically or experimentally. However, for the fundamental understanding and characterization of the different energy harvester designs an analytic description is inalienable. Thus, Chapter 4 introduces the framework of analytical methods that are applied to the different models. The framework includes methods like the commonly used multiple scales and the harmonic balance method. Closed-form expressions describing the bifurcation behavior for the considered systems are formulated using these methods. Furthermore, an empiric criterion which helps to describe the solution's topology of a bistable DUFFING oscillator in an accurate manner is developed.

In Chapter 5, the different systems are analyzed. It is shown that the bistable prestressed beam exhibits the main features of any multistable system. The numerical simulations reveal that the continuous snap-through oscillations between the two equilibria (inter-well oscillations) enhance the efficiency and broadband capacities of these energy harvesters compared to monostable linear or nonlinear systems. A comparison between the numerical simulations and the analytical bifurcation values illustrates a good correspondence. Thus, these methods provide a powerful tool for the description of the solution's topology to design an energy harvester when the excitation parameters are known. For example, the analytic methods limit the favorable inter-well domain for the different energy harvester designs. This analytic description can be exploited to design the system accordingly. In order to show the general behavior of bistable systems, a reduction of simple bistable energy harvesters into a single equation is performed and compared with numerical results. This reduction extends the number of the applicable analytical methods for bistable energy harvesters. Chapter 5 also highlights the difference between bistable systems such as a prestressed beam and a bistable composite plate. Both structures posses similar topologies for the solution while showing considerable differences concerning robustness. Simple bistable oscillators possess a broad bandwidth for inter-well oscillations, while the bistable composite plate shows, if at all, only a narrow inter-well domain. The implications resulting from this major difference for energy harvesting are presented.

A possibility of enhancing the broadband capabilities of multistable structures is presented by means of the multistable plate. It is shown that a structure exhibiting four equilibria exhibits inter-well oscillations over a broader frequency range. This is achieved by a separation of the eigenfrequencies within the equilibria. A short study on combined harmonic and noise excitation concludes this chapter. This study reveals that additional noise improves the energy harvesting capabilities by increasing the inter-well domain for DUFFING oscillator-like harvesters.

In order to demonstrate the transferability and validity of the derived analytic criteria for real-world applications experiments are performed. These results are presented in Chapter 6. The first experiment considers a bistable prestressed beam. It is proven that the analytic criteria conform well to the experimental measurements. Furthermore, the significance of the developed empiric criterion is verified. Experiments with bistable electromechanical beams also show a good agreement between analytical criteria and experiments. Moreover, the influence of the initial conditions investigated in order to demonstrate the conservative character of the analytical criteria and to validate the numerical findings. In addition, the constraints of the applied model order is shown by means of experiments. Nonetheless, the experiments stress the validity and significance of the analytical criteria for the design and characterization of bistable energy harvesters. The chapter closes with an experiment with a bistable electromechanical composite plate. The results point out that the solution's topology is preserved in the experiment. However, the composite plate also illustrates the drawback of such structures concerning robustness, e.g. sensitivity of the system parameters on the operating temperature.

The presented results suggest to expand the comparison between the different underlying mechanical structures. The findings show that there are significant differences concerning the performance even though in the literature they are considered to be equivalent [28, 55]. Thus, a comparison of these structures concerning the robustness in real environmental conditions such as temperature, moisture, excitation and durability and the energy harvesting density provides a possible outlook. Another issue for further research

offers the miniaturization of the presented energy harvester designs. This is a requirement for a successful and widespread application especially in the field of mechanical structures. In this thesis the energy is dissipated by an electrical resistance. However, to maximize the efficiency of the harvester several circuit designs e.g. switching shunts [29, 79] are proposed. The resulting electromechanical interaction might affect the solution's topology. This demands further consideration on the route to a widespread implementation of multistable energy harvesters.

Bibliography

[1] Adhikari, S.; Friswell, M.I.; Inman, D.J.: Piezoelectric energy harvesting from broadband random vibrations, *Smart Materials and Structures*, 18(11):115005, 2009.

[2] Airbus (Editor): *FAST: Airbus technical magazine*, 54, 2014.

[3] Al-Ashtari, W.; Hunstig, M.; Hemsel, T.; Sextro, W.: Frequency tuning of piezoelectric energy harvesters by magnetic force, *Smart Materials and Structures*, 21(3):35019, 2012.

[4] American National Standards Institute.: *IEEE standard on piezoelectricity : an American national standard*, Institute of Electrical and Electronics Engineers, New York N.Y, 1988.

[5] Andrews, D.L.: *Energy harvesting materials*, World Scientific Pub. Co., Singapore and Hackensack, NJ, 2005.

[6] Aridogan, U.; Basdogan, I.; Erturk, A.: Analytical modeling and experimental validation of a structurally integrated piezoelectric energy harvester on a thin plate, *Smart Materials and Structures*, 23(4):45039, 2014.

[7] Arrieta, A.F.; Delpero, T.; Bergamini, A.E.; Ermanni, P.: Broadband vibration energy harvesting based on cantilevered piezoelectric bi-stable composites, *Applied Physics Letters*, 102(17):173904, 2013.

[8] Arrieta, A.F.; Hagedorn, P.; Erturk, A.; Inman, D.J.: A piezoelectric bistable plate for nonlinear broadband energy harvesting, *Applied Physics Letters*, 97(10):104102, 2010.

[9] Arrieta, A.F.; Wagg, D.J.; Neild, S.A.: Dynamic Snap-through for Morphing of Bi-stable Composite Plates, *Journal of Intelligent Material Systems and Structures*, 22(2):103–112, 2011.

[10] Arrieta, A.F.; Hagedorn, P.; Erturk, A.; Inman, D.J.: Electromechanical Modelling and Experiments of a Bistable Plate for Nonlinear Energy Harvesting, *ASME 2010 Conference on Smart Materials, Adaptive*

Structures and Intelligent Systems, pp. 487–494, September 28–October 1, 2010.

[11] Arrieta, A.F.; Neild, S.A.; Wagg, D.J.: On the cross-well dynamics of a bi-stable composite plate, *Journal of Sound and Vibration*, 330(14):3424–3441, 2011.

[12] Atanacković, T.M.; Guran, A.: *Theory of elasticity for scientists and engineers*, Birkhäuser, Boston, 2000.

[13] Barton, D.A.W.; Burrow, S.G.; Clare, L.R.: Energy Harvesting From Vibrations With a Nonlinear Oscillator, *Journal of Vibration and Acoustics*, 132(2):21009, 2010.

[14] Beeby, S.P.; Tudor, M.J.; White, N.M.: Energy harvesting vibration sources for microsystems applications, *Measurement Science and Technology*, 17(12):R175–R195, 2006.

[15] Beeby, S.P.; White, N.: *Energy harvesting for autonomous systems*, Artech House series smart materials, structures, and systems, Artech House, Norwood, Mass., 2010.

[16] Beeby, S.P.; Wang, L.; Zhu, D.; Weddell, A.S.; Merrett, G.V.; Stark, B.; Szarka, G.; Al-Hashimi, B.M.: A comparison of power output from linear and nonlinear kinetic energy harvesters using real vibration data, *Smart Materials and Structures*, 22(7):75022, 2013.

[17] Betts, D.N.; Kim, H.A.; Bowen, C.R.; Inman, D.J.: Optimal configurations of bistable piezo-composites for energy harvesting, *Applied Physics Letters*, 100(11):114104, 2012.

[18] Betts, D.N.; Guyer, R.A.; Le Bas, P.Y.; Bowen, C.R.; Inman, D.; Kim, H.A.: Modelling the Dynamic Response of Bistable Composite Plates for Piezoelectric Energy Harvesting, *55th AIAA/ASMe/ASCE/AHS/SC Structures, Structural Dynamics, and Materials Conference*.

[19] Betts, D.N.; Kim, H.; Bowen, C.; Inman, D.: Static and Dynamic Analysis of Bistable Piezoelectric-Composite Plates for Energy Harvesting, *53rd AIAA/ASME/ASCE/AHS/ASC Structures, Structural Dynamics and Materials Conference
20th AIAA/ASME/AHS Adaptive Structures Conference
14th AIAA*.

[20] Borowiec, M.; Litak, G.; Friswell, M.I.; Ali, S.F.; Adhikari, S.; Lees, A.W.; Bilgen, O.: Energy Harvesting in Piezoelastic Systems Driven by Random Excitations, *International Journal of Structural Stability and Dynamics*, 13(07):1340006, 2013.

[21] Cammarano, A.; Burrow, S.G.; Barton, D A W; Carrella, A.; Clare, L.R.: Tuning a resonant energy harvester using a generalized electrical load, *Smart Materials and Structures*, 19(5):55003, 2010.

[22] Challa, V.R.; Prasad, M.G.; Shi, Y.; Fisher, F.T.: A vibration energy harvesting device with bidirectional resonance frequency tunability, *Smart Materials and Structures*, 17(1):15035, 2008.

[23] Chicone, C.C.: *Ordinary differential equations with applications*, volume 34 of *Texts in applied mathematics*, Springer, New York and Berlin, 2006, 2nd ed. edition.

[24] Cottone, F.; Gammaitoni, L.; Vocca, H.; Ferrari, M.; Ferrari, V.: Piezoelectric buckled beams for random vibration energy harvesting, *Smart Materials and Structures*, 21(3):35021, 2012.

[25] Cottone, F.; Vocca, H.; Gammaitoni, L.: Nonlinear Energy Harvesting, *Physical Review Letters*, 102(8), 2009.

[26] Dano, M.L.; Hyer, M.W.: Thermally-induced deformation behavior of unsymmetric laminates, *International Journal of Solids and Structures*, 35(17):2101–2120, 1998.

[27] Daqaq, M.F.: Response of uni-modal duffing-type harvesters to random forced excitations, *Journal of Sound and Vibration*, 329(18):3621–3631, 2010.

[28] Daqaq, M.F.; Masana, R.; Erturk, A.; Dane Quinn, D.: On the Role of Nonlinearities in Vibratory Energy Harvesting: A Critical Review and Discussion, *Applied Mechanics Reviews*, 66(4):40801, 2014.

[29] Delpero, T.; Di Lillo, L.; Bergamini, A.E.; Ermanni, P.: Energy harvesting module for the improvement of the damping performance of autonomous synchronized switching on inductance, *Journal of Intelligent Material Systems and Structures*, 24(7):837–845, 2013.

[30] Diaconu, C.G.; Weaver, P.M.; Arrieta, A.F.: Dynamic analysis of bistable composite plates, *Journal of Sound and Vibration*, 322(4-5):987–1004, 2009.

[31] Duffing, G.: *Erzwungene Schwingungen bei veränderlicher Eigenfrequenz und ihre technische Bedeutung*, Sammlung Vieweg, F. Vieweg & Sohn, 1918.

[32] Elvin, N.; Erturk, A.: *Advances in Energy Harvesting Methods*, Springer New York, New York, NY, 2013.

[33] Emam, S.A.: A theoretical and experimental study of nonlinear dynamics of buckled beams, 2002.

[34] Erturk, A.; Hoffmann, J.; Inman, D.J.: A piezomagnetoelastic structure for broadband vibration energy harvesting, *Applied Physics Letters*, 94(25):254102, 2009.

[35] Erturk, A.; Inman, D.: Broadband piezoelectric power generation on high-energy orbits of the bistable Duffing oscillator with electromechanical coupling, *Journal of Sound and Vibration*, 330(10):2339–2353, 2011.

[36] Erturk, A.; Inman, D.J.: *Piezoelectric energy harvesting*, Wiley, Chichester, West Sussex, U.K. and Hoboken, N.J., 2011.

[37] Fenner, R.T.; Reddy, J.N.: *Mechanics of solids and structures*, Computational mechanics and applied analysis, CRC Press/Taylor & Francis Group, Boca Raton, 2012, second ed. edition.

[38] Ferrari, M.; Ferrari, V.; Guizzetti, M.; Andò, B.; Baglio, S.; Trigona, C.: Improved energy harvesting from wideband vibrations by nonlinear piezoelectric converters, *Sensors and Actuators A: Physical*, 162(2):425–431, 2010.

[39] Foisal, A.R.M.; Hong, C.; Chung, G.S.: Multi-frequency electromagnetic energy harvester using a magnetic spring cantilever, *Sensors and Actuators A: Physical*, 182:106–113, 2012.

[40] Friswell, M.I.; Ali, S.F.; Bilgen, O.; Adhikari, S.; Lees, A.W.; Litak, G.: Non-linear piezoelectric vibration energy harvesting from a vertical cantilever beam with tip mass, *Journal of Intelligent Material Systems and Structures*, 23(13):1505–1521, 2012.

[41] Gammaitoni, L.; Neri, I.; Vocca, H.: Nonlinear oscillators for vibration energy harvesting, *Applied Physics Letters*, 94(16):164102, 2009.

[42] Gibson, R.F.: *Principles of composite material mechanics*, McGraw-Hill series in aeronautical and aerospace engineering, McGraw-Hill, New York, 1994.

[43] Gilbert, J.M.; Balouchi, F.: Comparison of energy harvesting systems for wireless sensor networks, *International Journal of Automation and Computing*, 5(4):334–347, 2008.

[44] Gilmore, R.; McCallum, J. W. L.: Structure in the bifurcation diagram of the Duffing oscillator, *Physical Review E*, 51(2):935–956, 1995.

[45] Giurgiutiu, V.; Soutis, C.: Enhanced Composites Integrity Through Structural Health Monitoring, *Applied Composite Materials*, 19(5):813–829, 2012.

[46] Gladwell, G.M.L.; Preumont, A. (Editors): *Vibration Control of Active Structures*, Solid Mechanics and Its Applications, Springer Netherlands, Dordrecht, 2011.

[47] Goldstein, H.: *Classical mechanics*, World student series, Addison-Wesley Pub. Co., Reading, Mass., 1980, 2d ed. edition.

[48] Grinberg, I.; Gendelman, O.V.: Boundary for Complete Set of Attractors for Forced–Damped Essentially Nonlinear Systems, *Journal of Applied Mechanics*, 82(5):51004, 2015.

[49] Gu, L.; Livermore, C.: Impact-driven, frequency up-converting coupled vibration energy harvesting device for low frequency operation, *Smart Materials and Structures*, 20(4):45004, 2011.

[50] Guckenheimer, J.; Holmes, P.: *Nonlinear Oscillations, Dynamical Systems, and Bifurcations of Vector Fields*, SpringerLink : Bücher, Springer, New York, NY, 1983.

[51] Hagedorn, P.: *Non-linear oscillations*, volume 10 of *The Oxford engineering science series*, Clarendon Pr, Oxford u.a, 1988, 2 edition.

[52] Hagedorn, P.: *Technische Schwingungslehre*, Springer, Berlin and Heidelberg and New York and London and Paris and Tokyo, 1989.

[53] Halvorsen, E.: Fundamental issues in nonlinear wideband-vibration energy harvesting, *Physical Review E*, 87(4), 2013.

[54] Harne, R.L.; Thota, M.; Wang, K.W.: Concise and high-fidelity predictive criteria for maximizing performance and robustness of bistable energy harvesters, *Applied Physics Letters*, 102(5):53903, 2013.

[55] Harne, R.L.; Wang, K.W.: A review of the recent research on vibration energy harvesting via bistable systems, *Smart Materials and Structures*, 22(2):23001, 2013.

[56] Heffel, E.: *Ultrasonic generators for energy harvesting applications: Self-excitation and mechanical frequency transformation*, volume Bd. 32 of *Forschungsbericht / Studienbereich Mechanik, Technische Universität Darmstadt*, Techn. Univ., Studienbereich Mechanik, Darmstadt, 2013.

[57] Hochlenert, D.: *Normalformen und Einzugsbereiche nichtlinearer dynamischer Systeme: Beispiele und technische Anwendungen*, Habilitation, TU Berlin, 2012.

[58] Hodges, D.H.: Proper definition of curvature in nonlinear beam kinematics, *AIAA journal*, 22(12):1825–1827, 1984.

[59] Hoffmann, K.: *Mathematische Modellierung*, Mathematik Kompakt, Birkhäuser, Basel, 2009, 1. aufl. edition.

[60] Holmes, P.: A Nonlinear Oscillator with a Strange Attractor, *Philosophical Transactions of the Royal Society A: Mathematical, Physical and Engineering Sciences*, 292(1394):419–448, 1979.

[61] Hsu, J.C.; Tseng, C.T.; Chen, Y.S.: Analysis and experiment of self-frequency-tuning piezoelectric energy harvesters for rotational motion, *Smart Materials and Structures*, 23(7):75013, 2014.

[62] Hyer, M.W.: The Room-Temperature Shapes of Four-Layer Unsymmetric Cross-Ply Laminates, *Journal of Composite Materials*, 16(4):318–340, 1982.

[63] Hyer, M.W.: Calculation of the room-temperature shapes of unsymmetric laminates, 1981.

[64] Isermann, R.; Munchhof, M.: *Identification of dynamical systems: An introduction with applications*, Advanced textbooks in control and signal processing, Springer, Berlin and London, 2011.

[65] Janocha, H.: *Adaptronics and smart structures: Basics, materials, design, and applications*, Springer, Berlin and New York, 2007, 2nd, rev. ed. edition.

[66] Jiang, W.A.; Chen, L.Q.: Snap-through piezoelectric energy harvesting, *Journal of Sound and Vibration*, 333(18):4314–4325, 2014.

[67] Jones, R.M.: Buckling and vibration of unsymmetrically laminated cross-ply rectangular plates, *AIAA journal*, 11(12):1626–1632, 1973.

[68] Jones, R.M.: *Mechanics of composite materials*, Taylor & Francis, Philadelphia, PA, ©1999, 2 edition.

[69] Jung, S.M.; Yun, K.S.: Energy-harvesting device with mechanical frequency-up conversion mechanism for increased power efficiency and wideband operation, *Applied Physics Letters*, 96(11):111906, 2010.

[70] Kai-Dietrich Wolf: *Electromechanical Energy Conversion in Asymmetric Piezoelectric Bending Actuators*, Ph.D. thesis, TU Darmstadt, 2001.

[71] Kapitaniak, T.: *Chaos for engineers: Theory, applications, and control*, Springer Verlag, Berlin and New York, 1998.

[72] Kaźmierski, T.J.; Beeby, S.: *Energy harvesting systems: Principles, modeling and applications*, Springer, New York, 2011.

[73] Kerschen, G.: *Nonlinear Dynamics, Volume 2*, Springer International Publishing, Cham, 2014.

[74] Kim, I.H.; Jung, H.J.; Lee, B.M.; Jang, S.J.: Broadband energy-harvesting using a two degree-of-freedom vibrating body, *Applied Physics Letters*, 98(21):214102, 2011.

[75] Kovacic, I.; Brennan, M.: *The Duffing Equation: Nonlinear Oscillators and their Behaviour*, Wiley, 2011.

[76] Kurths, J.; Boccaletti, S.; Grebogi, C.; Lai, Y.C.: Introduction: Control and synchronization in chaotic dynamical systems, *Chaos: An Interdisciplinary Journal of Nonlinear Science*, 13(1):126, 2003.

[77] Kyriazoglou, C.; Guild, F.: Finite element prediction of damping of composite GFRP and CFRP laminates – a hybrid formulation – vibration damping experiments and Rayleigh damping, *Composites Science and Technology*, 66(3-4):487–498, 2006.

[78] Leadenham, S.; Erturk, A.: M-shaped asymmetric nonlinear oscillator for broadband vibration energy harvesting: Harmonic balance analysis and experimental validation, *Journal of Sound and Vibration*, 333(23):6209–6223, 2014.

[79] Lefeuvre, E.; Badel, A.; Richard, C.; Petit, L.; Guyomar, D.: A comparison between several vibration-powered piezoelectric generators for standalone systems, *Sensors and Actuators A: Physical*, 126(2):405–416, 2006.

[80] Lequeux, J. (Editor): *Le Verrier—Magnificent and Detestable Astronomer*, Astrophysics and Space Science Library, Springer New York, New York, NY, 2013.

[81] Lin, H.C.; Wu, P.H.; Lien, I.C.; Shu, Y.C.: Analysis of an array of piezoelectric energy harvesters connected in series, *Smart Materials and Structures*, 22(9):94026, 2013.

[82] Litak, G.; Friswell, M.I.; Adhikari, S.: Magnetopiezoelastic energy harvesting driven by random excitations, *Applied Physics Letters*, 96(21):214103, 2010.

[83] Liu, H.; Lee, C.; Kobayashi, T.; Tay, C.J.; Quan, C.: Investigation of a MEMS piezoelectric energy harvester system with a frequency-widened-bandwidth mechanism introduced by mechanical stoppers, *Smart Materials and Structures*, 21(3):35005, 2012.

[84] Lo, K.H.; Christensen, R.M.; Wu, E.M.: A high-order theory of plate deformation—part 2: laminated plates, *Journal of Applied Mechanics*, 44(4):669–676, 1977.

[85] Mann, B.P.: Discussion: "On the Role of Nonlinearities in Vibratory Energy Harvesting: A Critical Review and Discussion" (Daqaq, M., Masana, R., Erturk, A., and Dane Quinn, D., 2014, ASME Appl. Mech. Rev., 66(4), p. 040801), *Applied Mechanics Reviews*, 66(4):45501, 2014.

[86] Mann, B.P.; Owens, B.A.: Investigations of a nonlinear energy harvester with a bistable potential well, *Journal of Sound and Vibration*, 329(9):1215–1226, 2010.

[87] Marinkovic, D.; Koppe, H.; Gabbert, U.: Accurate Modeling of the Electric Field within Piezoelectric Layers for Active Composite Structures,

Journal of Intelligent Material Systems and Structures, 18(5):503–513, 2006.

[88] Markert, R.: *Strukturdynamik: Skript zur Vorlesung "Strukturdynamik für Maschinenbauer"*, Techn. Univ., Fachgebiet Strukturdynamik, Darmstadt, 2011, 2011, 1., verb. aufl. edition.

[89] Masana, R.; Daqaq, M.F.: Electromechanical Modeling and Nonlinear Analysis of Axially Loaded Energy Harvesters, *Journal of Vibration and Acoustics*, 133(1):11007, 2011.

[90] McInnes, C.R.; Gorman, D.G.; Cartmell, M.P.: Enhanced vibrational energy harvesting using nonlinear stochastic resonance, *Journal of Sound and Vibration*, 318(4-5):655–662, 2008.

[91] Metzler, W.: *Nichtlineare Dynamik und Chaos: Eine Einführung*, Teubner-Studienbücher : Mathematik, Teubner, Stuttgart and Leipzig, 1998.

[92] Murdock, J.A.: *Normal forms and unfoldings for local dynamical systems*, Springer monographs in mathematics, Springer, New York, 2003.

[93] Nayfeh, A.H.; Emam, S.A.: Exact solution and stability of postbuckling configurations of beams, *Nonlinear Dynamics*, 54(4):395–408, 2008.

[94] Nayfeh, A.H.: *Perturbation methods*, Pure and applied mathematics, Wiley, New York, 1973.

[95] Nayfeh, A.H.; Mook, D.T.: *Nonlinear oscillations*, Physics textbook, Wiley, Weinheim, 2007.

[96] Ouakad, H.M.; Younis, M.I.: On using the dynamic snap-through motion of MEMS initially curved microbeams for filtering applications, *Journal of Sound and Vibration*, 333(2):555–568, 2014.

[97] Panyam, M.; Masana, R.; Daqaq, M.F.: On approximating the effective bandwidth of bi-stable energy harvesters, *International Journal of Non-Linear Mechanics*, 67:153–163, 2014.

[98] Penella-López, M.T.; Gasulla-Forner, M.: *Powering Autonomous Sensors*, Springer Netherlands, Dordrecht, 2011.

[99] Quinn, D.D.; Triplett, A.L.; Bergman, L.A.; Vakakis, A.F.: Comparing Linear and Essentially Nonlinear Vibration-Based Energy Harvesting, *Journal of Vibration and Acoustics*, 133(1):11001, 2011.

[100] Ramlan, R.; Brennan, M.J.; Mace, B.R.; Kovacic, I.: Potential benefits of a non-linear stiffness in an energy harvesting device, *Nonlinear Dynamics*, 59(4):545–558, 2010.

[101] Rao, S.S.: *Vibration of continuous systems*, Wiley, Hoboken, N.J., 2007.

[102] Reddy, J.N.: *Theory and analysis of elastic plates and shells*, CRC and Taylor & Francis [distributor], Boca Raton, Fla. and London, 2006, 2nd ed. edition.

[103] Roundy, S.; Wright, P.K.; Rabaey, J.: A study of low level vibrations as a power source for wireless sensor nodes, *Computer Communications*, 26(11):1131–1144, 2003.

[104] Seydel, R.: *Practical bifurcation and stability analysis*, volume v. 5 of *Interdisciplinary applied mathematics*, Springer, New York, 2010, 3rd ed. edition.

[105] Smith, R.C.: *Smart material systems: Model development*, volume 32 of *Frontiers in applied mathematics*, Society for Industrial and Applied Mathematics (SIAM, 3600 Market Street, Floor 6, Philadelphia, PA 19104), Philadelphia, Pa., 2005.

[106] Spelsberg-Korspeter, G.; Hochlenert, D.; Heffel, E.; Wagner, A.; Hagedorn, P.; Sampaio, R.: Construction of Lyapunov functions for the estimation of basins of attraction, *Journal of the Brazilian Society of Mechanical Sciences and Engineering*, 34(2):633–639, 2012.

[107] Stanton, S.C.; Mann, B.P.; Owens, B.A.: Melnikov theoretic methods for characterizing the dynamics of the bistable piezoelectric inertial generator in complex spectral environments, *Physica D: Nonlinear Phenomena*, 241(6):711–720, 2012.

[108] Stanton, S.C.; McGehee, C.C.; Mann, B.P.: Reversible hysteresis for broadband magnetopiezoelastic energy harvesting, *Applied Physics Letters*, 95(17):174103, 2009.

[109] Stanton, S.C.; McGehee, C.C.; Mann, B.P.: Nonlinear dynamics for broadband energy harvesting: Investigation of a bistable piezoelectric

inertial generator, *Physica D: Nonlinear Phenomena*, 239(10):640–653, 2010.

[110] Stanton, S.C.; Owens, B.A.; Mann, B.P.: Harmonic balance analysis of the bistable piezoelectric inertial generator, *Journal of Sound and Vibration*, 331(15):3617–3627, 2012.

[111] Szemplińska-Stupnicka, W.: The refined approximate criterion for chaos in a two-state mechanical oscillator, *Ingenieur-Archiv*, 58(5):354–366, 1988.

[112] Szemplińska-Stupnicka, W.: Cross-well chaos and escape phenomena in driven oscillators, *Nonlinear Dynamics*, 3(3):225–243, 1992.

[113] Szemplińska-Stupnicka, W.: The analytical predictive criteria for chaos and escape in nonlinear oscillators: A survey, *Nonlinear Dynamics*, 7(2):129–147, 1995.

[114] Tang, L.; Yang, Y.; Soh, C.K.: Toward Broadband Vibration-based Energy Harvesting, *Journal of Intelligent Material Systems and Structures*, 21(18):1867–1897, 2010.

[115] Teschl, G.: *Ordinary differential equations and dynamical systems*, volume v. 140 of *Graduate studies in mathematics*, American Mathematical Society, Providence, R.I., 2012.

[116] Timoshenko, S.; Gere, J.M.: *Theory of elastic stability*, Engineering societies monographs, McGraw-Hill and Kogakusha, New York and Toronto and London and Tokyo, 1963, 2nd edition edition.

[117] Timoshenko, S.; Woinowsky-Krieger, S.: *Theory of plates and shells*, Engineering societies monographs, McGraw-Hill, New York, 1959, 2d ed. edition.

[118] Todd, M.D.; Virgin, L.N.: An Experimental Verification of Basin Metamorphoses in A Nonlinear Mechanical System, *International Journal of Bifurcation and Chaos*, 07(06):1337–1357, 1997.

[119] Torby, B.J.: *Advanced dynamics for engineers*, HRW series in mechanical engineering, Holt, Rinehart, and Winston, New York, N.Y., 1984.

[120] Trigona, C.; Maiorca, F.; Ando, B.; Baglio, S.: Tri-stable behavior in mechanical oscillators to improve the performance of vibration energy

harvesters, *2013 Transducers & Eurosensors XXVII: The 17th International Conference on Solid-State Sensors, Actuators and Microsystems (TRANSDUCERS & EUROSENSORS XXVII)*, pp. 458–461.

[121] Troger, H.; Steindl, A.: *Nonlinear Stability and Bifurcation Theory*, Springer Vienna, Vienna, 1991.

[122] Tseng, W.Y.; Dugundji, J.: Nonlinear Vibrations of a Buckled Beam Under Harmonic Excitation, *Journal of Applied Mechanics*, 38(2):467, 1971.

[123] Twiefel, J.; Westermann, H.: Survey on broadband techniques for vibration energy harvesting, *Journal of Intelligent Material Systems and Structures*, 24(11):1291–1302, 2013.

[124] University of Bristol/University of Southampton: Next Generation Energy-Harvesting Electronics: Holistic Approach [Available]: `http://www.holistic.ecs.soton.ac.uk`. , downloaded via the EH Network Data Repository, `http://eh-network.org/data`, 2015 (accessed September 14, 2015).

[125] Ventsel, E.; Krauthammer, T.: *Thin plates and shells: Theory, analysis, and applications*, Marcel Dekker, New York, 2001.

[126] Verlag & Freie Medien (Editor): *RFID & Co. aus der Metropolregion Nürnberg*, Fraunhofer IIS, Zentrum für Intelligente Objekte ZIO, 2012.

[127] Vocca, H.; Neri, I.; Travasso, F.; Gammaitoni, L.: Kinetic energy harvesting with bistable oscillators, *Applied Energy*, 97:771–776, 2012.

[128] Wagg, D.; Neild, S.: *Nonlinear vibration and control: For flexible and adaptive structures*, volume 170 of *Solid Mechanics and Its Applications*, Springer, Dordrecht and Heidelberg [u.a.], 2010.

[129] Waite, J.J.; Virgin, L.N.; Wiebe, R.: Competing Responses in a Discrete Mechanical System, *International Journal of Bifurcation and Chaos*, 24(01):1430003, 2014.

[130] Wu, Y.; Badel, A.; Formosa, F.; Liu, W.; Agbossou, A.: Nonlinear vibration energy harvesting device integrating mechanical stoppers used as synchronous mechanical switches, *Journal of Intelligent Material Systems and Structures*, 25(14):1658–1663, 2014.

[131] Wu, Z.; Harne, R.L.; Wang, K.W.: Excitation-Induced Stability in a Bistable Duffing Oscillator: Analysis and Experiments, *Journal of Computational and Nonlinear Dynamics*, 10(1):11016, 2015.

[132] Xue, H.; Hu, Y.; Wang, Q.M.: Broadband piezoelectric energy harvesting devices using multiple bimorphs with different operating frequencies, *IEEE transactions on ultrasonics, ferroelectrics, and frequency control*, 55(9):2104–2108, 2008.

[133] Yang, Z.; Yang, J.: Connected Vibrating Piezoelectric Bimorph Beams as a Wide-band Piezoelectric Power Harvester, *Journal of Intelligent Material Systems and Structures*, 20(5):569–574, 2008.

[134] Zhou, S.; Cao, J.; Erturk, A.; Lin, J.: Enhanced broadband piezoelectric energy harvesting using rotatable magnets, *Applied Physics Letters*, 102(17):173901, 2013.

[135] Zhou, S.; Cao, J.; Inman, D.J.; Lin, J.; Liu, S.; Wang, Z.: Broadband tristable energy harvester: Modeling and experiment verification, *Applied Energy*, 133:33–39, 2014.

[136] Zhu, D.; Tudor, M.J.; Beeby, S.P.: Strategies for increasing the operating frequency range of vibration energy harvesters: a review, *Measurement Science and Technology*, 21(2):22001, 2010.

A. Appendix

A.1. Coefficients for the electromechanically coupled equations

$$\bar{m} = \frac{\left(2\pi^2 - 9\right)}{6\pi^2} Al\rho + \bar{m}_p + m, \tag{A.1a}$$

$$\bar{m}_e = \frac{A_p \rho_p}{\pi^2 l}\left(2l^2(\cos\frac{\pi l_2}{l} - \cos\frac{\pi l_1}{l}) + \pi^2\left(l_2^2 - l_1^2\right)\right) + m + \frac{\left(\pi^2 - 4\right)}{2\pi^2} m_b, \tag{A.1b}$$

$$\bar{m}_p = \frac{A_p \rho_p}{6\pi^3 l^2}\left(24l^3\left(\sin\frac{\pi l_1}{l} - \sin\frac{\pi l_2}{l}\right) + 3l^3\left(\sin\frac{2\pi l_1}{l} - \sin\frac{2\pi l_2}{l}\right) + 6\pi l^2\left(l_2 - l_1\right) + 24\pi l^2\left(l_2\cos\frac{\pi l_2}{l} - l_1\cos\frac{\pi l_1}{l}\right) + 4\pi^3\left(l_2^3 - l_1^3\right)\right), \tag{A.1c}$$

$$\bar{\mu} = \mu\frac{\left(9 - 2\pi^2\right) lA\rho}{6\pi^2}, \tag{A.1d}$$

$$\alpha = \frac{\pi^2 EI}{2l^3} - \frac{kl_0}{2l} + \frac{\pi E_p b_p h_p\left(6h_b h_p + 3h_b^2 + 4h_p^2\right)}{24l^4}\left(2\pi\left(l_2 - l_1\right) - l\left(\sin\frac{2\pi l_2}{l} - \sin\frac{2\pi l_1}{l}\right)\right), \tag{A.1e}$$

$$\beta = \left(\frac{5\pi^2 EI}{4l^5} + \frac{k\left(2l - 19l_0\right)}{16l^3}\right), \tag{A.1f}$$

$$C_p = \frac{\left(l_2 - l_1\right)\varepsilon_{33}^S b_p}{h_p}, \tag{A.1g}$$

$$\lambda = \frac{e_{31} b_p\left(\cos\left(\frac{\pi l_1}{l}\right) - \cos\left(\frac{\pi l_2}{l}\right)\right)\left(h_b + h_p\right)}{2l}, \tag{A.1h}$$

$$\phi = 1/R \tag{A.1i}$$

A.2. Nonlinear restoring force of the composite plate

$$\mathbf{K}(\mathbf{q}) = \frac{1}{9a^3b^3\theta\lambda\eta} \begin{bmatrix} 512a^4b^4E_1\eta^2G_{12}\theta h_l p_1 p_2^2 + \\ \quad 72a^2\big(\alpha_1-\alpha_2\big)b^4\Delta T E_1E_2\theta\lambda h_l^2\big(\kappa-2E_2\nu_{12}\big) + \\ \quad 96a^2b^2\delta E_1E_2\lambda\nu_{12}h_l^3p_2 + 48b^4\delta E_1\kappa\lambda h_l^3p_1 \\ \\ 512a^4b^4E_1\eta^2G_{12}\theta h_l p_1^2 p_2 - \\ \quad 72\big(\alpha_1-\alpha_2\big)a^4b^2\Delta T E_1E_2\theta\lambda h_l^2\big(\kappa-2E_2\nu_{12}\big) + \\ \quad 48a^4\delta E_1\kappa\lambda h_l^3p_2 + 96a^2b^2\delta E_1E_2\lambda\nu_{12}h_l^3p_1 \end{bmatrix} \tag{A.2}$$

with

$$\lambda = E_1\kappa\left(10a^4G_{12} + a^2b^2\kappa + 10b^4G_{12}\right) - \tag{A.3a}$$
$$\quad 2E_2\nu_{12}^2\left(5a^4G_{12}\kappa + 2a^2b^2E_1E_2 + 5b^4G_{12}\kappa\right), \tag{A.3b}$$
$$\delta = E_1^2 + 14E_1E_2 - 16E_2^2\nu_{12}^2 + E_2^2, \tag{A.3c}$$
$$\eta = (E_1+E_2)^2 - 4E_2^2\nu_{12}^2, \tag{A.3d}$$
$$\theta = E_1 - E_2\nu_{12}^2, \tag{A.3e}$$
$$\kappa = E_1 + E_2. \tag{A.3f}$$

A.3. Equations of motion of the electromechanical composite plate

The equations of motion are given by

$$\mathbf{M}\ddot{\mathbf{p}} + \mathbf{D}\dot{\mathbf{p}} + \mathbf{K}(\mathbf{p}) = \hat{\mathbf{e}}\,e(t). \tag{A.4}$$

The matrices are stated in the following.

Mass matrix M and excitation vector ê

$$\mathbf{M} = \begin{bmatrix} m_{11} & m_{12} & 0 & 0 \\ m_{12} & m_{22} & 0 & 0 \\ 0 & 0 & 0 & 0 \\ 0 & 0 & 0 & 0 \end{bmatrix} \tag{A.5}$$

with

$$\begin{aligned} m_{11} =& \frac{1}{45a^4}\left(9a^5bh\rho + 20a^3bh^3\rho + 3h_p\Delta x_p\Delta y_p\rho_p\big(80h_p^2\big(12x_0^2+\right. \\ & \Delta x_p^2\big) + 9\big(80x_0^4 + 40x_0^2\Delta x_p^2 + \Delta x_p^4\big) + 240h_p\big(12x_0^2+ \\ & \left.\Delta x_p^2\big)h_l + 240\big(12x_0^2 + \Delta x_p^2\big)h_l^2\big), \end{aligned} \tag{A.6}$$

$$m_{12} = \frac{1}{9a^2b^2}\left(a^3b^3h\rho + 3h_p\Delta x_p\big(12x_0^2 + \Delta x_p^2\big)\Delta y_p\big(12y_0^2 + \Delta y_p^2\big)\rho_p\right), \tag{A.7}$$

$$\begin{aligned} m_{22} =& \frac{1}{45b^4}\left(9ab^5h\rho + 20ab^3h^3\rho + 3h_p\Delta x_p\Delta y_p\rho_p\big(80h_p^2\big(12y_0^2+\right. \\ & \Delta y_p^2\big)9 + \big(80y_0^4 + 40y_0^2\Delta y_p^2 + \Delta y_p^4\big) + 240h_p\big(12y_0^2+ \\ & \left.\Delta y_p^2\big)h_l + 240\big(12y_0^2 + \Delta y_p^2\big)h_l^2\big). \end{aligned} \tag{A.8}$$

The excitation vector is given by

$$\hat{\mathbf{e}} = \begin{bmatrix} \frac{1}{3q^2}\left(a^3bh\rho + 3h_p\Delta x_p\Delta y_p\big(12x_0^2 + \Delta x_p^2\big)\rho_p\right) \\ \frac{1}{3b^2}\left(ab^3h\rho + 3h_p\Delta x_p\Delta y_p\big(12y_0^2 + \Delta y_p^2\big)\rho_p\right) \\ 0 \\ 0 \end{bmatrix}. \tag{A.9}$$

Restoring force K(q)

The vector containing the nonlinear restoring force is defined by

$$\mathbf{K}(\mathbf{q}) = \begin{bmatrix} \frac{\partial \mathcal{U}_s + \mathcal{U}_p - \mathcal{W}_e}{\partial p_1} \\ \frac{\partial \mathcal{U}_s + \mathcal{U}_p - \mathcal{W}_e}{\partial p_2} \\ \frac{\mathrm{d}}{\mathrm{d}t}\frac{\partial \mathcal{D}_e}{\partial v_1} \\ \frac{\mathrm{d}}{\mathrm{d}t}\frac{\partial \mathcal{D}_e}{\partial v_2} \end{bmatrix}. \tag{A.10}$$

In the following the potential energy of the structure $\mathcal{U}_s$, the potential energy of the piezoelectric patches $\mathcal{U}_p$ and the work of the electric forces $\mathcal{W}_e$ are

stated. It can be shown that $e_i = 0$ for $i = 4, 8, 9, 10, 11$, thus the functionals are functions of the unknowns e_i for $i = 1, 2, 3, 5, 6, 7$. Due to the large number of variables in the polynomials it is not possible to state a closed-form solution for the parameters e_i. Thus, the determination of the yet unknowns e_i has to be performed numerically by solving the equations

$$\frac{\partial(\mathcal{U}_s + \mathcal{U}_p - \mathcal{W}_e)}{\partial e_i} = 0, \qquad \text{with} \qquad i = 1, 2, 3, 5, 6, 7. \tag{A.11}$$

The functionals are defined by

$$\begin{aligned}
\mathcal{U}_s = &\frac{1}{1440a^3b^3\big(E_1 - E_2\nu_{12}^2\big)} h_l \big(5120b^2p_1^2\big(3b^2E_1(E_1+E_2)h_l^2 + \\
&8a^2G_{12}p_2^2\big(E_1 - E_2\nu_{12}^2\big)\big) - 160a^2b^2p_1\big(-16p_2\big(-a^2b^2E_2(e_3+e_6) \\
&G_{12}\nu_{12}^2 + E_1\big(a^2b^2e_3G_{12} + a^2b^2e_6G_{12} + 24E_2h_l^2\nu_{12}\big)\big) + \\
&3b^2E_1h_l\big(12e_1(E_1 - E_2) + E_1\big(a^2e_2 + b^2e_3 - 12\Delta\alpha_1\big) - \\
&E_2\big(a^2e_2 + b^2e_3 - 12\Delta\big(\alpha_2 + \alpha_1\nu_{12} - \alpha_2\nu_{12}\big)\big)\big)\big) + \\
&a^4\big(15360E_1(E_1+E_2)p_2^2h_l^2 + 480b^2E_1p_2h_l\big(E_1\big(12e_5 + a^2e_6 + \\
&b^2e_7 - 12\Delta\alpha_1\big) - E_2\big(12e_5 + a^2e_6 + b^2e_7 - 12\Delta\alpha_2 - 12\Delta\alpha_1\nu_{12} + \\
&12\Delta\alpha_2\nu_{12}\big)\big) + b^4\big(720e_1^2E_1(E_1+E_2) + E_1^2\big(9a^4e_2^2 + 9b^4e_3^2 + \\
&720e_5^2 + 9a^4e_6^2 + 10a^2b^2e_6e_7 + 9b^4e_7^2 - 120b^2e_3\Delta\alpha_1 - \\
&120a^2e_6\Delta\alpha_1 - 120b^2e_7\Delta\alpha_1 + 10a^2e_2\big(b^2e_3 - 12\Delta\alpha_1\big) + \\
&120e_5\big(a^2e_6 + b^2e_7 - 12\Delta\alpha_1\big)\big) - 40a^2b^2E_2(e_3+e_6)^2G_{12}\nu_{12}^2 + \\
&120e_1E_1\big(E_1\big(a^2e_2 + b^2e_3 - 12\Delta\alpha_1\big) + E_2\big(a^2e_2 + b^2e_3 + \\
&2\big(\big(12e_5 + a^2e_6 + b^2e_7 - 6\Delta\alpha_1\big)\nu_{12} - 6\Delta\alpha_2\big(1+\nu_{12}\big)\big)\big)\big) + \\
&E_1\big(40a^2b^2(e_3+e_6)^2G_{12} + E_2\big(9a^4e_2^2 + 9b^4e_3^2 + 720e_5^2 + \\
&9a^4e_6^2 + 10a^2b^2e_6e_7 + 9b^4e_7^2 - 120b^2e_3\Delta\alpha_2 - 120a^2e_6\Delta\alpha_2 - \\
&120b^2e_7\Delta\alpha_2 + 20a^2b^2e_3e_6\nu_{12} + 36b^4e_3e_7\nu_{12} - 120b^2e_3\Delta\alpha_1\nu_{12} - \\
&120\big(a^2e_6\Delta\alpha_1\nu_{12} - b^2e_7\Delta\alpha_1\nu_{12} - b^2e_3\Delta\alpha_2\nu_{12} - a^2e_6\Delta\alpha_2\nu_{12} - \\
&b^2e_7\Delta\alpha_2\nu_{12} + e_5\big(a^2e_6 + b^2e_7 + 2\big(\big(a^2e_2 + b^2e_3 - 6\Delta\alpha_1\big)\nu_{12} - \\
&6\Delta\alpha_2\big(1+\nu_{12}\big)\big)\big) + 2a^2e_2\big(5b^2e_3 - 2\big(\big(-9a^2e_6 - 5b^2e_7 + \\
&30\Delta\alpha_1\big)\nu_{12} + 30\Delta\alpha_2\big(1+\nu_{12}\big)\big)\big)\big)\big)\big)\big),
\end{aligned} \tag{A.12}$$

$$\begin{aligned}\mathcal{U}_p =& \frac{1}{720a^4b^4}\Delta x_p\Delta y_p\big(5120h_p p_1^2\big(4c_{66}^E\big(12x_0^2+\Delta x_p^2\big)\big(12y_0^2+\Delta y_p^2\big)p_2^2+\\ &3b^4c_{11}^E\big(h_p^2+3h_ph_l+3h_l^2\big)\big)+160a^2b^2p_1\big(8h_pp_2\big(c_{66}^E(e_3+e_6)\\ &\big(12x_0^2+\Delta x_p^2\big)\big(12y_0^2+\Delta y_p^2\big)+24c_{12}^E\big(h_p^2+3h_ph_l+3h_l^2\big)\big)+\\ &9b^2e_{31}\big(h_p+2h_l\big)(v_1+v_2)\big)+a^4\big(15360c_{11}^Eh_pp_2^2\big(h_p^2+3h_ph_l+\\ &3h_l^2\big)+1440b^2e_{31}p_2\big(h_p+2h_l\big)(v_1+v_2)+b^4\big(h_p\big(c_{11}^E\big(720e_1^2+\\ &720e_5^2+720e_2^2x_0^4+720e_6^2x_0^4+1440e_2e_3x_0^2y_0^2+1440e_6e_7x_0^2y_0^2+\\ &720e_3^2y_0^4+720e_7^2y_0^4+360e_2^2x_0^2\Delta x_p^2+360e_6^2x_0^2\Delta x_p^2+\\ &120e_2e_3y_0^2\Delta x_p^2+120e_6e_7y_0^2\Delta x_p^2+9e_2^2\Delta x_p^4+9e_6^2\Delta x_p^4+\\ &120e_2e_3x_0^2\Delta y_p^2+120e_6e_7x_0^2\Delta y_p^2+360e_3^2y_0^2\Delta y_p^2+360e_7^2y_0^2\Delta y_p^2+\\ &10e_2e_3\Delta x_p^2\Delta y_p^2+10e_6e_7\Delta x_p^2\Delta y_p^2+9e_3^2\Delta y_p^4+9e_7^2\Delta y_p^4+\\ &120e_5\big(12e_6x_0^2+12e_7y_0^2+e_6\Delta x_p^2+e_7\Delta y_p^2\big)+120e_1\big(e_2\big(12x_0^2+\\ &\Delta x_p^2\big)+e_3\big(12y_0^2+\Delta y_p^2\big)\big)\big)+2\big(10c_{66}^E(e_3+e_6)^2\big(12x_0^2+\Delta x_p^2\big)\\ &\big(12y_0^2+\Delta y_p^2\big)+c_{12}^E\big(60e_1\big(12e_5+e_6\big(12x_0^2+\Delta x_p^2\big)+e_7\big(12y_0^2+\\ &\Delta y_p^2\big)\big)+e_2\big(60e_5\big(12x_0^2+\Delta x_p^2\big)+9e_6\big(80x_0^4+40x_0^2\Delta x_p^2+\Delta x_p^4\big)+\\ &5e_7\big(12x_0^2+\Delta x_p^2\big)\big(12y_0^2+\Delta y_p^2\big)\big)+e_3\big(60e_5\big(12y_0^2+\Delta y_p^2\big)+\\ &5e_6\big(12x_0^2+\Delta x_p^2\big)\big(12y_0^2+\Delta y_p^2\big)+9e_7\big(80y_0^4+40y_0^2\Delta y_p^2+\\ &\Delta y_p^4\big)\big)\big)\big)\big)-30e_{31}\big(12e_1+12e_5+12e_2x_0^2+12e_6x_0^2+12e_3y_0^2+\\ &12e_7y_0^2+e_2\Delta x_p^2+e_6\Delta x_p^2+e_3\Delta y_p^2+e_7\Delta y_p^2\big)v_1+30e_{31}\big(12e_1+\\ &12e_5+12e_2x_0^2+12e_6x_0^2+12e_3y_0^2+12e_7y_0^2+e_2\Delta x_p^2+e_6\Delta x_p^2+\\ &e_3\Delta y_p^2+e_7\Delta y_p^2\big)v_2\big)\big)\big),\end{aligned} \tag{A.13}$$

$$\begin{aligned}\mathcal{W}_e =& \frac{1}{24a^2b^2h_p}\Delta x_p \Delta y_p \big(e_{31}h_p\big(-48b^2p_1\big(h_p+2h_l\big)+a^2\big(b^2\big(12e_1+\\ &12(\,e_5+e_2x_0^2+e_6x_0^2+e_3y_0^2+e_7y_0^2+e_2\Delta x_p^2+e_6\Delta x_p^2+e_3\Delta y_p^2+\\ &e_7\Delta y_p^2\big)-48p_2\big(h_p+2h_l\big)\big)\big)v_1+12a^2b^2\varepsilon_{33}^S v_1^2+\\ &v_2\big(-48b^2e_{31}h_pp_1\big(h_p+2h_l\big)-a^2\big(48e_{31}h_pp_2\big(h_p+2h_l\big)+\\ &b^2\big(e_{31}h_p\big(12(e_1+e_5+e_2x_0^2+e_6x_0^2+e_3y_0^2+e_7y_0^2)+\\ &e_2\Delta x_p^2+e_6\Delta x_p^2+e_3\Delta y_p^2+e_7\Delta y_p^2\big)-12\varepsilon_{33}^S v_2\big)\big)\big)\big)\end{aligned} \tag{A.14}$$

Damping matrix D

The damping matrix $\mathbf{D}$ is defined by

$$\mathbf{D}=\begin{bmatrix}\alpha_0\ m_{11} & \alpha_0\ m_{12} & 0 & 0\\ \alpha_0\ m_{12} & \alpha_0\ m_{22} & 0 & 0\\ & \frac{\mathrm{d}}{\mathrm{d}t}\frac{\partial \mathcal{U}_s+\mathcal{U}_p-\mathcal{W}_e}{\partial v_1} & & \\ & \frac{\mathrm{d}}{\mathrm{d}t}\frac{\partial \mathcal{U}_s+\mathcal{U}_p-\mathcal{W}_e}{\partial v_2} & & \end{bmatrix}. \tag{A.15}$$

Note that the unknowns e_i contained in the functionals $\mathcal{U}_s$,$\mathcal{U}_p$ and $\mathcal{W}_e$ are determined by Eqn (A.11).

A.4. Nonlinear restoring force of the multistable plate

The nonlinear restoring force results from the potential energy $\mathcal{U}$ (3.128). The potential energy is of the form

$$\mathcal{U} = \alpha_1 p_1^2 + \alpha_2 p_2^2 + \beta_1 p_1^4 + \beta_2 p_2^4 + \gamma p_1 p_2 + \eta_1 p_1^3 p_2 + \eta_2 p_1 p_2^3 + \kappa p_1^2 p_2^2 \tag{A.16}$$

with the coefficients

$$\begin{aligned}\alpha_1 =& \frac{1}{9a^3\eta\xi} 8Eh\big(- 3b\big(80a^7 G\xi k_x\big(Eh\Delta l_x + \nu k_y \Delta l_y\big) + \\ & 20a^6 G k_x\big(9b\xi k_y \Delta l_x + 4Eh^3\big) + 4a^5 b\big(4E^2\big(bh\xi k_x \Delta l_x + 5Gh^4\big) + \\ & 4bE\xi\nu k_x k_y \Delta l_y + 5G k_x k_y\big(5b\xi\Delta l_y + \big(9-4\nu\big)h^2\big)\big) + \\ & 36a^4 b^2 E\big(b\xi k_x k_y \Delta l_x + Eh^3 k_x + 5Gh^3 k_y\big) + \\ & a^3 b^3\big(Ehk_x\big(80bG\xi\Delta l_x + h\big(81-16\nu^2\big)k_y\big) + 40G\nu k_x k_y\big(2b\xi\Delta l_y - \\ & 5h^2\big) + 16E^3 h^4\big) + 4a^2 b^4\big(20bG\xi k_x k_y \Delta l_x + 9E^2 h^3 k_y + \\ & 45EGh^3 k_x\big) + 20ab^5 Gh^2\big(Ek_x + 5Gk_y\big) + 80b^6 EGh^3 k_y\big) + \\ & 16a^3\xi p_2^2\big(40a^4 G\nu k_x k_y + 36a^3 bEGhk_x + a^2 b^2\big(16E^2 Gh^2 + \\ & 8E\nu k_x k_y + G\big(131-16\nu^2\big)k_x k_y\big) + 36ab^3 EGhk_y + 40b^4 G\nu k_x k_y\big)\big),\end{aligned} \tag{A.17}$$

$$\begin{aligned}\alpha_2 =& \frac{1}{9b^3\eta\xi} 8Eh\big(- 3a\big(80a^6 EGh^3 k_x + 20a^5 bG\big(k_x k_y\big(4b\xi\Delta l_y + \\ & \big(9-4\nu\big)h^2\big) + 4E^2 h^4\big) + 4a^4 b^2\big(5EGhk_y\big(4b\xi\Delta l_y + 9h^2\big) + \\ & 20bG\xi\nu k_x k_y \Delta l_x + 9E^2 h^3 k_x\big) + a^3 b^3\big(Ek_x k_y\big(36b\xi\Delta l_y + \\ & h^2\big(81-16\nu^2\big)\big) + 16E^3 h^4 - 200Gh^2\nu k_x k_y\big) + \\ & 4a^2 b^4\big(E^2 hk_y\big(4b\xi\Delta l_y + 9h^2\big) + Ek_x\big(4b\xi\nu k_y \Delta l_x + 45Gh^3\big) + \\ & 25bG\xi k_x k_y \Delta l_x\big) + 20ab^5 G\big(k_x k_y\big(9b\xi\Delta l_y + \big(9-4\nu\big)h^2\big) + 4E^2 h^4\big) + \\ & 80b^6 Gk_y\big(E\big(bh\xi\Delta l_y + h^3\big) + b\xi\nu k_x \Delta l_x\big)\big) + 16b^3\xi p_1^2\big(40a^4 G\nu k_x k_y + \\ & 36a^3 bEGhk_x + a^2 b^2\big(16E^2 Gh^2 + 8E\nu k_x k_y + G\big(131-16\nu^2\big)k_x k_y\big) + \\ & 36ab^3 EGhk_y + 40b^4 G\nu k_x k_y\big)\big),\end{aligned} \tag{A.18}$$

$$\beta_1 = -\frac{1}{9a^5\eta\xi}128bEh\big(-20a^8EGh\xi k_x - 45a^7bG\xi k_xk_y + 4a^6Ehk_x\big(b^2\big(E-E\nu^2\big)+20Gh^2\big)+a^5\big(20bGh^2\big(4E^2h^2+\big(9-4\nu\big)k_xk_y\big)-9b^3E\xi k_xk_y\big)-4a^4b^2Eh\big(5b^2G\xi k_x-9\delta h^2\big)+a^3b^3\big(16E^3h^4-20Gk_xk_y\big(b^2\xi+10h^2\nu\big)+Eh^2\big(81-16\nu^2\big)k_xk_y\big)+36a^2b^4Eh^3\lambda+20ab^5Gh^2\big(Ek_x+5Gk_y\big)+80b^6EGh^3k_y\big), \tag{A.19}$$

$$\beta_2 = -\frac{1}{9b^5\eta\xi}128aEh\big(80a^6EGh^3k_x - 20a^5bG\big(k_xk_y\big(b^2\xi+h^2\big(4\nu^2-9\big)\big)-4E^2h^4\big)-4a^4b^2Eh\big(5Gk_y\big(b^2\xi-9h^2\big)-9Eh^2k_x\big)+a^3b^3\big(Ek_xk_y\big(h^2\big(81-16\nu^2\big)-9b^2\xi\big)+16E^3h^4-200Gh^2\nu k_xk_y\big)+4a^2b^4Eh\big(Ek_y\big(b^2\big(-\nu^2\big)+b^2+9h^2\big)+45Gh^2k_x\big)-5ab^5G\big(k_xk_y\big(9b^2\xi+4h^2\big(4\nu^2-9\big)\big)-16E^2h^4\big)-20b^6EGhk_y\big(b^2\xi-4h^2\big)\big), \tag{A.20}$$

$$\gamma = -\frac{1}{3ab\eta\xi}16Eh\big(80a^6EGh^3\nu k_x - 20a^5bG\big(2b\xi k_x\big(Eh\Delta l_x+\nu k_y\Delta l_y\big)+h^2\nu\big(\big(4\nu^2-9\big)k_xk_y-4E^2h^2\big)\big)+18a^4b^2\big(2\delta Eh^3\nu-5bG\xi k_xk_y\Delta l_x\big)+a^3b^3\big(h^2\nu\big(16E^3h^2+E\big(81-16\nu^2\big)k_xk_y-200G\nu k_xk_y\big)-90bG\xi k_xk_y\Delta l_y\big)+4a^2b^4\big(9Eh^3\lambda\nu-10bG\xi k_y\big(Eh\Delta l_y+\nu k_x\Delta l_x\big)\big)+20ab^5Gh^2\nu\big(Ek_x+5Gk_y\big)+80b^6EGh^3\nu k_y\big), \tag{A.21}$$

$$\eta_1 = -\frac{1}{9a^3b\eta\xi}128Eh\big(40a^6EGhk_x\big(b^2\xi+2h^2\nu\big)+10a^5bG\big(9b^2\xi k_xk_y+2h^2\nu\big(Ek_x+5Gk_y\big)\big)+36a^4b^2\delta Eh^3\nu+a^3b^3\nu\big(40Gk_xk_y\big(b^2\xi-5h^2\nu\big)+16E^3h^4+Eh^2\big(81-16\nu^2\big)k_xk_y\big)+36a^2b^4Eh^3\lambda\nu+20ab^5Gh^2\nu\big(Ek_x+5Gk_y\big)+80b^6EGh^3\nu k_y\big), \tag{A.22}$$

$$\begin{aligned}\eta_2 =& -\frac{1}{9ab^3\eta\xi}128Eh\big(80a^6EGh^3\nu k_x + 20a^5bG\nu\big(k_xk_y\big(2b^2\xi+\\ &h^2\big(9-4\nu\big)\big)+4E^2h^4\big)+36a^4b^2\delta Eh^3\nu + a^3b^3\big(90b^2G\xi k_xk_y+\\ &h^2\nu\big(16E^3h^2+E\big(81-16\nu^2\big)k_xk_y-200G\nu k_xk_y\big)\big)+\\ &4a^2b^4Eh\big(10b^2G\xi k_y+9h^2\lambda\nu\big)+20ab^5Gh^2\nu\big(Ek_x+5Gk_y\big)+\\ &80b^6EGh^3\nu k_y\big),\end{aligned} \tag{A.23}$$

$$\begin{aligned}\kappa =&\frac{1}{9\eta}128Eh\big(40a^4G\nu k_xk_y+36a^3bEGhk_x+a^2b^2\big(16E^2Gh^2+\\ &8E\nu k_xk_y+G\big(131-16\nu^2\big)k_xk_y\big)+36ab^3EGhk_y+40b^4G\nu k_xk_y\big),\end{aligned} \tag{A.24}$$

with

$$\begin{aligned}\eta =&80a^6EGhk_x+20a^5bG\big(Ek_x+5Gk_y\big)+36a^4b^2\delta Eh+\\ &a^3b^3\big(16E^3h^2+E\big(81-16\nu^2\big)k_xk_y-200G\nu k_xk_y\big)+36a^2b^4Eh\lambda+\\ &20ab^5G\big(Ek_x+5Gk_y\big)+80b^6EGhk_y,\end{aligned} \tag{A.25}$$

$$\xi =\nu-1. \tag{A.26}$$

The nonlinear restoring force is defined by

$$\mathbf{K}(\mathbf{q}) = \begin{bmatrix}\dfrac{\partial\mathcal{U}}{\partial p_1}\\ \dfrac{\partial\mathcal{U}}{\partial p_2}\end{bmatrix}. \tag{A.27}$$

Bisher sind in dieser Reihe erschienen

Band 1
Zur mikrorissinduzierten Schädigung spröder Materialien
B. Lauterbach, Dissertation 2001, ISBN 3-935868-01-4

Band 2
3D-Simulation der Mikrostrukturentwicklung in Zwei-Phasen-Materialien
R. Müller, Dissertation 2001, ISBN 3-935868-02-2

Band 3
Zur numerischen Simulation von Morphologieänderungen in mikroheterogenen Materialien
S. Kolling, Dissertation 2001, ISBN 3-935868-03-0

Band 4
Theoretische und numerische Untersuchung von Versagensmechanismen in Metall-Keramik-Verbundwerkstoffen
T. Emmel, Dissertation 2002, ISBN 3-935868-04-9

Band 5
On microcrack dominated problems in dynamics and statics of brittle fracture: a numerical study by boundary element techniques
S. Rafiee, Dissertation 2002, ISBN 3-935868-05-7

Band 6
Kontinuumsmechanik anisotroper Festkörper und Fluide
H. Ehrentraut, Habilitationsschrift 2002, ISBN 3-935868-06-5

Band 7
Plane unsteady inviscid incompressible hydrodynamics of a thin elastic profile
N. Blinkova, Dissertation 2002, ISBN 3-935868-07-3

Band 8
Anmerkungen zur Simulation von entfestigendem Materialverhalten
H. Baaser, Habilitationsschrift 2004, ISBN 3-935868-08-1

Band 9
Orts- und zeitadaptive DAE-Methoden zur Beschreibung elastisch-plastischen Materialverhaltens innerhalb der FEM
S. Eckert, Dissertation 2005, ISBN 3-935868-09-X

Band 10
Simulations of the Flow of the Ross Ice Shelf, Antarctica: Parameter Sensitivity Tests and Temperature-Dependent Rate Factor
A. Humbert, Dissertation 2005, ISBN 3-935868-10-3

Band 11
A Thermo-mechanical Continuum Theory with Internal Length of Cohesionless Granular Materials
Chung Fang, Dissertation 2006, ISBN 3-935868-11-1

Band 12
Modeling Dry Granular Avalanches past Different Obstructions: Numerical Simulation and Laboratory Analyses
Chiou Min-Ching, Dissertation 2006, ISBN 3-935868-12-X

Band 13
Configurational forces in defect mechanics and in computational methods
R. Müller, Habilitationsschrift 2005, ISBN 3-935868-13-8

Band 14
Hyperelastic dynamics in physical and material space
S. Kolling, Habilitationsschrift 2007, ISBN 978-3-935868-14-3

Band 15
Phenomenological modeling of ferroelectric material behavior
V. Mehling, Dissertation 2007, ISBN 978-3-935868-15-0

Band 16
Ein mischungsbasiertes Materialmodell zum Knochenumbau
R.-R. Kühn, Dissertation 2006, ISBN 978-3-935868-16-7

Band 17
Einige Erweiterungen der Rand-Finite-Elemente-Methode und deren Anwendung auf Randeffekte in ebenen Laminaten
J. Artel, Dissertation 2007, ISBN 978-3-935868-17-4

Band 18
Spannungskonzentrations-Effekte an Verstärkungspflaster-Ecken
H. Wigger, Dissertation 2008, ISBN 978-3-935868-18-1

Band 19
Rotationseffekte in der Kristallplastizität
C. Bröse, Dissertation 2007, ISBN 978-3-935868-19-8

Band 20
Finite-Element-Modelle zur Simulation von Delaminationen dünner Filme auf Substraten
V. D. Pham, Dissertation 2010, ISBN 978-3-935868-20-4

Band 21
Asymptotische Nahfeldanalysen ebener Multi-Materialverbindungsstellen mit der Methode komplexer Potentiale
C. Sator, Dissertation 2010, ISBN 978-3-935868-21-1

Band 22
Modellierung spröder Rissbildung an Spannungskonzentrationen mit der Bruchmechanik finiter Risse
J. Hebel, Dissertation 2010, ISBN 978-3-935868-22-8

Band 23
Some Contributions to the Homogenization of Macroscopically Isotropic Composites
V. Salit, Dissertation 2011, ISBN 978-3-935868-23-5

Band 24
Asymptotic Analysis of the Load Transfer on Double-Lap Bolted Joints
J. Kratochvíl, Dissertation 2012, ISBN 978-3-935868-24-2

Band 25
Spannungssingularitätsordnungen in linear-elastischen und piezoelektrischen Multimaterialkonfigurationen mit der Rand-Finite-Elemente-Methode
W. Mayland, Dissertation 2012, ISBN 978-3-935868-25-9

Band 26
Plastizität und Skaleneffekte sowie Deformations- und Versagensmodellierung dünner metallischer Schichten bei Nanoindentation
A. Trondl, Dissertation 2012, ISBN 978-3-935868-26-6

Band 27
Theoretical modeling and parallel programming of a nonlinear composite finite shell element based on a mixed global-local variational principle
M. Schürg, Dissertation 2012, ISBN 978-3-935868-27-3

Band 28
Strukturmechanische Modellierung und Analyse des Tragverhaltens von dünn-wandigen hochbelasteten Composite-Biege- und Querkraftträgern
A. M. Kroker, Dissertation 2013, ISBN 978-3-935868-28-0

Band 30
Der Laminatrandeffekt und seine Analyse, insbesondere mit der Rand-Finite-Elemente-Methode
J. Lindemann, Dissertation 2013, ISBN 978-3-935868-30-3

Band 31
Avoidance of brake squeal by a separation of the brake disc's eigenfrequencies: A structural optimization problem
A. Wagner, Dissertation 2013, ISBN 978-3-935868-31-0

Band 32
Ultrasonic Generators for Energy Harvesting Applications: Self-Excitation and Mechanical Frequency Transformation
E. Heffel, Dissertation 2013, ISBN 978-3-935868-32-7

Band 33
Neue Ansätze zur Analyse der Lastübertragung und Initiierung finiter Risse in Klebverbindungen
P. Weißgraeber, Dissertation 2014, ISBN 978-3-935868-33-4

Band 34
Instabilities and Wear Propagation in Calenders: Interactions with Structural Dynamics and Contact Kinematics
M. Eckstein, Dissertation 2014, ISBN 978-3-935868-34-1

Band 35
Adaptive Camber Airfoil for Load Alleviation in Horizontal Axis Wind Turbines: Analytical and Numerical Study
H. Spiegelberg, Dissertation 2014, ISBN 978-3-935868-35-8

Band 36
Erweiterungen der Rand-Finite-Elemente-Methode zur Analyse von Platten und Laminaten mit besonderem Fokus auf der Ermittlung von Singularitätsordnungen an Rissen und Kerben
R. Dieringer, Dissertation 2015, ISBN 978-3-935868-36-5

Band 37
Entwicklung und Analyse mikromechanischer Modelle zur Beschreibung des Effektivverhaltens von geschlossenzelligen Polymerschäumen
N.-C. Fahlbusch, Dissertation 2015, ISBN 978-3-935868-37-2

Band 38
Reduktion niederfrequenter Schwingungen von Windenergieanlagen durch Tilgersysteme
S. Katz, Dissertation 2015, ISBN 978-3-935868-38-9

The field of vibrational energy harvesting aims to transform ambient mechanical energy into electrical energy. Robust energy harvesters that allow to harvest sufficient energy over a broad frequency range are crucial for possible applications. One strategy to increase the bandwidth of energy harvesters and, thus, the robustness is the exploitation of multistable structures. This is due to their feature of showing large amplitude oscillations that result from snap-through actions (inter-well oscillations) in a significant frequency range.
In this thesis different multistable energy harvester designs are analyzed in order to optimize their performance and formulate design criteria. Based on analytical investigations, design criteria are formulated to describe the favorable harvesting domain. Numerical simulations are performed to supplement the analytical investigations. The differences of the considered structures are highlighted concerning robust and efficient harvesting by means of numerical simulations for different types of excitation. Experiments are carried out to complement the analytical and numerical analysis. The experiments establish the transferability of the numerical and analytical findings to real-world applications.

ISBN 978-3-935868-39-6